



# BRNO UNIVERSITY OF TECHNOLOGY

VYSOKÉ UČENÍ TECHNICKÉ V BRNĚ

## CENTRAL EUROPEAN INSTITUTE OF TECHNOLOGY BUT

STŘEDOEVROPSKÝ TECHNOLOGICKÝ INSTITUT VUT

## RESIDUAL LIFETIME OF PARTS WITH RESIDUAL STRESS

ZBYTKOVÁ ŽIVOTNOST SOUČÁSTÍ S REZIDUÁLNÍM NAPĚTÍM

### DOCTORAL THESIS

DIZERTAČNÍ PRÁCE

### AUTHOR

AUTOR PRÁCE

Ing. Pavol Dlhý

### SUPERVISOR

ŠKOLITEL

doc. Ing. Luboš Náhlík, Ph.D.

BRNO 2022



## Abstract

This doctoral thesis deals with residual stress determination and residual fatigue lifetime estimation of the sizable component. As a representative of the sizable components, the railway axles are used. Determining the entire residual stress field in sizable components is problematic in industrial conditions. Therefore, a new methodology is developed and used for the residual stress determination of the induction hardened railway axle. The developed methodology uses X-ray diffraction measurement for the surface residual stress determination and numerical simulations for the original residual stress field determination. Each piece of equipment is commonly present in industrial R&D laboratories. The residual stress effect is then implemented in the residual fatigue lifetime estimation procedure developed at the Institute of Physics of Materials of the Czech Academy of Sciences. Results showed no surface crack propagation after the induction hardening surface treatment. Therefore, residual fatigue lifetime is estimated for three quenched railway axles. Estimations are compared with experimentally tested railway axles. A significant improvement in the estimation has been achieved by including the residual stress effect in the residual fatigue lifetime estimation. The present work further deals with the sizable component analysis based on the damage-tolerant approach. That means the determination of the critical stress concentration position and estimation of the crack position; experimental determination of the fatigue crack growth curves; stochastic residual fatigue lifetime estimation in order to include the effect of the variability of the data. Results obtained in this work can be used for the inspection interval assessment of the cyclically loaded components with the residual stress.

## Keywords

Residual stress, railway axle, damage-tolerant concept, residual fatigue lifetime, finite element modelling, fatigue

## Abstrakt

Tato disertační práce se zabývá stanovením zbytkového napětí a odhadem zbytkové únavové životnosti rozměrné součásti. Jako zástupce rozměrných součástí jsou použity železniční nápravy. Určení celého pole zbytkových napětí v rozměrných součástech je v průmyslových podmínkách problematické. Proto je vyvinuta nová metodika, která je použita pro stanovení zbytkového napětí indukčně kalené železniční nápravy. Vyvinutá metodika využívá rentgenové difrakční měření pro stanovení povrchového zbytkového napětí a numerické simulace pro stanovení původního pole zbytkového napětí. Jednotlivé vybavení se běžně vyskytují v průmyslových laboratořích výzkumu a vývoje. Vliv zbytkového napětí je pak implementován do postupu odhadu zbytkové únavové životnosti vyvinutého na Ústavu fyziky materiálů Akademie věd ČR. Výsledky ukázaly, že po povrchové úpravě indukčním kalením nedochází k šíření povrchových trhlin. Proto byla odhadnuta zbytková únavová životnost tří klasicky kalených železničních náprav. Odhady jsou porovnány s experimentálně zkoušenými železničními nápravami. Výrazného zlepšení odhadu bylo dosaženo zahrnutím vlivu zbytkového napětí do odhadu zbytkové únavové životnosti. Tato práce se dále zabývá analýzou rozměrných součástí na základě přístupu přípustných poškození. To znamená určení polohy kritické koncentrace napětí a odhad polohy trhliny; experimentální určení křivek růstu únavových trhlin; stochastický odhad zbytkové únavové životnosti s cílem zahrnout vliv variability dat. Výsledky získané v této práci lze použít pro posouzení intervalu kontroly cyklicky zatěžovaných součástí se zbytkovým napětím.

## Klíčová slova

Zbytkové napětí, železniční náprava, přístup přípustných poškození, zbytková únavová životnost, konečno prvkové modelování, únava

#### Bibliographic citation

DLHÝ, Pavol. Residual lifetime of parts with residual stress. Brno, 2022. Available also at: <https://www.vutbr.cz/studenti/zav-prace/detail/143863>. Doctoral Thesis. Vysoké učení technické v Brně, Středoevropský technologický institut VUT, Central European Institute of Technology BUT. Supervisor Luboš Náhlík.

Declaration

I declare that this thesis was composed by myself under the supervision of doc. Ing. Luboš Náhlík, Ph.D., and it is an original work with cited literature and other professional sources listed in the text and reference list.

.....  
Pavol Dlhý

## Acknowledgement

This work has been created using the research infrastructure of the Institute of Physics of Materials of the Czech Academy of Sciences, v.v.i. and in close cooperation with BONATRANS GROUP a.s. This work was supported by project No. FV40034 "Development of new design of railway axles with high operational reliability" of Ministry of Industry and Trade of the Czech Republic.



First of all, I would like to thank my supervisor, doc. Ing. Luboš Náhlík, Ph.D., for this opportunity, guidance, encouragement and advice during my PhD study. Special thanks go to the head of the High Cycles Fatigue Group doc. Ing. Pavel Hutař, Ph.D., for his professional guidance and friendly attitude. I would also like to thank all my colleagues from IPM Pavel Pokorný, Jan Poduška, Ondrej Krepl, Tomáš Vojtek, Ondrej Slávik, Tomáš Oplt, Hector Tinoco, Lukáš Trávníček, Vítek Horník, Radek Kubíček and Dušan Ťichoň for sharing their advice and friendly atmosphere. I would also like to thank BONATRANS GROUP a.s. representatives Rostislav Fajkoš and Ondrej Peter their professional advice and consultation.

Special thanks to my wife Michaela, for her patience, motivation and support during my studies.

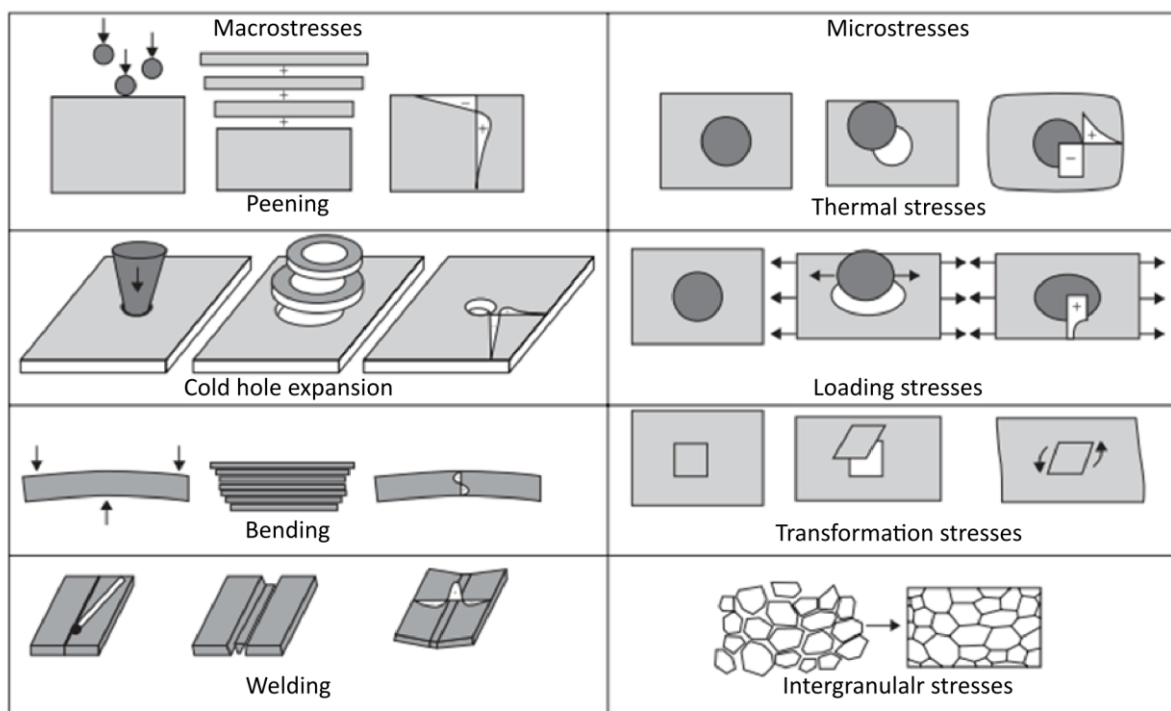
# Contents

1	Introduction .....	10
2	Theoretical background .....	12
2.1	Fracture Mechanics – Stress Intensity Factor.....	12
2.2	Fatigue of Metals.....	14
2.3	General Fatigue Design.....	15
2.3.1	Damage-tolerant Design.....	16
3	Review .....	17
3.1	Railway Axle Design .....	17
3.1.1	Non-Destructive Testing and Probability of Detection.....	19
3.2	Residual fatigue lifetime of the railway axle with the crack .....	20
3.2.1	Investigation of the railway axle with the crack.....	20
3.2.2	Stress Intensity Factor Determination for the Railway Axle with a Crack.....	21
3.3	Residual Fatigue Lifetime Determination for the Railway Axle.....	24
3.3.1	Influence of Residual Stress on Residual Fatigue Lifetime .....	25
3.4	Residual Stress – Review .....	25
3.4.1	Background and Definition of Residual Stress.....	25
3.4.2	Production of Residual Stress .....	26
3.4.3	Effect of Residual Stress .....	26
3.4.4	Residual Stress Length Scales .....	26
3.5	Overview of Residual Stress Measurement Methods .....	27
3.5.1	Ultrasonic.....	28
3.5.2	Deep Hole Drilling Method.....	29
3.5.3	Slitting (Crack Compliance) Method.....	30
3.5.4	Contour Method.....	31
3.5.5	Layer Removal Method .....	32
3.5.6	Sectioning Method .....	33
3.5.7	Diffraction methods.....	33
3.5.8	Method Selection Summary .....	34
4	Aims of Thesis.....	36
5	Railway axle design process.....	37
5.1	Bending and Press-fit Stress Field Determination.....	38
5.2	Residual Stress Field Determination.....	40
6	Developed Methodology for Residual Stress Determination.....	41
6.1	The Layer-Removal-Based Method .....	42
6.1.1	Analytical Iterative Evaluation of the Original Residual Stress State .....	46
6.2	The Sectioning-Based Method .....	51
6.3	Discussion and Validation.....	54
6.3.1	Additional Hardness and Microstructure Analysis .....	58
7	Stress Intensity Factor Determination.....	60
7.1	Compression Loaded Central Cracked Cylinder .....	60
7.1.1	The Model with a Flat Crack – Results and Discussion.....	64
7.2	The Investigated Railway Axle .....	73
7.2.1	The Investigated Railway Axle with the Surface Crack.....	73
7.2.2	The Investigated Railway Axle with the Internal Crack .....	78

8	Material Data Determination .....	84
9	Residual Fatigue Lifetime Estimation.....	87
9.1	Experimental Validation of the Estimated Residual Fatigue Lifetime .....	89
10	The Stochastic Residual Fatigue Lifetime Estimation.....	92
11	Conclusions.....	97
12	References.....	101
13	List of Abbreviations.....	112
14	List of Figures .....	116
15	List of Tables .....	120
16	Author's publication list and other activities .....	121
17	Curriculum vitae.....	123

# 1 Introduction

When designing a component of critical structures, the presence of a crack-type defect is often conservatively considered. The presence of the crack itself does not necessarily mean a failure of the component. The crack can originate in a manufacturing process or can occur during operational conditions. However, knowing of residual lifetime of components is crucial for the safe operation of the structure. Design of such parts where the failure of one component means failure of the whole system is often based on a damage-tolerant approach. The damage-tolerant considers crack presence in critical positions of the component. During the component design process, deciding whether the crack will propagate during structure operation (during cyclic loading, environmental conditions, etc.) is necessary. In the first case, regular inspections and their conditions (methods, intervals, critical spots, limit values, etc.) should be suggested. It is necessary to know the component's residual fatigue lifetime to specify a regular inspection timeline. Regular inspections ensure the safe operation of the component; however, they are usually very costly. An underestimation of residual fatigue lifetime increases operational costs, while overestimation of residual fatigue lifetime may lead to tragic consequences. However, residual fatigue lifetime estimation requires a lot of data to be known. Initial and final crack size, material behaviour, and total loading conditions are the most critical ones.



**Figure 1** Examples of some typical ways in which residual stress is developed in engineering materials [1]

Determining the initial crack length goes hand in hand with selecting the non-destructive testing method for defect detection. The initial crack length is mostly set based on the probability of defect detection for the used method and application. The dimensions of the component influence the determination of the final crack length. Material behaviour needs to be determined experimentally on the testing samples in the laboratories. External loading conditions are nowadays inspected by the numerical methods loads (e.g. finite element analysis), or they can be measured in-situ. However, internal loads such as residual stress are often unknown. The residual stress is

a consequence of most manufacturing processes. Important are mainly after welding, casting processes or surface heat treatment, see Figure 1. Knowing a component internal stress state is an essential initial condition for correctly estimating a residual fatigue lifetime. However, residual stress determination in sizable components is costly and time-consuming. Therefore, using conventional methods (like neutron diffraction) in the industry for residual stress determination in sizable components is rarely performed on a regular basis. The “new age “methods (like the contour method or deep hole drilling) are meant to be less time-consuming. However, specialized equipment necessary for such method performance is still costly for regular use in the industry.

Therefore, an original methodology for residual stress determination and its effect on residual fatigue lifetime will be shown in the present work. Thanks to the ongoing project of the Institute of Physics of Materials, the Czech Academy of Sciences, the methodology developed will be directly used in a new railway axle design process.

## 2 Theoretical background

### 2.1 Fracture Mechanics – Stress Intensity Factor

In the case of linear elastic fracture mechanics (LEFM), the stress field near the crack front can be described by the following equation [2]:

$$\sigma_{ij} = \frac{k}{\sqrt{r}} f_{ij,l}(\theta) + \sum_{t=2}^{\infty} A_t r^{\frac{t}{2}} g_{ij}^{(t)}, \quad (1)$$

where  $\sigma_{ij}$  is the stress tensor,  $r$  and  $\theta$  are polar coordinates,  $f_{ij,l}$  is the dimensionless shape function,  $k$  is constant which is related to the stress intensity factor (SIF or  $K$ ) ( $k = K/\sqrt{2\pi}$ ). For higher-order terms,  $A_t$  is amplitude, and  $g_{ij}^{(t)}$  is the dimensionless shape function for  $t^{\text{th}}$  term. The coordinate system is defined at the crack tip, as shown in Figure 2. The elastic solution shows a singular stress field near the vicinity of the crack tip (for  $r \rightarrow 0$ ), because first term is proportional to  $1/\sqrt{r}$ . Therefore, only this first term of eq. (1) is usually used to describe the stress field close to the crack tip because other terms are negligible for  $r \rightarrow 0$ . In some cases, the second, constant term is also used.

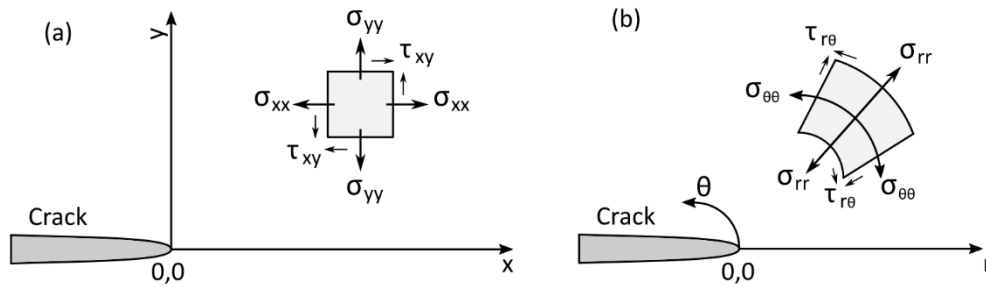


Figure 2 Stress components near crack tip a) cartesian coordinate system b) polar coordinate system [3]

Among the first who investigated solutions for the stress field near the crack were Westergaard [4], Irwin [5], Sneddon [6], Paris and Sih [7], and Williams [8]. Griffith [9], [10] was the first who proposed the theory that failure occurs when energy release rate  $G$  reaches its critical value  $G_c$ . Irwin [5] introduced the SIF and proposed that failure occurs when the SIF reaches its critical values  $K_c$ . In the LEFM, there is a direct relation between the SIF  $K$  and the energy release rate  $G$ :

$$G = \frac{K^2}{E'} \quad \begin{array}{l} \text{for plane stress: } E' = E \\ \text{for plane strain: } E' = \frac{E}{1 - \nu^2} \end{array}, \quad (2)$$

where  $E$  is Young's modulus, and  $\nu$  is the Poisson ratio. Therefore, the energy and the SIF approaches are essentially the same for the linear elastic material and two-dimensional solution.

A crack in the component can be loaded in three basic ways, see Figure 3. Mode I is the opening mode caused by the tensile loading, Mode II is the in-plane shear mode caused by the shear loading, and Mode III is the out-of-plane shear mode caused by the shear loading as well, but in the perpendicular direction, as shown in Figure 3. It is possible to load the crack in any combination of these three modes, which is called mixed-mode loading [11]–[13].

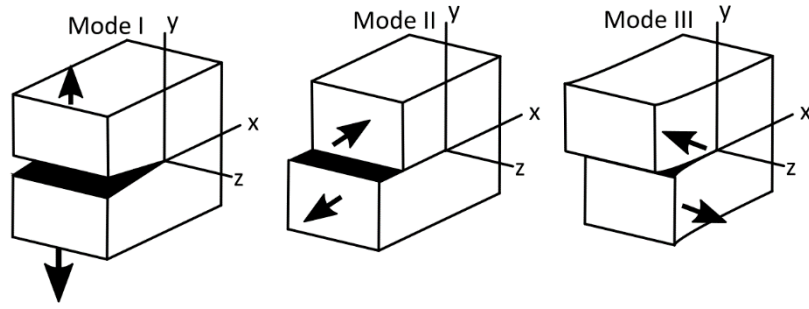


Figure 3 Modes of crack loading [14]

The SIF magnitude is dependent on the applied load, the crack length, and the geometry of the body with the crack. The SIF can be expressed as

$$K_I = \sigma \sqrt{\pi a} Y_I \left( \frac{a}{W} \right), \quad (3)$$

where  $\sigma$  is the far-field applied stress,  $a$  is the actual crack length and  $Y_I \left( \frac{a}{W} \right)$  is the function corresponding to the component geometry [15].

For the LEFM, individual components (corresponding to different loads, e.g. thermal and mechanical) of the SIF can be superimposed:

$$K_I^{total} = K_I^{(A)} + K_I^{(B)} + K_I^{(C)}. \quad (4)$$

However, SIFs in different modes cannot:

$$K^{total} \neq K_I + K_{II} + K_{III}. \quad (5)$$

The SIF is used in the linear elastic description of the material behaviour [12]:

1. The crack tip plastic zone has to be small compared to the component characteristic dimensions, e.g., crack length, uncracked width, a distance of crack tip to load application point, so-called small scale yielding condition[16], [17].
2. The crack grows in the homogenous, elastic, isotropic material.

For the SIF transfer from the test specimen to the actual component, as shown in Figure 4, it is necessary to consider the small region removed around the crack tip from both parts. The stress field in the boundary has to be described by equation (1). It is assumed that similar local loading leads to similar crack behaviour. It means that the singularity dominated zone (see Figure 4) is significantly bigger than the plastic zone near the crack tip and unaffected by the outer dimensions of the structure.

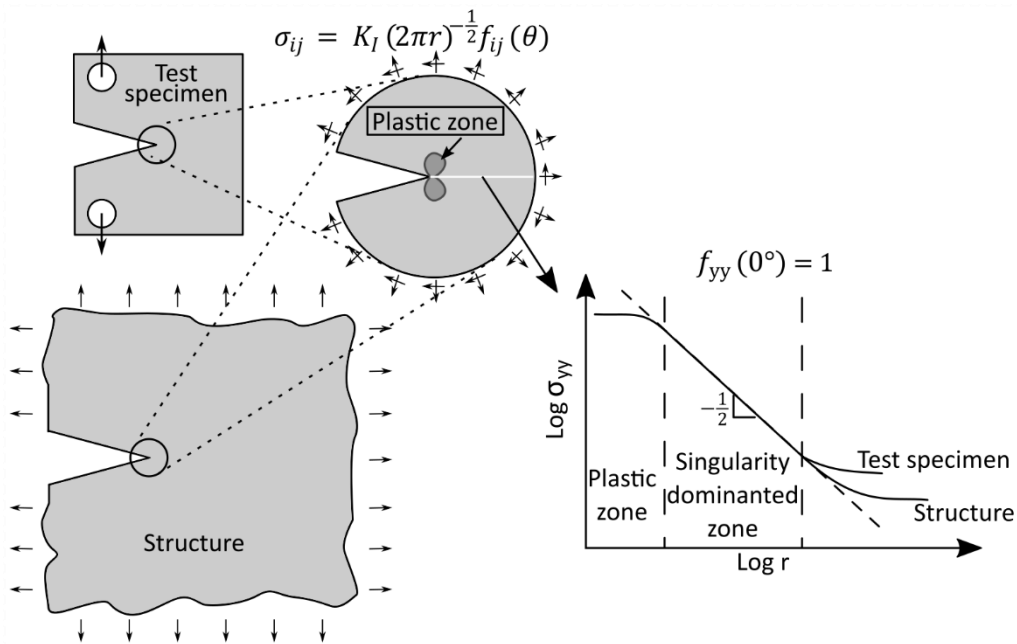


Figure 4 Schematic illustration of stress field portability from test specimen to actual structure [12]

## 2.2 Fatigue of Metals

From the engineering point of view, fatigue is connected with damage accumulation when cyclic loading is applied. The accumulation process consists of dislocation movement, localisation of plastic deformation, and consequent initiation and propagation of fatigue cracks. The final failure of the component occurs when the crack reaches its critical size ( $a \geq a_c$ ), or the maximal SIF (corresponding to applied load) exceeds the fracture toughness of the material ( $K_I \geq K_{Ic}$ ) [18].

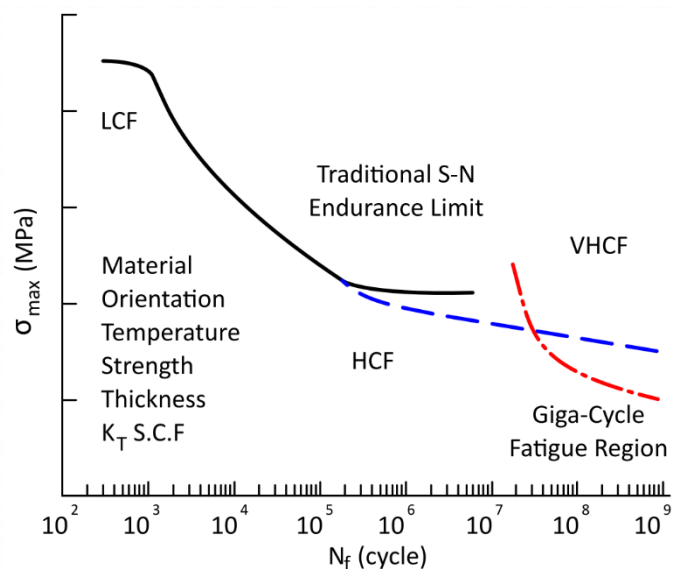
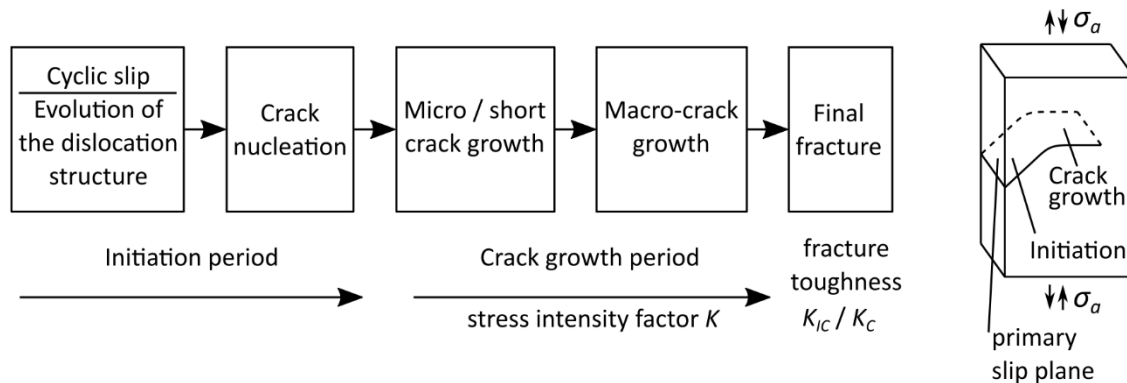


Figure 5 Typical stress-life (S-N) curve [19]

The fatigue lifetime of materials is characterised by the number of cycles to the failure; see Figure 5. While the number of cycles is less than  $10^4$ , we are talking about the low-cycle fatigue; between  $10^4$  up to  $10^7$  number of cycles it is so-called high-cycle fatigue, and when the number of cycles exceeds  $10^7$ , we talk about the giga-cycle (or the very high-cycle) fatigue [20], [21]. The Manson-Coffin curve typically characterises the low-cycle fatigue (fatigue failure is characterised

by plastic strain amplitude). Then, fatigue life can be described as:  $\varepsilon_{ap} = \varepsilon_f' (2N_f)^c$  where  $\varepsilon_f'$  is the fatigue ductility coefficient,  $N_f$  number of cycles to the failure and  $c$  the fatigue ductility exponent [22]. This description of the fatigue damage is used when the loading level is near the yield stress of the material. Contrary, a high-cycle fatigue regime is typically characterised by localised plastic deformations (fatigue failure is characterised by stress amplitude). Diagram stress – number of cycles to the failure is called the S-N or Wöhler (see Figure 5), named after August Wöhler [23], who was one of the first noticed dependence of the applied stress amplitude on the number of cycles to the failure for the railway axles. The high-cycle fatigue regime is characterised by the loading in the elastic regime of the material and localised plastic deformation. Typically fatigue strength of the material is defined for  $10^7$  cycles.

Nowadays, the fatigue life process is quite well described, see Figure 6. Fatigue life can be generally divided into the initiation and the crack growth periods. Those periods can be further divided into smaller parts.



**Figure 6 Different phases of the fatigue life with schematic illustration** [20], [24]

*The initiation period* – fatigue damage is typically initiated at the free surface (from the surface roughness after the manufacturing, artificial notches, scratches, or slip bands) or inside of the material in the vicinity of stress concentrators (from the material inhomogeneity or material discontinuities like defects after casting). In these areas is localised plastic deformation, and afterwards, first fatigue cracks are nucleated there. These small (microstructural) cracks can stop on grain boundaries or propagate further when cyclic loading is still applied.

*The crack growth period* – when a small crack becomes larger (about 1 mm or a few grain sizes), its propagation is relatively independent of the microstructure and can be described by fracture mechanics tools. Fatigue crack growth is well described by the SIF range, see Paris et al. [7], [25]–[28]. The curve crack growth rate vs the SIF range is a material property and can be obtained experimentally. Then, the residual fatigue lifetime (RFL) for a given initial crack can be estimated by integrating, see chapter 3.3 for details. Fatigue crack in this stage is not influenced by microstructure and usually propagates in a plane perpendicular to the loading axis (perpendicular to the maximum principal stress).

### 2.3 General Fatigue Design

All components and structures subjected to the cyclic loading are exposed to fatigue. Fatigue failures have caused many injuries and much financial loss (depending on literature, 80-90% of mechanical failures are case by fatigue). Therefore, it is necessary to prevent such failure during the design

process. Component fatigue criteria can be divided into four groups depending on a permissible load limit [29]–[33]:

1. *Infinite-life Design* – unlimited safety, is the oldest and the most conservative criterion. It requires local stresses or strains to be essentially elastic and safely below the pertinent fatigue limit.
2. *Safe-life Design* – the practice of designing for a finite life. A safe life must include a margin for the scatter of fatigue results and other unknown factors. The estimations may be based on the stress-life, strain-life, or crack growth relationships. Here appropriate regular inspections may not be practical or possible, and hence allowable service life must be less than the lifetime determined during the testing of the component. Alternatively, the estimated lifetime limit, determined during the component design process, is less than service life.
3. *Fail-safe Design* – requires the safety of the system after the failure of the part. The damage must not be fatal for all the system or any humans (e.g., failure of a lift cable is ensured by cabin brakes, “run-flat” tires enable driving even after the tire damage, etc.).
4. *Damage-tolerant Design* – assumes that defects (cracks) exist in the component. Cracks can be caused either by component processing or by material fatigue. The damage-tolerant approach uses the fracture mechanics analyses, and fatigue crack propagation tests to determine whether growing cracks will be large enough to cause the failure of a component. Limit intervals of the periodic inspection can be set to ensure the crack removal (e.g., by machining, typical for railway axles, or by welding) or the component repair or replacement before the final fracture occurs.

### 2.3.1 Damage-tolerant Design

A damage-tolerant approach should be employed when the component failure means failure of the system with severe consequences. This is the case of the railway axles. The failure of the axle can lead to a disaster with a number of victims. Pressure on the safety of critical components is even higher nowadays when the high-speed train operation speed is higher than 300 km/h.

Damage-tolerant design involves the complex analysis of how a critical component can fail. General input parameters for the damage-tolerant design are:

1. *Component geometry*.
2. *Loading conditions* – external loads (e.g. weight, applied loads), internal loads (e.g. residual stress).
3. *Material properties* – stress-strain curve, crack growth rate curve, ...
4. *Initial crack/defect information* – position (assumed) of initial cracks or defects, the shape of cracks, ... (this kind of information can be used as input information derived from service conditions or is predicted by the fracture mechanics analysis).
5. *The probability of detection curve* – is information on the probability of detecting cracks by non-destructive testing (should be determined for the particular technique and component).

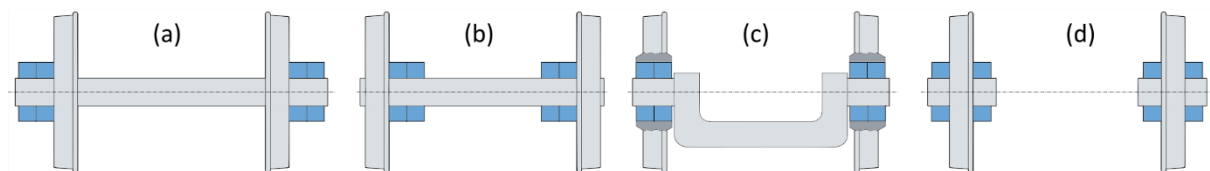
The main result of the damage-tolerant analysis is the estimation of the component's RFL (crack length vs loading cycles/time curve). It means how much time (how many cycles, etc.) does an initial defect (crack) (measured by non-destructive methods or specified based on the probability of the defect detection) needs to grow to its critical length causing the component failure.

### 3 Review

The presented work deals with sizable components. As a representative of such components, the railway axle was chosen to be investigated. Therefore, further in work, railway axle only is investigated and represents a common sizable component.

#### 3.1 Railway Axle Design

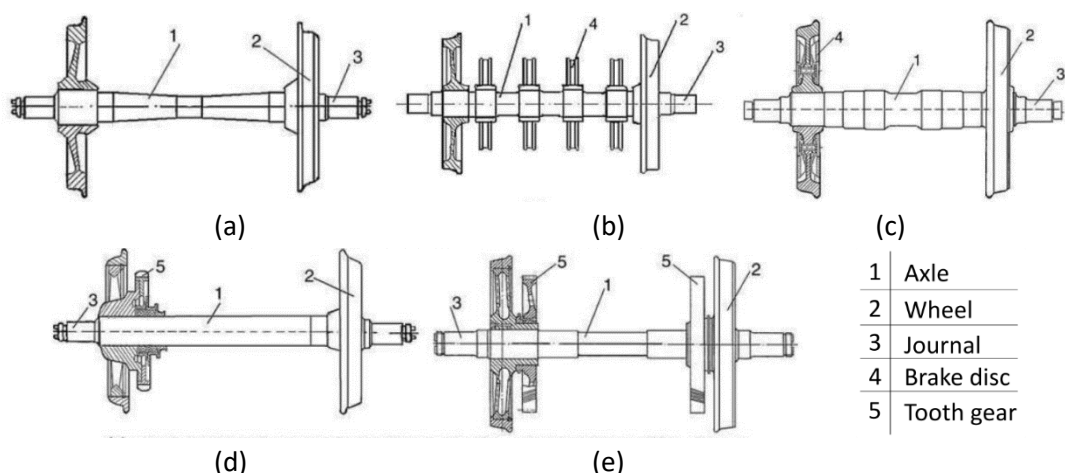
To design a railway axle, one first needs to look at the whole railway wheelset. Figure 7 shows the typical arrangement of railway wheelsets. Figure 7 a) shows the oldest, classic wheelset with outboard bearing standardised in the EU. Figure 7 b) shows a wheelset with an inboard bearing. This type has an advantage in axial bending moment reduction due to lateral forces. The wheelset is standardised in the UK [34]. Figure 7 c) shows an independently rotating wheel arrangement with an axlebridge. This wheelset is used for low profile vehicles like trams. Figure 7 d) shows an independently rotating guided wheels arrangement. This particular wheelset is used for special railway track applications.



**Figure 7 Wheelset design types; a) outboard bearings arrangement, b) inboard bearing arrangement, c) the axlebridge design principle, d) independent wheel arrangement with bearings on both sides [35]**

Figure 8 shows a general outboard bearing wheelsets arrangement. The axle design further depends on:

1. The type of the axle (traction or trailing).
2. The type of braking system (shoe brake, brake disc on the axle, brake disc on the wheel, ...).
3. The construction of the wheel centre and the position of bearings.
4. The construction of resilient elements to limit higher frequency forces.



**Figure 8 Types of wheelsets with external journals; a) pure wheelset, b) wheelset with brake discs on the axle, c) wheelset with brake discs on the wheels, d) wheelset with asymmetric gear position, e) wheelset with symmetric gears position [36]**

European railway axle design is mainly based on EN 13103-1 and EN 13261 standards [37], [38]. For the engineering design, the axle is simplified as a beam loaded by the static forces while nominal

forces (force from vehicle mass, braking and traction forces) are calculated. Real axle geometry is then taken into account by multiplying the nominal stress by the stress concentration factors for different axle parts. Obtained stress values are compared with the endurance limit value multiplied by the safety factor. Endurance limit has to be obtained experimentally while S-N curve determination. In the past, there were no other effects included in standards. In last years, standards were updated, and the stress caused by the press-fit is now included in EN 13261 standard. European Committee for Standardization accepted technical report CEN/TR 17469 [39] as a result of the EURAXLES project. The technical report is not mentioned to replace accepted standards but as a recommendation for further steps to be taken in the axle design process. One of the main improvements is the finite element method (FEM) simulation to estimate the stress concentration. However, there is still a place for improvement.

Railway axles are historically produced according to UIC standard 811 [40], which originally specified five steel grades (A1=C35, A2=22MnCrV5, A3=C45, A4=25CrMo4, A5=42CrMo4). EU standards on the axle design include only A1 and A4 steel grades [41]. Railway axle steel can be further labelled as N for normalised (i.e., EA1N) or T for quenched and tempered (i.e., EA4T).

Axle improvements developed in time and used include coating application (see, Figure 9) or surface treatment to improve impact resistance and fatigue properties. The next improvement is the axle produced with an axial bore, the so-called “hollow axle” (advantages will be discussed in the next section).

Other development is going on in order to improve traditional axle design. Bracciali [42] proposed a wheelset arrangement where the wheel can be disassembled with a procedure where the bogie frame only is lifted and some screws removed. The design is intended to reduce maintenance. Another axle design using modern materials is the composite axle proposed by Mistry et al. [43]. Figure 10 shows both axle designs.



Figure 9 Example of coated axle [44]

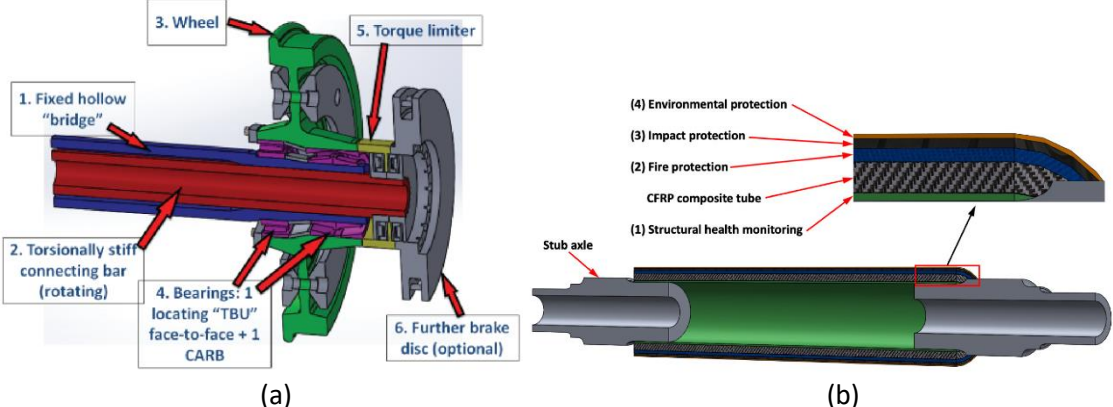


Figure 10 New axles in development; (a) axle with torque limiter [42], (b) composite axle [43]

Despite different standards, current customers require numerical and experimental evidence for the guaranteed mileage without failure or the guaranteed mileage between maintenance inspections. Such requirements are getting harder with the arrival of high-speed trains. Guaranteed mileage for such a massive component as the railway axle requires the fracture mechanics analysis (Damage-tolerant design described in the previous section). For the RFL estimation purposes, the initial crack length is equal to the minimal crack length, which can be found by the axle non-destructive testing (NDT). Using the NDT method affects the considered minimal crack length and significantly affects the estimated RFL.

3.1.1 Non-Destructive Testing and Probability of Detection

The axle NDT is typically done by magnetic or ultrasonic testing methods. An inspection can be done only from the outer surface in the solid axle case. The hollow axle NDT is possible from the inside of the axle. An ultrasonic testing probe can be inserted into the axle bore, and an NDT inspection can be performed without coating removal. Figure 11 shows a schematic illustration of ultrasound inspection of the position under the wheel by outer high angle scan and inside bore scan.

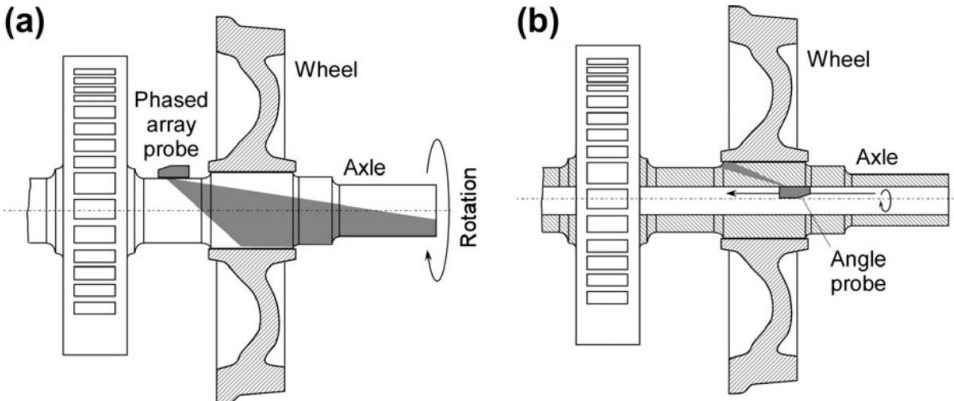
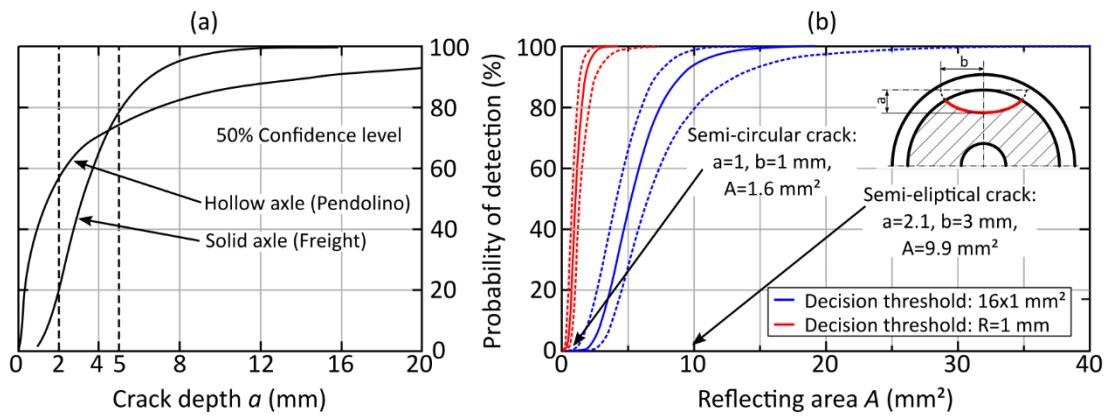


Figure 11 Ultrasound testing probe position: (a) solid axle, (b) hollow axle [45]

Figure 12 a) shows the ultrasonic testing probability of detection (PoD) curves comparison for solid and hollow axle determined below the WIDEM project [46] in 2008. One can see that for small cracks, the hollow axle has a higher probability of catching the crack; however, for the 20 mm crack length, the probability is about 90 %. On the other hand, classical near-end inspection reaches a very high probability for the 12 mm crack length. For about 4 mm crack length, both methods have the same PoD of the crack. In 2016 Carboni et al. [47] proposed a master PoD curve (Figure 12 b) in terms of defect reflected area developed for the third generation of bore ultrasound sensor. PoD curve shows very high sensitivity for semi-elliptical like cracks. For 2 mm (about 10 mm<sup>2</sup>), crack length probability is close to 100%.

It should be mentioned that PoD data should be determined for particular geometry, material and application. PoD data are also highly dependent on the NDT methods used to produce them. It is often assumed that the smallest flaw detected is a good measure of PoD, but there is usually a large gap between the smallest flaw detected, and the largest flaw missed [48], [49].

Estimating the proper PoD curve and the initial crack for the residual lifetime estimation is an integral part of the damage-tolerant approach. Several PoD models are presented by Gray et al. [50] or by other authors [47], [51], [52] in terms of railway axles. More information about the determination of PoD curves can be found in [53]–[56].



**Figure 12 (a) PoD curve comparison for solid and hollow axle [46], (b) Master PoD curve through naturally fatigued cracked hollow axles [47]**

Determination of the PoD curve is not part of the presented work. Therefore, minimal crack length further used in the damage-tolerant analysis is set up by a discussion with representatives of BONATRANS GROUP a.s and the requirements of their customers.

### 3.2 Residual fatigue lifetime of the railway axle with the crack

One of the last customer's requirements is extending the axle's inspection interval from about 30 000km [41] up to 500 000 km [57] or up to 1 000 000 km [58]. Such improvement means high economic savings in terms of operating costs. Therefore, customers are looking forward to extending the inspection interval length.

#### 3.2.1 Investigation of the railway axle with the crack

Figure 13 shows typical positions of the crack on the railway axle surface. Fatigue crack can initiate under the press-fit area from fretting corrosion pits, from corrosion pits at the shaft area or near the T-notch geometrical stress concentrator. Crack initiation at the U or V-notch is typically associated with an overheating of bearings. Most of the cracks are initiated on the free surface of the axle [45], [59]. Presented work deals with fatigue cracks initiated from geometrical stress concentrators.

The SIF for railway axles is typically obtained by the numerical simulation of the undamaged axle in combination with the simplified analytical model (developed by Wang and Lambert [60], [61]) for the semi-elliptical surface crack in the plate [62], [63]. Figure 14 shows how far is this simplified analytical model from the real axle geometry. Therefore, this kind of solution can be used in limited conditions, even with the inevitable inaccuracies. Limiting conditions are short crack lengths (the stress field in the axle has to be similar to the bent plate), and the crack has to grow from the axle surface. Fatigue crack initiation and growth from the axle surface is the basic assumption in the standard axle design. However, with the effort for the compressive residual stress field at the axle surface, there is a possibility for the sub-surface crack growth. Therefore, the simplified plate analytical model is not relevant enough, and further investigation is necessary. Another option for RFL estimation is using the specialised software INARA for the surface semi-elliptical crack growth in railway axle, developed in the framework of the research project EBFW 3, where the SIF is obtained by analytical solution with improved weight function [64]–[67]. However, analytical procedures assume surface crack growth as well.

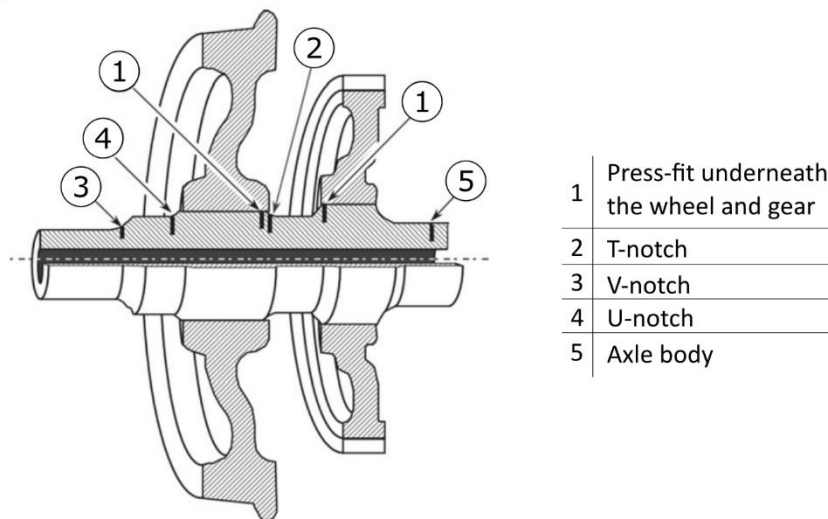


Figure 13 Typical fatigue crack locations for the railway axle [45], [59]

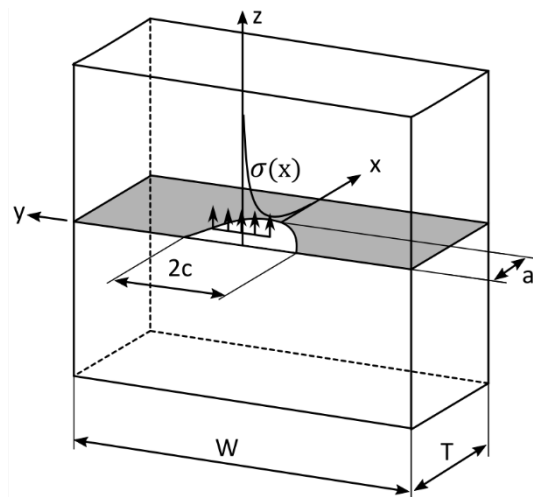


Figure 14 Scheme of a crack in bent plate. The basic model for SIF estimation [61]

A numerical investigation of the railway axle with surface crack was performed by several authors [68]–[75]. Madia et al. [62] provided a collection of SIF solutions for different surface crack positions. The numerical model for the axle is generally modelled with the press-fitted wheel. However, the application of boundary conditions differs due to simulated loading. Press-fit loading can be simulated by the wheel and axle geometrical overlap or by the theoretical overlap applied in the software. The bending load can be applied in two ways. The first is applying the force in journal positions and restricting the degrees of freedom at the wheel (where the wheel and railway are in contact). The second is applying the moment loading condition at the one end of the axle and restricting the degrees of freedom at the other end of the axle. Both methods, for press-fit and bending load, are interchangeable and provide similar results.

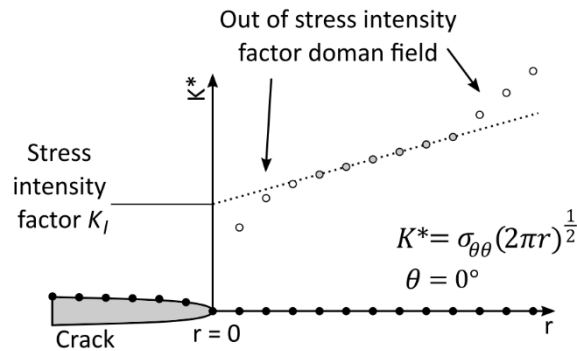
### 3.2.2 Stress Intensity Factor Determination for the Railway Axle with a Crack

Another critical part of railway axle numerical investigation is an estimation of the SIF. There are several possibilities for the SIF determination by FEM. For example: the stress or the displacement correlation, global energy or compliance, domain (volume) integral, interaction integral or crack tip singular elements [3], [12], [76], [77]. Further in the text are described methods used in presented work only.

*Stress correlation* (also called the “direct method”) is one of the basic methods to determine the SIF from the finite element (FE) analysis. SIF can be determined from the stress field near the crack tip. Therefore, we can use the (1) formula, and for angle  $\theta = 0$  and mode I we obtain:

$$K_I = \lim_{r \rightarrow 0} \sigma_{yy} \sqrt{2\pi r}, \quad (6)$$

where  $\sigma_{yy}$  is the opening stress (for  $\theta = 0$ ;  $\sigma_{yy} = \sigma_{\theta\theta}$ ),  $r$  is the distance from the crack tip, see Figure 15. By FEM simulation, one obtains the stress field near the crack tip and calculates the SIF for certain stress positions, as shown in Figure 15. Finally, by the linear extrapolation to the  $r = 0$  one obtains the SIF for a given crack length. The SIF for modes II and III can be estimated similarly. It is necessary to change the opening stress for the shear stress  $\sigma_{xy}$  or  $\sigma_{zy}$  for mode II or III, respectively.



**Figure 15 SIF ahead of the crack tip with extrapolation value for estimation of SIF at the crack tip [12]**

The advantages of this method are simplicity, no unique elements are needed, only one analysis is performed, and only simple post-processing is required. However, the main advantage of this method is that it provides information about the quality of the solution. Compared to other methods, this method does not require the definition of plane strain or plane stress condition. Therefore, it can be easily used for 2D and 3D determination. The disadvantage is that fine mesh is required for an accurate result. This procedure is not implemented in the commercial FEM software; therefore, the own post-processing is needed.

*The interaction (energy) contour integral* method is derived from the standard J-integral method [78]. Integral is path independent for elastic materials. For the homogenous material it has the form:

$$J = \oint_{\Gamma} \left( W dy - T_i \frac{\partial u_i}{\partial x} \right) d\Gamma, \quad (7)$$

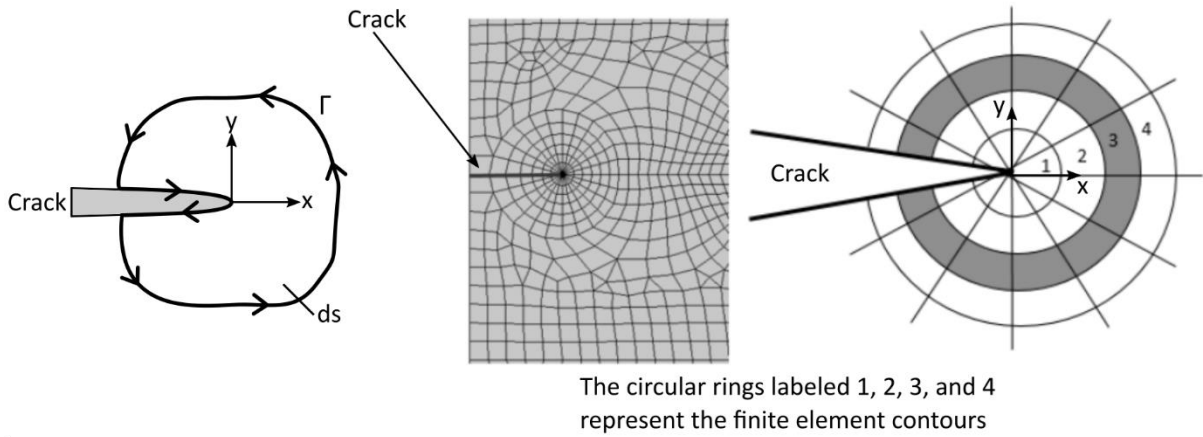
where  $\Gamma$  is the integration path shown in Figure 16,  $W$  is a strain energy density,  $u_i$  is a vector of displacements, and  $T_i$  are components of the line load acting perpendicular to the integration path  $\Gamma$ . Strain energy density  $W$  can be expressed as:

$$W = \int \sigma_{ij} d\varepsilon_{ij}. \quad (8)$$

The line load components  $T$  can be expressed as:

$$T_i = \sigma_{ij} n_j, \quad (9)$$

where  $d\varepsilon$  are strain components and  $n$  are the outward unit vector components normal to an arbitrary contour enclosing the crack tip.

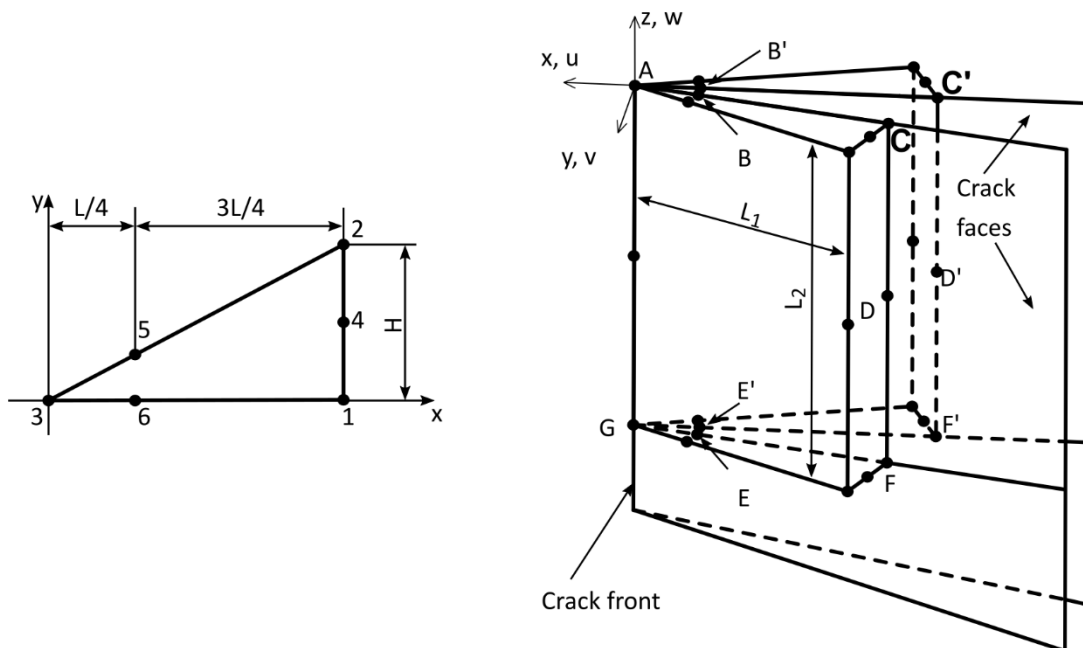


**Figure 16** Integration path used for the calculation [79], [80]

The energy release rate  $G$  and the  $J$ -integral value are equal for the linear elastic material. Therefore, the SIF can be determined by (2) substituting the  $J$  value for the  $G$  value. The SIF is typically evaluated for several contours to exclude numerical errors, and the final SIF determination is made as the mode value of those values.

Advantages of this method are that it is often implemented in commercial software, has high accuracy for the coarser mesh, and can evaluate fracture parameters for plastic materials as well. The disadvantage is that the mesh is sensitive to the shape and quality near the crack tip area.

*Crack tip singular elements.* Numerical SIF determination is based on the stress field around the crack tip. However, the crack tip causes singular stress in the elastic material. Therefore, using the special singular elements to describe such singularity is recommended. Quarter-point singular elements are derived from standard elements. There are more possibilities for how it is done, for example, see [81], [82]. Generally, the mid-size node is moved from  $1/2$  to  $1/4$  distance of the element size, closer to the crack tip, as shown in Figure 17. Node movement helps to obtain  $1/\sqrt{r}$  singularity.



**Figure 17** 2D and 3D singular element [81]–[84]

With singular elements, fewer elements are required near the crack tip region for obtaining the appropriate stress field required for the different SIF evaluation methods. Singular elements allow us to evaluate the SIF directly from node displacements on these elements. Necessary equations are described in [83], [84].

The disadvantage of using singular elements lies in its generation for 3D geometries. However, this may vary for the used software.

### 3.3 Residual Fatigue Lifetime Determination for the Railway Axle

As was mentioned in the previous sections, the damage-tolerant approach considers the crack in critical locations. With a defect in a critical position, the RFL for the component can be estimated for some initial crack length. Estimation is determined by integrating the crack growth curve.

Figure 18 shows a typical crack growth rate  $v$  curve vs the SIF range  $\Delta K$ , also called the  $v$ - $K$  curve. This curve can be divided into three regions:

1. *I – threshold region* – the crack growth rate is near the threshold value of the SIF. If the SIF values are below the threshold, the crack is not propagating.
2. *II – linear crack growth region or Paris-Erdogan region* [25] – the crack growth rate in this region is stable. In the logarithmic scale,  $da/dN$  vs  $\Delta K$  looks like a straight line. The Paris-Erdogan formula describes this region, as:

$$v = \frac{da}{dN} = A(\Delta K)^m, \quad (10)$$

where  $da/dN$  is the crack extension in a single cycle (crack propagation rate), and  $A$  and  $m$  are material constants measured experimentally.

3. *III – stable-tearing crack growth region* – the crack growth rate in the stable-tearing crack growth region is high. Values of the SIF are getting close to the critical value  $K_c$ , and the crack starts to grow unstable, which leads to the final break.

RFL is typically estimated by integrating the formula approximating the  $v$ - $K$  curve like (10). The crack growth rate can be replaced by the effective SIF  $K_{eff}$  in this formula.  $K_{eff}$  considers the effect of the crack closure like the plastic zone around the crack tip [85]:

$$v = \frac{da}{dN} = A^*(\Delta K_{eff})^m, \quad (11)$$

where material constant  $A^* \neq A$ .

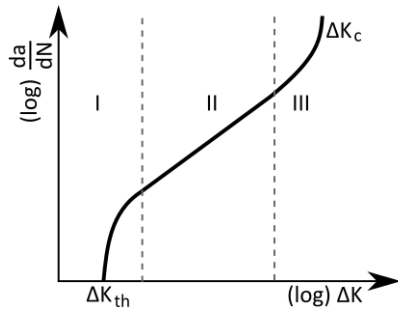
However, the Paris-Erdogan formula describes only region II of the  $v$ - $K$  curve. It means that regions I and III are not described. This lack was removed in the NASGRO approach, where terms describing the curvature of the  $v$ - $K$  curve were added [86], [87]:

$$v = \frac{da}{dN} = C \left( \left( \frac{1-f}{1-R} \right) \Delta K \right)^n \frac{\left( 1 - \frac{\Delta K_{th}}{\Delta K} \right)^p}{\left( 1 - \frac{K_{max}}{K_c} \right)^q}, \quad (12)$$

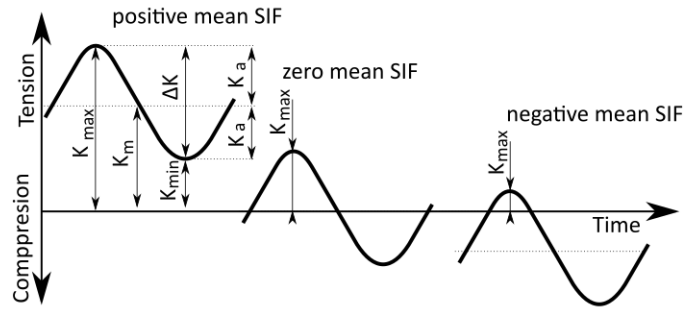
where  $C$ ,  $n$ ,  $p$ ,  $q$  are material constants. Constant  $p$  corresponds to the degree of curvature in the I region (threshold region) of the  $v$ - $K$  curve. Constant  $q$  corresponds to the degree of curvature

in the III region (stable-tearing crack growth region) of the  $v$ - $K$  curve.  $R$  is the stress ratio of the cycle (see Figure 19 for different ratios), and  $f$  corresponds to crack closure effects in the vicinity of the crack tip.

NASGRO approach was developed in the aircraft industry. However, for its complexity has become popular for determining the RFL of engineering structures in different engineering areas as well [59]. Other used formulas for the description of the  $v$ - $K$  curve are Forman [88], Priddle [89], Walker [90], Klesnil and Lukáš [91], etc.



**Figure 18** Three regions of a crack growth rate as a function of  $\Delta K$



**Figure 19** Description of the loading cycle

### 3.3.1 Influence of Residual Stress on Residual Fatigue Lifetime

It is known that the tensile residual stress contributes to the crack propagation and the compressive residual stress reduces the magnitude of the loading stress [20], [33], [92]–[96]. The residual stress can be considered in a given spot as local static loading. The mean SIF influences the opening and closing state in terms of the loading cycle (Figure 19). Residual stress affects the component of the mean SIF value  $K_m$ .

$$K_m = \frac{K_{max} + K_{min}}{2}, \quad (13)$$

where  $K_{max}$  and  $K_{min}$  are the maximum and minimum SIF in a given stress cycle, respectively. In other words, residual stress affects the SIF ratio  $R$ :

$$R = \frac{K_{min}}{K_{max}}. \quad (14)$$

Hutař [97], Schindler [98] and Pokorný [99] showed that a relatively small compressive residual stress can substantially impact RFL. Therefore, further study of the residual stress effect on the RFL is essential for a deeper understanding of fatigue damage of structures.

## 3.4 Residual Stress – Review

The following section describes the theoretical background of the residual stress, and the next one reviews common methods for the investigation of residual stress in engineering components.

### 3.4.1 Background and Definition of Residual Stress

Residual stress is “locked-in” stress that exists in material, whether metallic or not (polymer, glass, ceramic, wood, etc.), independent of the presence of any external loads. Residual stress is difficult to assess because it is self-equilibrating. So, unlike applied stress, it cannot be calculated from the forces, impulses, and couples experienced by a material, component, or assembly [1], [100]–[107].

### 3.4.2 Production of Residual Stress

Almost all manufacturing processes create residual stress. Further, stress can also develop during the service life of the manufactured component. Such stress develops as an elastic response to incompatible local strains within the component, for example, due to non-uniform plastic deformation. The surrounding material must then deform elastically to preserve dimensional continuity, creating residual stress. The mechanisms for creating residual stress include [104], [108]:

1. *Non-uniform plastic deformation* – manufacturing processes that change the shape of the material, including forging [109], rolling [110], bending [111], drawing and extrusion [112], and in-service during surface deformation, as in ball bearings and railway rails.
2. *Surface modification* – manufacture during machining [113], grinding [114], plating [115], peening [116], [117], and carburizing [118], and in service by corrosion.
3. *Material phase, often in the presence of significant thermal gradients* – manufacture during additive manufacturing [119], welding [120], casting [121], quenching [122], phase transformation in metals and ceramics, precipitation hardening in alloys, and polymerisation in plastics, as well as in service from radiation damage in nuclear reactor components and moisture changes in wood.

### 3.4.3 Effect of Residual Stress

It has been proven that compressive residual stress has a beneficial effect on the fatigue life, crack propagation, and stress corrosion of materials. In contrast, tensile residual stress reduces material performance capacity. For many applications, the properties of a part's surface are dominant for the functional behaviour of the whole component. James and Lu [108] stated that the residual stress can be added as a static load. While the residual stress is maintained in the elastic region of the material's loading capability, the principle of superposition of different types of stresses applies. It means that as a result of surface treatment is the compressive residual stress, and if there is applied tensile stress, the actual stress which acts in the material is less than typically. It can thus be seen that the residual stress acts as mean stress and can affect the mechanical behaviour of materials. The residual stress can affect friction, chemical resistance, magnetisation, optical, acoustic, or thermal properties of components [100], [103].

### 3.4.4 Residual Stress Length Scales

Figure 20 illustrates how the different types of stress equilibrate over the different length scales. The macro-stress is continuous across phases for a two-phase material, but the type II and III stresses are not. As a result, even when the sampling area is greater than the characteristic areas for type II and type III, non-zero phase-average micro-stresses  $\langle \sigma_1 \rangle_A^{II,III}$  and  $\langle \sigma_2 \rangle_A^{II,III}$  can be recorded. Considering the stresses in the Z direction:

$$0 = \int_A \sigma_{zz}\{x, y\} dA_z = \int_{A_1} \sigma_{zz}\{x, y\}^{II} dA_z + \int_{A_2} \sigma_{zz}\{x, y\}^{III} dA_z, \quad (15)$$

$$0 = f_A \langle \sigma_1 \rangle_A^{II} + (1 - f_A) \langle \sigma_2 \rangle_A^{III}, \quad (16)$$

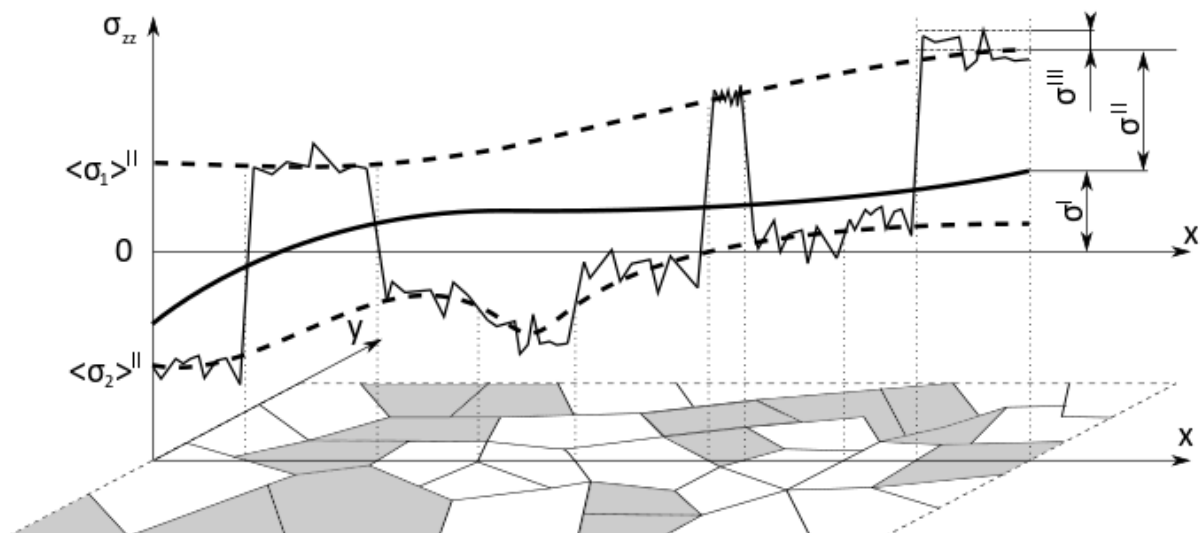
where  $f_A$  and  $(1 - f_A)$  are the area fractions  $A_1/A$  and  $A_2/A$  respectively. Extending the analysis to three dimensions by integrating over the sampling volume, the type II volume average phase stresses ( $\langle \sigma_1 \rangle^{II}$  and  $\langle \sigma_2 \rangle^{III}$ ) must obey

$$0 = f\langle\sigma_1\rangle^{II} + (1 - f)\langle\sigma_2\rangle^{II}. \quad (17)$$

Suppose the sampling volume is larger than the characteristic volume for type II. In other words, while the type II and type III stresses must balance over the appropriate small distance, there may be a phase-dependent residual effect over large distances; this leads to mean background stress in each phase [1], [123].

To summarise, residual stresses can be classified as:

1. *Type I* – macro residual stress develops in the body of the component on a scale larger than the grain size of the material.
2. *Type II* – micro residual stress that varies on the scale of the individual grain. Such stresses may be expected to exist in single-phase materials because of anisotropy in the behaviour of each grain. They may also develop in multi-phase materials because of the different properties of the different phases.
3. *Type III* – micro residual stress exists within a grain, essentially due to the presence of dislocations and other crystalline defects. Types II and III are often grouped as micro-stresses.



**Figure 20 Residual stress distribution over several grains of a two-phase material showing the three kinds of residual stresses [1], [101], [107]**

### 3.5 Overview of Residual Stress Measurement Methods

The residual stress cannot be directly measured, which is rather unfortunate. There are no simple techniques for measuring this stress. All techniques measure some other entity. For destructive techniques, strain or deflection is often measured, and residual stress is calculated based on known relations to stress.

This section summarises residual stress measurement techniques that can investigate the residual stress across the whole cross-section of the actual components. Due to ongoing projects, the requirement is to measure residual stress through the whole cross-section of the railway axle (diameter of more than 150 mm). It is necessary to employ the technique capable of penetrating a great depth, is repeatable in real-time, and is affordable.

Detailed descriptions for the commonly used residual stress measurement technique can be found in [1], [107], [124]–[126]. In general, residual stress measurement techniques are sorted by the level of destruction of the measured sample, possible penetration depth, and technique resolution. Other factors for choosing the appropriate measurement technique are material issues, precision, difficulty of measurement, available equipment, and cost.

Figure 21 shows a comparison of these techniques in terms of penetration depth. As one can see, only a few techniques are possible for the deeper measurement of the residual stress. In terms of destruction, there seem to be only two possibilities. Therefore, next will be briefly described only techniques with the potential of measuring the whole cross-section of the railway axle. And X-ray diffraction, which is the most common technique for residual stress investigation.

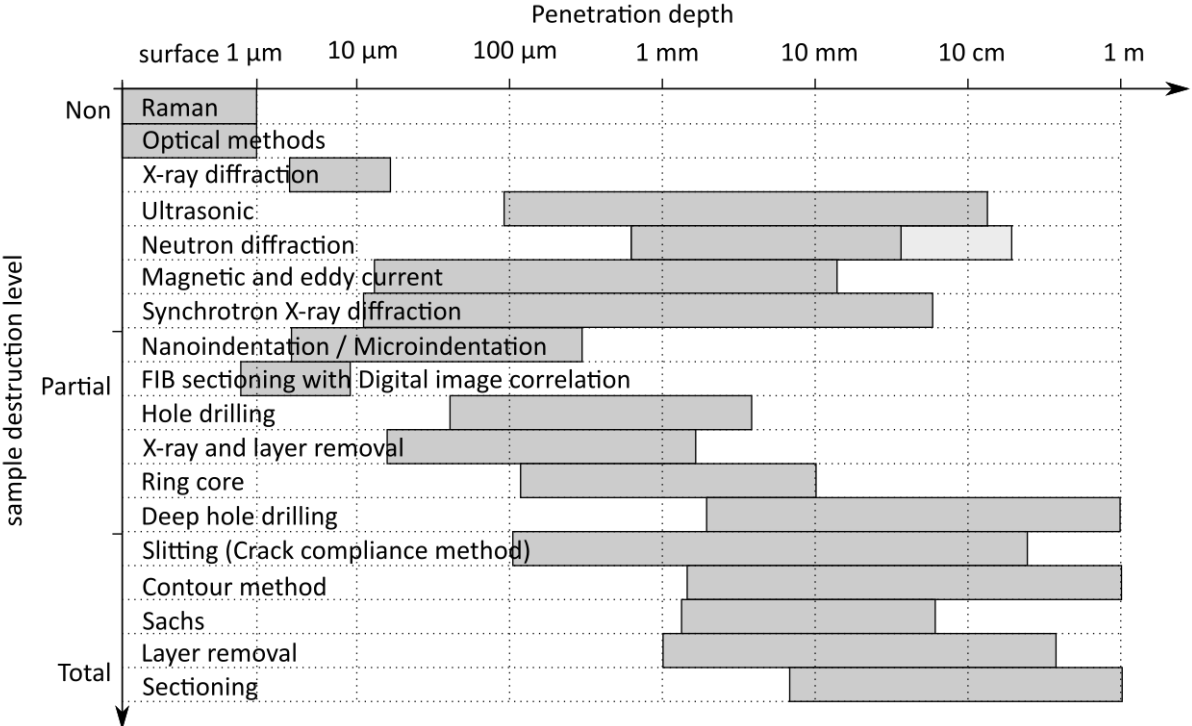
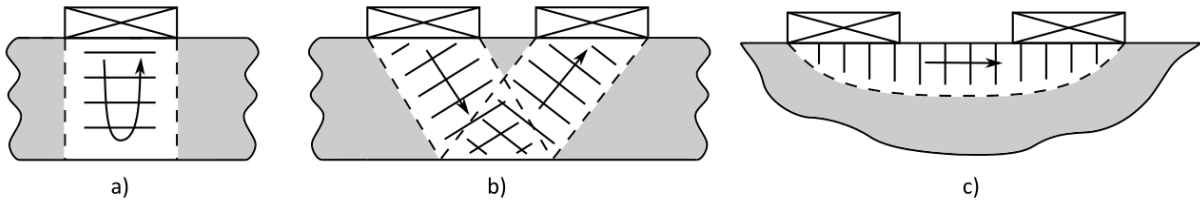


Figure 21 Comparison of different residual stress measurement techniques [107], [111], [125]

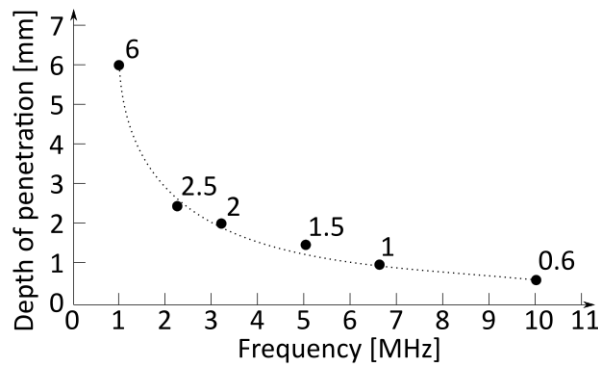
### 3.5.1 Ultrasonic

The ultrasonic stress measurement technique is based on the acoustic-elasticity effect, according to which the velocity of elastic wave propagation in solids is dependent on the mechanical stress. Within the elastic limit, this correlation is known as the acoustoelastic effect. The acoustoelastic effect means that the flight time of the ultrasonic wave changes with the stress. In 1967, Crecraft [127] showed that the acoustoelastic law could be employed for stress measurement in engineering materials. Different types of ultrasonic testing methods have been developed, such as the ultrasonic longitudinal wave [128], ultrasonic shear wave [129], a combination of shear wave and longitudinal wave [130], ultrasonic surface wave [131], ultrasonic guided wave, nonlinear ultrasonic [132], and ultrasonic critically refracted longitudinal wave ( $L_{CR}$ ) [133] methods.



**Figure 22 Schematic view of ultrasonic measurement configurations: a) through-thickness with one transducer, b) through-thickness with two transducers, and c) surface with two transducers [134]**

In Figure 22, one can see different experimental configurations that can be used for residual stress measurements. In each case, waves are launched by a transmitting transducer, propagate through a material region, and are detected by a receiving transducer. Thus, the configurations shown in Figure 22 a) and Figure 22 b) through-thickness average of the stress is sensed. In the configuration shown in Figure 22 c), the stress in a surface layer is sensed. The depth of this layer is related to the ultrasonic wavelength. Figure 23 shows the accessible depth function of transmitted frequency published in [135].



**Figure 23 Function of penetration depth on ultrasonic frequency [135]**

### 3.5.2 Deep Hole Drilling Method

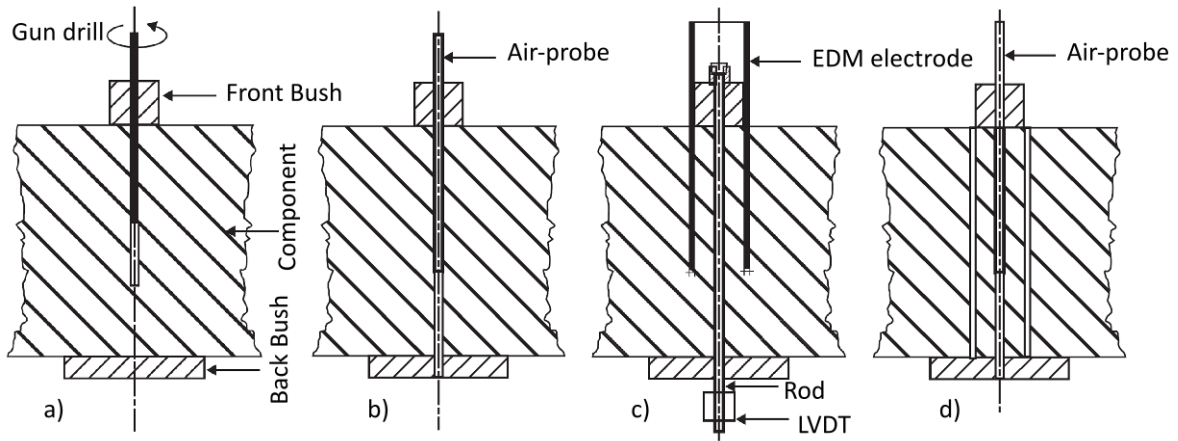
The Deep Hole Drilling (DHD) method belongs to the class of mechanical strain relaxation techniques designed to measure the stress and residual stress in the material. Its origins as a technique rise from its use in rock mechanics [136]–[139]. The term “Deep Hole Drilling” has been adopted to describe the method to distinguish it from near-surface residual stress measurement methods such as centre hole drilling. DHD procedure is schematically described in Figure 24. Figure 25 is the FEM simulation of DHD to understand better what is going on during the drilling of the reference hole and trepanning the ring core. The DHD method estimates the through-thickness residual stress distribution in a component by measuring the change in diameter of the reference hole that occurs when a core of the material is removed from the component by trepanning. The difference in the reference hole diameter,  $\Delta d(\theta, z)$ , is calculated according to

$$\Delta d(\theta, z) = d'(\theta, z) - d(\theta, z), \quad (18)$$

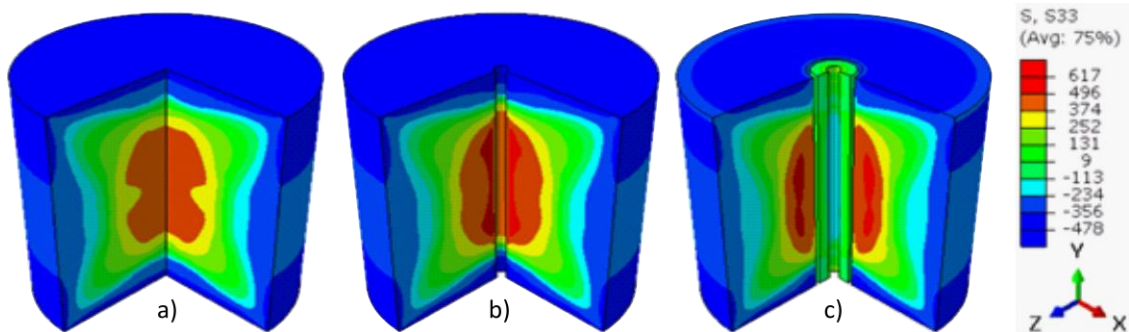
where  $d$  and  $d'$  are the reference hole diameters before and after trepanning, respectively, each function of the angular orientation around the hole,  $\theta$ , and depth through the core thickness,  $z$ . The changes in reference hole diameter are then converted to strain using

$$\tilde{\varepsilon}(\theta, z) = \frac{\Delta d(\theta, z)}{d_0}, \quad (19)$$

where  $d_0$  is the nominal reference hole diameter (and is independent of  $z$ ). The reference hole strains  $\tilde{\varepsilon}(\theta, z)$  are related to the reference hole axis,  $\sigma_{xx}(z)$ ,  $\sigma_{yy}(z)$  and  $\sigma_{xy}(z)$ , through an elastic analysis [140]–[143].



**Figure 24** schematic illustration of DHD technique a) attachment of reference bushes and gun-drilling reference hole, b) measurement of the diameter of reference hole through the depth of hole c) trepanning of material around the hole (core) often by electro-discharge machining, d) final diameter measurement of residual stress-free reference hole [140]



**Figure 25** FEM simulation of the DHD method a) original specimen b) specimen with gun-drilled hole c) specimen with a trepanned cylinder around hole [144]

Many developments have been made over recent years [145]–[147]. The aim was to increase the accuracy and applicability of the DHD method to a range of engineering materials and components. The last development of the DHD technique and summarised state of the art is done by Brermann [148].

### 3.5.3 Slitting (Crack Compliance) Method

The slitting method, also known as the crack compliance method, is one of the relaxation methods. The slitting method (see Figure 26) uses a cut of incrementally increasing depth to release the residual stress on a plane perpendicular to the cutting plane. At the same time, the deformation is recorded. From the change of geometry, the residual stress component can be determined. Obtained stress results are averaged through the whole cut increment. The method initially developed by Finnie and co-workers [149]–[154] has been reviewed in detail by Prime [155]. Further findings are published in [156]–[159].

After the successful experiment and component deformation recording, the residual stress is determined. Stress computation assumed a polynomial basis for the stress versus depth profile, elastic superposition, and a linear system developed using finite element analysis. The residual stress as a function of depth  $\sigma_{yy}(x)$  was assumed to be described by a polynomial expansion of order  $m$

$$\sigma_{yy}(x) = \sum_{j=2}^m A_j P_j(x) = [P]\{A\}, \quad (20)$$

where  $P_j(x)$  are Legendre basis interpolation functions and  $A_j$  are a set of coefficients to fit the measured data. Then, by measuring strain  $\varepsilon$  corresponding to different crack depths, the flexibility function  $C$  is obtained by

$$\varepsilon(a) = \sum_{j=2}^m A_j C(a, P_j) = [C]\{A\}. \quad (21)$$

Therefore, the undetermined coefficient matrix  $A$  is obtained according to

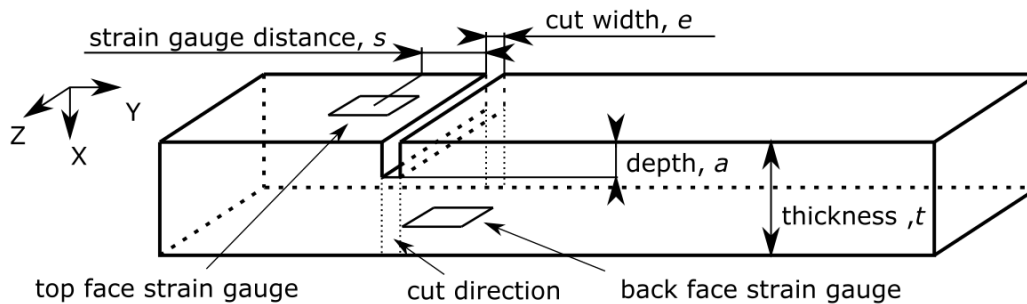
$$\{A\} = ([C]^T [C])^{-1} [C]^T \{\varepsilon_{measured}\}, \quad (22)$$

furthermore, the residual stress value along the depth distribution is obtained.

For investigation of residual stress influence on fatigue crack growth, it is possible to directly determine the SIF induced by residual stress [98], [160]–[163] by:

$$K_{I,RS}(a) = \frac{E'}{Z(a)} \cdot \frac{d\varepsilon(a)}{da}, \quad (23)$$

where  $E'$  is equal to  $E$  in plane stress and  $E/(1 - \nu^2)$  in plane strain,  $Z(a)$  is the influence function given by specific geometry and strain gage location, and  $\varepsilon(a)$  is the measured strain.

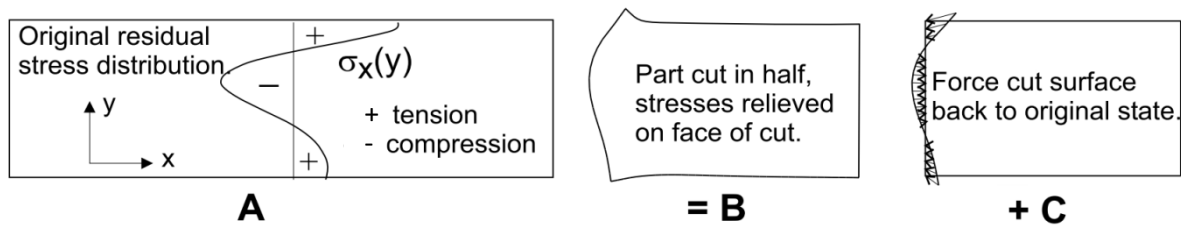


**Figure 26 Illustration of slitting measurement**

### 3.5.4 Contour Method

The contour method is one of the youngest methods. Firstly was proposed by Prime and Gonzales in a conference paper in 2000 [164] and journal publication in 2001 [165]. The contour method theory is a variation of Bueckner's superposition principle (see Figure 27). Bueckner presented the relevant theory in 1958 [166] and discussed it further in later publications [167], [168]. A similar principle was discussed by Paris in 1957 [169] and Eshelby in 1957 [170].

The component with the residual stress is cut along the section where the residual stress needs to be measured. A cutting surface is assumed to be an ideal plane, and there is an unknown residual stress distribution in the component. Due to the stress relaxation and redistribution, the contour of the cutting surface is deformed. The cutting procedure is generally processed by the electrical discharge machining (EDM, wire cut) with low processing stress. Then, the deformation profile data are collected by the high accuracy displacement sensor (mechanical or laser). The measured profile is inserted into the stress-free finite element model in the opposite direction. External stress must be applied to the interface to restore the deformed cut surface to the plane state before cutting. Then the stress distribution on the cut section is finally obtained. However, only residual stress perpendicular to the cross-section can be measured for a single cut.



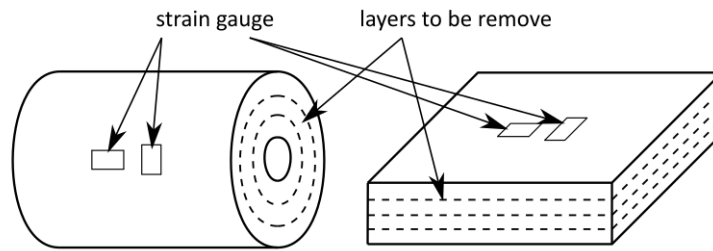
**Figure 27 Superposition principle is used to determine the original residual stress from the measurement of surface contour after cutting a part in two [164]**

The accuracy of the method has been discussed, and further development has been done. Toparli et al. [171] proposed a new criterion for determining the optimal smoothing parameters to obtain additional details. Li et al. [172] used the cubic spline interpolation processing to reduce the error effectively. Sun et al. [173] considered the cut-induced plasticity error. Olson et al. [174], [175] considered other factors such as displacement noise and surface smoothing errors. Hosseinzadeh and Bouchard [176] showed different approaches for measuring surface topography. How to perform measurement itself can be found in [177], [178].

### 3.5.5 Layer Removal Method

The layer removal method (also called the curvature method) is one of the oldest methods for the determination of residual stress [1], [179]–[181]. The layer removal method is a generalisation of Stoney's method [182]. The main principle of this method is to disrupt the static equilibrium of the residual stress, which leads to bending and deflection of the whole component. Figure 28 illustrates the layer removal method for the cylindrical and flat specimens. This deformation is measured in the form of strain or displacement. Then, removed stress is determined by the theory of elasticity. Layers are typically removed mechanically or chemically. Mechanical machining has the disadvantage of the addition of undesirable residual stress. The method is suited to a flat plate and cylindrical specimens where the residual stress varies with the depth from the surface. Stress has to be uniformly parallel to the surface. The method is suitable for different materials too [183]–[185]. When applied to the cylindrical component, the layer removal method is commonly called Sachs or Sachs boring method [186]–[189].

The described method has been used many times through the years [190]–[196] and obtained some refinements and modifications [197]–[199]. The interesting one is the modification described by Moore and Evans [198].

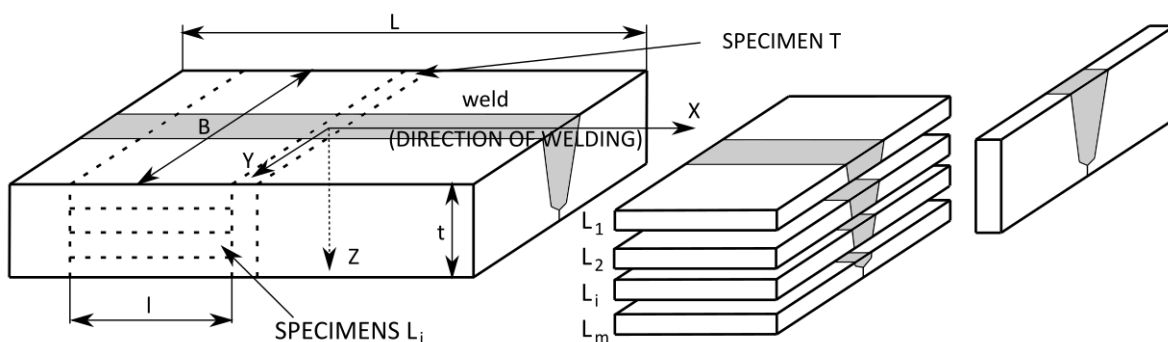


**Figure 28 Layer removal method for cylinder and flat plate**

### 3.5.6 Sectioning Method

The sectioning method [200] is one of the oldest methods for determining residual stress. In 1888, Kalakoutsky [201] reported a method of determining the longitudinal stress in bars by slitting the longitudinal strips from the bar and measuring their change in length. This method principle is that residual stress is relieved by the component cutting into many strips of the smaller cross-section [202].

In principle, the sectioning method is similar to the layer removal method. It is a relaxation method, and residual stress is determined by the deflection and/or strain measurement caused due to the disruption of the equilibrium state of residual stress in the component. The sectioning method often combines other evaluating methods to measure released residual stress, like strain gauge measurements or diffraction methods. For the original three-dimensional residual stress determination, the stress distribution acting on the newly created surfaces of the specimen before the sectioning is estimated from relaxed strains observed on the surface during sectioning. The sectioning is applied repeatedly to the sectioned pieces until no deflection and/or strain is relaxed. In this procedure, the stress in the section plane is dealt as a parameter for measurement.



**Figure 29 Welded joint of thick plate sectioned to specimens T and  $L_i$  [203]**

Through the years method has passed numerous modifications due to its different applications [202]–[205]. Ueda et al. [205] updated the three-dimensional residual stress determination method using inherent strains. However, this methodology requires strain recording while cutting out specimens from the original component. Figure 29 shows partial sectioning for the welded joint investigated by Ueda and Fukuda [203].

### 3.5.7 Diffraction methods

The diffraction methods provide non-destructive strain measurement. The diffraction methods effectively measure crystal or polycrystalline inter-planar dimensions. This dimension can be related to the magnitude and direction of the stress state existing within the material through the linear relation. These measurements are independent of whether the stress is residual or applied.

Diffraction of electromagnetic radiation occurs when the radiation interacts with atoms or crystallites arranged in a regular array. The radiation is absorbed and then reradiated with the same frequency such that strong emissions occur at certain orientations and minimal emissions at other orientations. Bragg's Law describes the angles at which the strong emissions occur:

$$n\lambda = 2d \sin \theta, \quad (24)$$

where  $n$  is an integer,  $\lambda$  is the wavelength of the electromagnetic radiation,  $d$  is the distance between the diffracting planes (inter-atomic lattice spacing, Figure 30), and  $\theta$  is the Bragg angle.

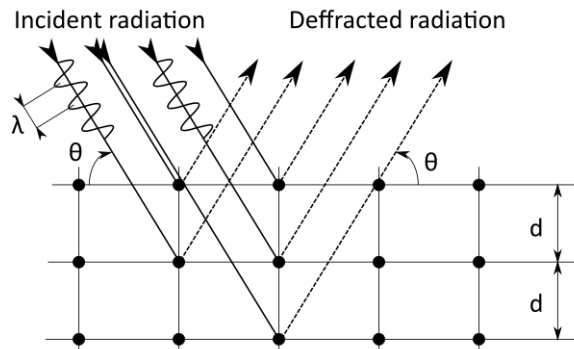


Figure 30 Diffraction ratio within the crystal structure

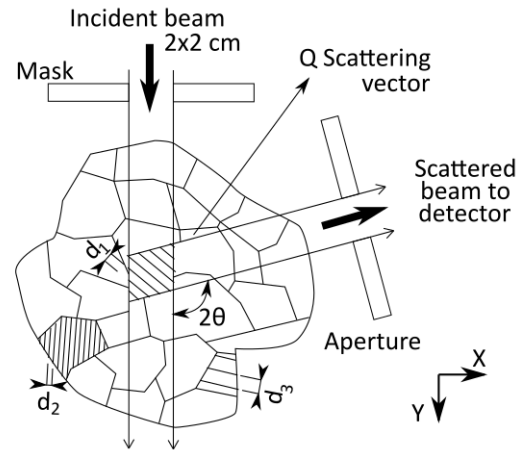


Figure 31 Principle of diffraction measurement

For the stress measurement using X-ray and neutron diffraction, a range of  $\theta$  angles are scanned, and the angle at which the most intense radiation is detected is established as the Bragg angle. Small changes in the corresponding  $d$ -spacing (Figure 31) that tend to broaden the diffracted peak reflect Type II and Type III stresses (section 3.4.4). The measured lattice strains are “absolute” quantities, that is, relative to a zero-strain state. This is a significant feature of diffraction methods because it allows the measurement of the residual stress as well as applied stress. Knowing the stress-free lattice spacing  $d_0^{hkl}$ , the lattice strain  $\varepsilon_{xx}^{hkl}$  in  $x$  direction can be calculated according to

$$\varepsilon_{xx}^{hkl} = \frac{\Delta d_{xx}^{hkl}}{d_0^{hkl}}. \quad (25)$$

To determine the stress tensor components, Hooke's law is employed [206]–[212].

### 3.5.8 Method Selection Summary

As shown in Figure 21 and based on previous sections, there were only two non-destructive techniques, the ultrasonic method and the neutron diffraction method, capable of measuring residual stress deeper than a few millimetres. However, the ultrasonic method can measure only averaged residual stress through the thickness measurement. Neutron diffraction looks like an appropriate measurement method for the crystalline material's residual stress determination. However, this kind of measurement is strictly laboratory-based. In Europe, there are only a few facilities (see Figure 32) capable of neutron diffraction measurement.

From destructive methods, two ‘new age’ methods, deep hole drilling and contour method look promising. However, primary costs and no experience with the necessary equipment for both

measurement techniques lead to choosing a more 'traditional' measurement technique. Nevertheless, EDM cutting of the whole railway axle in half to obtain a smooth cut for the contour method is unfeasible.

Therefore, there are three capable measurement techniques for further application. The Slitting method, the layer removal method, and the sectioning method combined with X-ray diffraction measurement. These three measurement techniques will be further discussed.

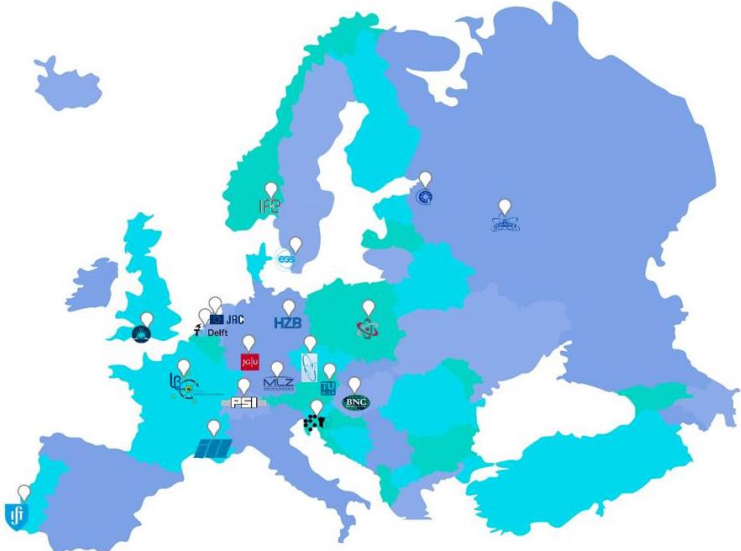


Figure 32 Map of neutron scattering facilities in Europe [213]

## 4 Aims of Thesis

The aims of the thesis can be summarised as follow:

1. *Review of literature for estimation of residual fatigue lifetime.*  
A deep review of available literature for procedures of residual fatigue lifetime estimation.
2. *Review of literature for determination of residual stress in engineering components.*  
A deep review of available literature for procedures and residual stress state determination approaches in general engineering components.
3. *Finding of methodology and procedures for determination of residual stress in sizeable components.*  
Based on the literature review, finding suitable procedures for residual stress determination in sizeable components through the whole cross-section of the component. Search for methods determining residual stresses in greater depths (tents of *mm* and more) under the surface of bodies.
4. *Creation or modification of existing methodology for determination of residual stress in sizeable components.*  
Development of suitable and reliable methodology for residual stress state determination in sizeable components. An existing experimental data valid for near-surface areas will be extended by own developed numerical procedure for greater depths. This procedure will make it possible to obtain reliable information about residual stress distribution in sizeable bodies in depths where experimental methods cannot be applied. Develop a simplified version of the proposed helpful methodology for fast engineering applications.
5. *Verification of proposed methodology for determination of residual stress on testing sample.*  
Verify the proposed methodology for the residual stress determination with other available methods using the testing sample.
6. *Implementation of residual stress influence into procedures for estimation of residual fatigue lifetime of engineering structures.*  
An implementation of residual stress influence into formerly developed procedures for residual fatigue lifetime estimation.
7. *Application of proposed methodologies of the determination of residual stress on real engineering components and estimation of residual fatigue lifetime.*  
An application of proposed methodologies onto railway axle. The railway axle residual stress determination. An estimation of the railway axle residual fatigue lifetime. Determination of an influence of residual stresses on the estimated residual fatigue lifetime of railway axle. (This task will be done in cooperation with BONATRANS GROUP a.s.)
8. *Dissemination of obtained results.*  
Publication of developed procedures, general conclusions, and selected results (with permission of BONATRANS GROUP a.s) in quality impacted journals.

## 5 Railway axle design process

Previous sections described the literature review for the fracture mechanics, state of the art for railway axle design process, and available residual stress measurement methods. The following text mainly describes the author's work and work performed in cooperation with colleagues at the IPM CAS. The railway axles investigation has been performed at the IPM CAS for many years. Presented work is made as a further step in order to improve the axle investigation process. The following sections describe a developed methodology for residual stress determination, which has been implemented in BONATRANS GROUP a.s. For methodology description purposes, one typical railway axle (see, Figure 33 (a)) will be shown for the residual stress determination. The neutron diffraction technique for residual stress determination was also applied on this axle. Therefore, it is possible to compare the results of different techniques for residual stress determination. The other axle type (see, Figure 33 (b)) will be shown for the RFL estimation and experimental validation of the estimated RFL. This axle was experimentally tested in full-scale tests and compared with numerically simulated lifetimes.

Railway axles (see Figure 33) investigated in this work are manufactured by the BONATRANS GROUP a.s. The axle material is the EA4T steel grade (25CrMo4; see Table 1 for chemical composition, Table 2 for mechanical properties, and Figure 34 for the microstructure). Both investigated axles were forged, machined, and then surface treated (e.g., quenching or induction hardening), followed by final turning to precise dimensions.

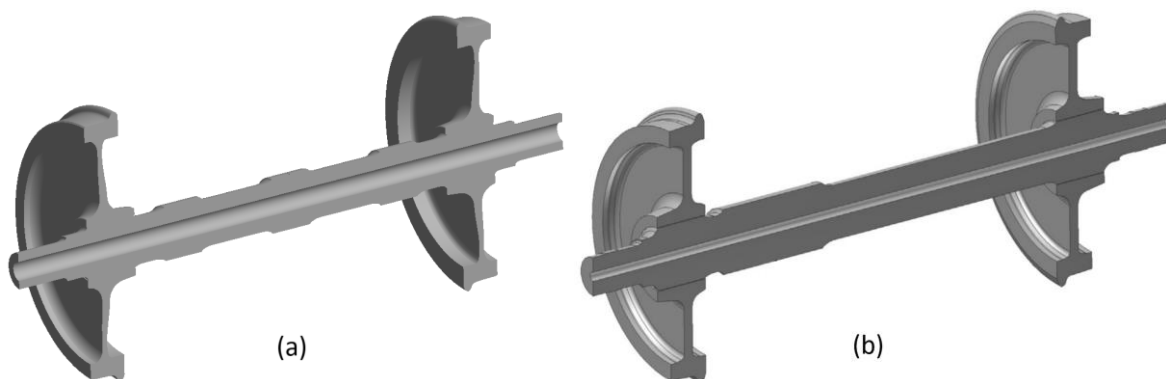


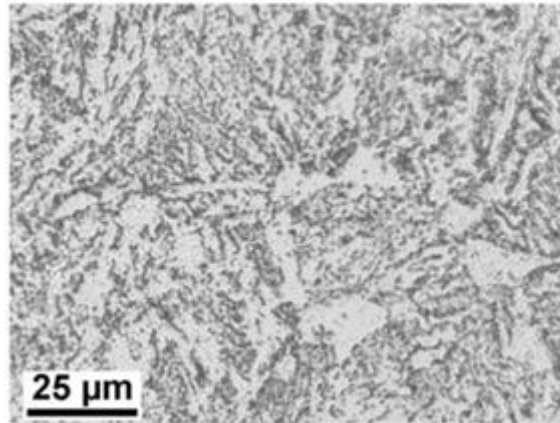
Figure 33 Considered railway axles

Table 1 Chemical composition of the EA4T steel [214]

Component	C	Si	Mn	P	S	Cr	Cu	Mo	Ni	V
Min (%)	0.220	0.150	0.500	0.000	0.000	0.900	0.000	0.000	0.000	0.000
Max (%)	0.290	0.400	0.800	0.020	0.015	1.200	0.300	0.300	0.300	0.060

Table 2 Mechanical properties of the EA4T steel [215]–[218]

Mechanical property	Mark	Value	Units
Young's modulus	$E$	204.0	GPa
Poisson's ratio	$\nu$	0.3	-
Yield Stress	$\sigma_y$	609.0	MPa
Ultimate tensile stress	$\sigma_u$	727.0	MPa
Cyclic yield stress	$\sigma_{y,c}$	420.0	MPa
Flow stress	$\sigma_0$	668.0	MPa
Strain at failure	$A_5$	22.5	%



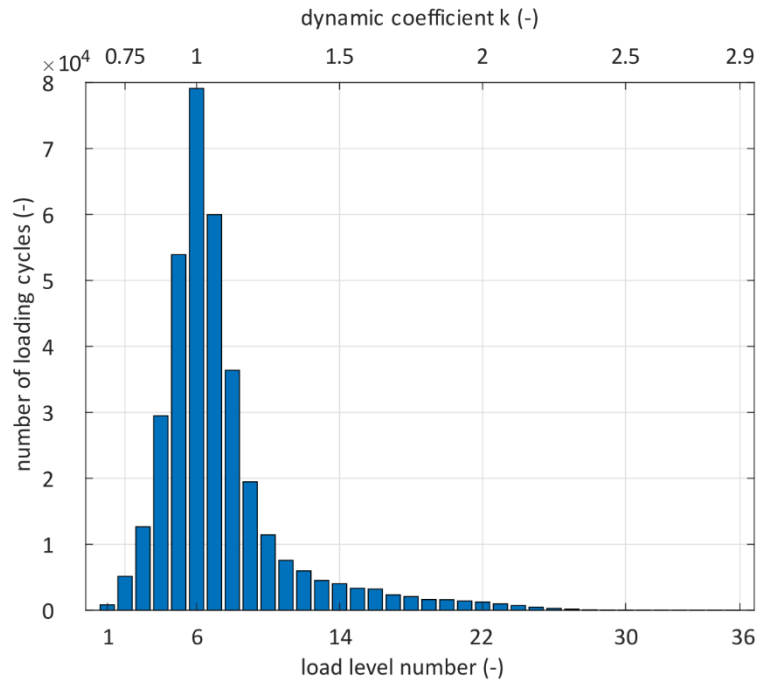
**Figure 34 Typical bainitic microstructure of the EA4T steel of conventionally treated axle [216]**

Knowledge of the loading conditions for the railway axle seems to be simple to specify. Standards define three types of variable loadings (weight, braking, and traction load) and one static load (press-fit) acting on the axle. However, in reality, the railway axle is exposed to another significant static loading – residual stress.

Numerical simulations can determine the bending and press-fit stress fields. However, the residual stress field determination only by numerical simulations (simulation of the induction hardening process for the whole railway axle) requires comprehensive material data knowledge as well as the verification and validation process where the experimental work is inevitable. Therefore, a procedure that combines the experimental residual stress measurement and the numerical simulation for the residual stress field evaluation was developed.

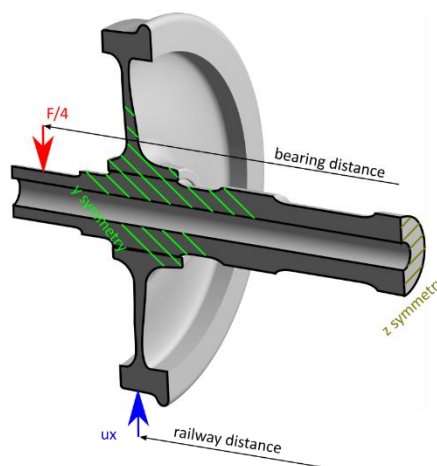
### 5.1 Bending and Press-fit Stress Field Determination

As was mentioned in the previous 2.3 section, estimation of the critical position of the component is necessary for a damage-tolerant approach. The critical position is mainly influenced by the variable bending load stress concentrators. Critical position can be affected by additional load due to press-fit [59]. The bending load varies during the train operation. The load amplitudes are obtained experimentally during the train operation at the different railroads [219]–[221]. Load amplitudes are then sorted by the Rainflow method into the different load levels, see Figure 35. Representatives of BONATRANS GROUP a.s provided the load spectrum used in this work. Spectrum was sorted into the 36 load block levels. The most common load amplitude is set as the static load (load caused by the train's weight), and other amplitudes are then considered as the multiplication of the “static load”. For the multiplication of the static load, dynamic coefficient  $k$  is used. The highest load level is  $k = 2.88$  in the provided spectrum. For the fatigue crack growth in the early stages (1 or 2 mm), the highest load levels are mainly responsible. Therefore, the critical position is estimated according to the highest load block and press-fit loading conditions by the numerical simulations.



**Figure 35 Histogram of used spectrum, sorted into 36 loading levels, which represents 1000 km of service operation**

The numerical model of the railway wheelset consists of 293000 hexahedral quadratic elements. The material model of the railway wheelset was linear elastic isotropic, defined by Young’s modulus of 204 GPa and Poisson’s ratio of 0.3. Figure 36 shows boundary conditions used in numerical simulations. The advantage of two symmetry planes was used. One symmetry plane was defined in the middle of the wheelset in a longitudinal way, and the second symmetry plane was defined in the middle in a transversal way. The vertical degree of freedom was restricted in the node where the wheel-rail contact should occur. Force loading was applied near the free end of the axle, where bearings are mounted. The nonlinear frictional contact with the friction coefficient of 0.6 (based on previous studies performed by Náhlík et al. [222]) was defined between the axle and the wheel. A geometric overlap of 0.3 mm was used as the press-fit loading condition.



**Figure 36 Boundary conditions of the used model for the critical position determination**

Results are shown in Figure 37, where axial stress is plotted near the critical position at the T-notch stress concentrator. One can see that the highest axial stress is 29.3 mm far from the wheel seat corner. This position is used as a critical position in further investigation.

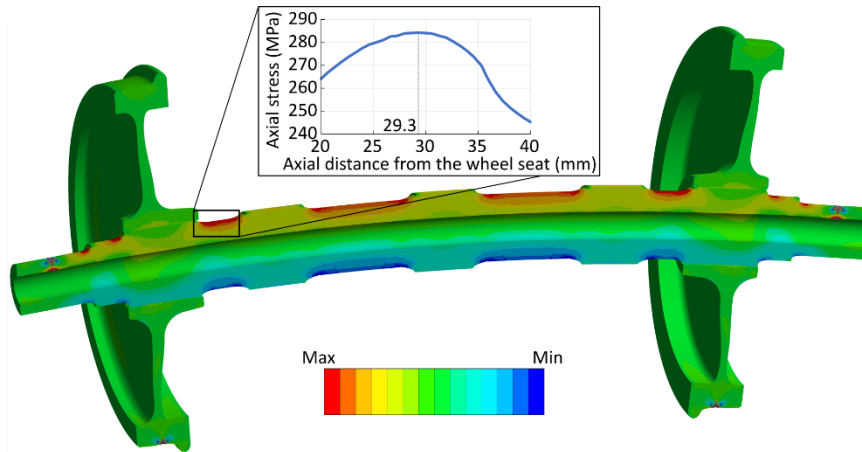


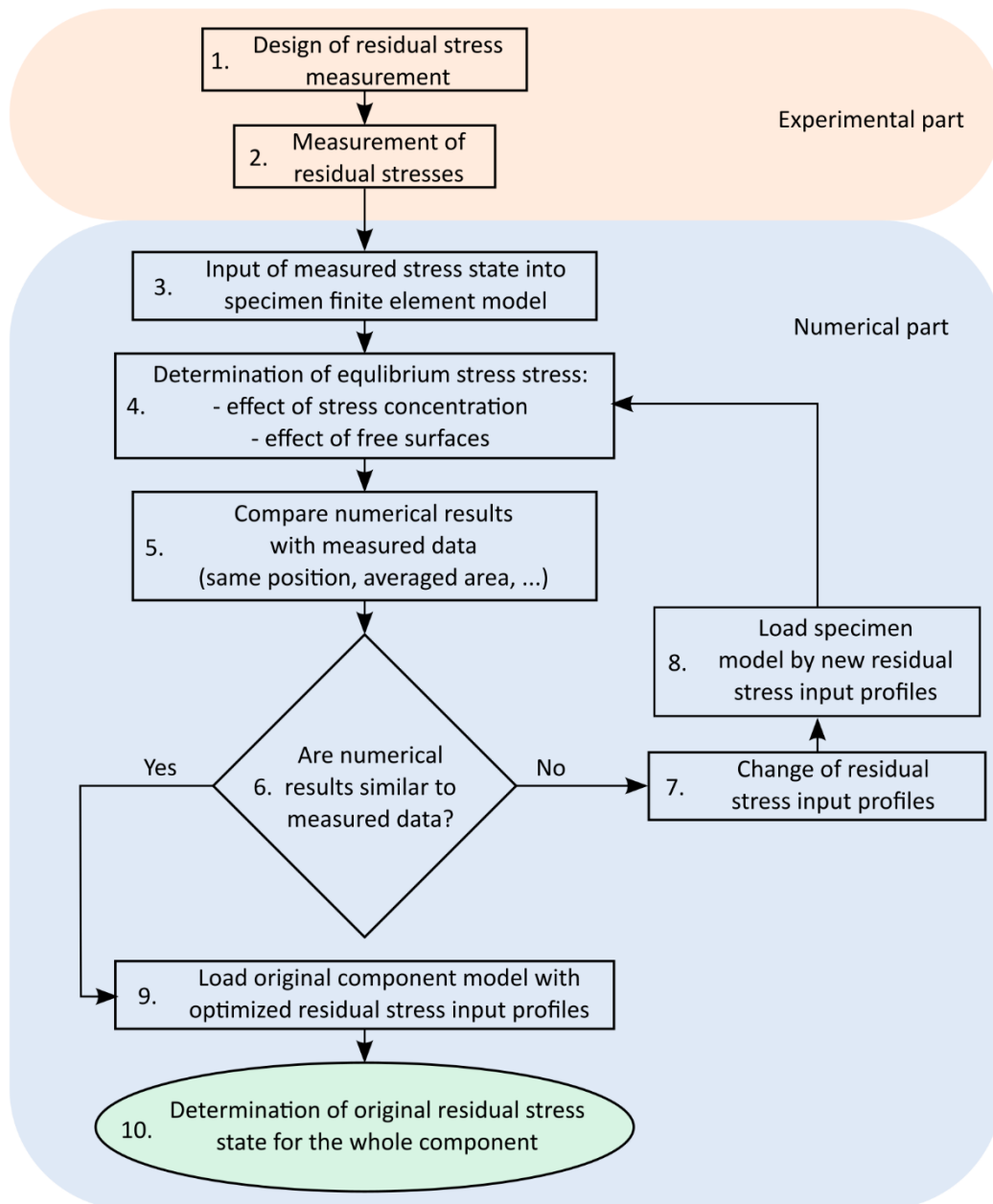
Figure 37 Axial stress behaviour near the critical position at the axle

## 5.2 Residual Stress Field Determination

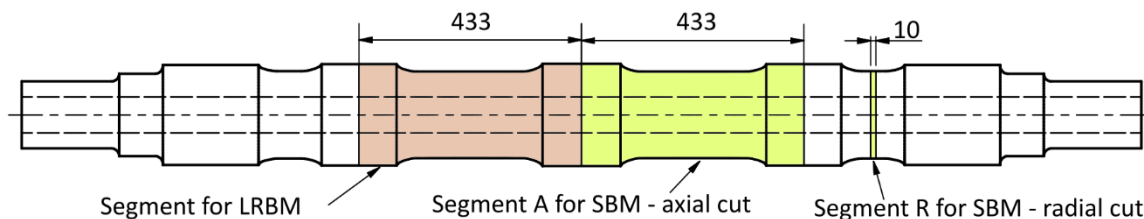
The literature review showed that residual stress determination in large depths of the sizable component like railway axle is challenging. Therefore, a new affordable methodology has been developed. Figure 38 shows the scheme of this methodology which combines the experimental residual stress measurement at the surface with the numerical simulations. First, the functionality of this methodology is verified by the application in a known manner. The layer removal method described by Moore and Evans [198] is used. Results from the layer removal method will be evaluated by the known formula as well as by the numerical simulations. Then new, less time-consuming method will be described.

For the residual stress determination explanation, the railway axle with the total length of the investigated railway axle was 2180 mm. The outer diameter in the investigated area was 168 mm. The hole inside the axle had a diameter of 70 mm (see Figure 39).

Two methods for residual stress determination were applied on one railway axle: the **layer-removal-based method** (LRBM) and the **sectioning-based method** (SBM). Both follow the same general methodology, schematically illustrated by a diagram in Figure 38. The first step is the design of the method, followed by destructive specimen preparation and X-ray diffraction measurement of residual stress on the surface of the specimen. An integral part of both methods is also a numerical simulation of the experiments by FEM that corrects the measured values and thus provides the true, original residual stress distribution in the component before any machining. The principles and details of the methods are described in the following sections.



**Figure 38 Scheme of the developed optimization process of residual stresses determination in sizeable components**

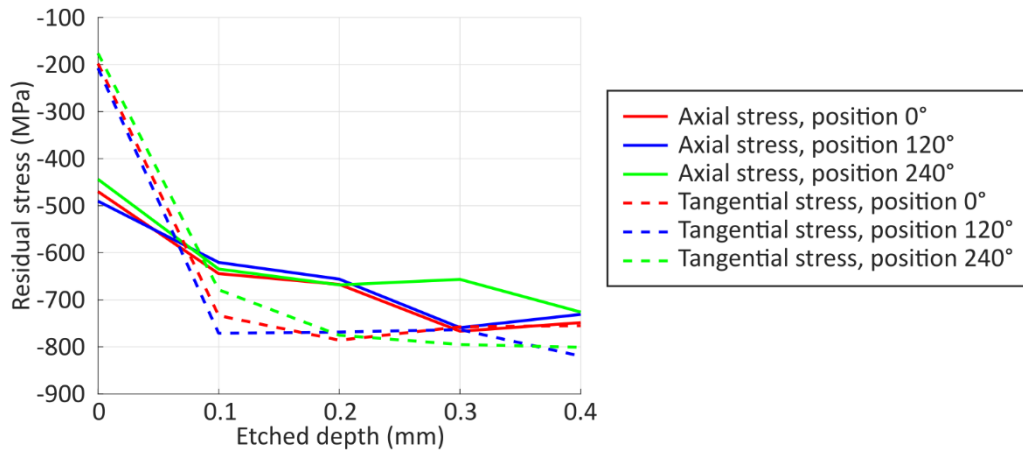


**Figure 39 Scheme of considered railway axle with highlighted segments for residual stress measurements**

## 6 Developed Methodology for Residual Stress Determination

The X-ray diffraction (XRD) itself was not listed among the methods suitable for residual stress determination in large depths. However, despite its low penetration depth, it can be used for the railway axle when combined with appropriate specimen preparation and, more importantly, the essential numerical procedure for analyzing and correcting the measured data see Figure 38.

XRD was used to measure residual stress at the surface of the railway axle when performing both the LRBM and the SBM –the step 2 in Figure 38. The setting of the method follows. The Stresstech Xstress 3000 robot with Chromium (Cr) radiation, current of 9 mA, and voltage of 30 kV was used for X-ray diffraction. The X-Ray beam was collimated to a diameter of 2 mm. The measurements were carried out using a 30° detector with four inclinations between  $\pm 40^\circ$ . Diffraction peak from {211} planes at  $2\theta = 156.4^\circ$  was used for the measurements. Young's modulus  $E = 204$  GPa and Poisson ratio  $\nu = 0.3$  were used for stress calculation. Surfaces were cleaned and electrolytically etched by KRISTALL 650 machine before every measurement to remove residual stress introduced by machining.



**Figure 40 Measured residual stress versus the etched depth for different circumferential positions determined on the original outer surface**

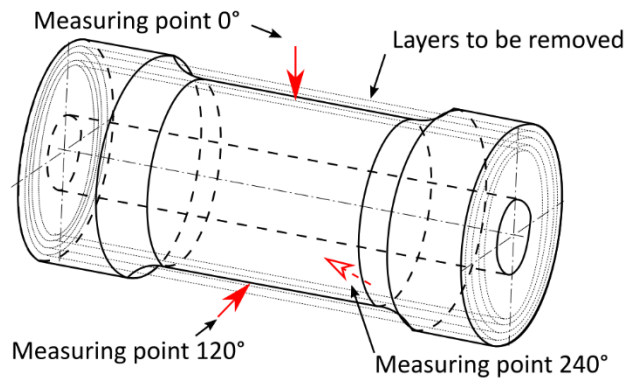
Prior to the actual measurement of stress by XRD, the surface has to be prepared by etching. It is desirable to etch such an amount of material to get rid of subsurface residual stress caused by machining. Different etching depths were tested on the studied axle. In Figure 40, residual stress values obtained by XRD for different etched depths are plotted. Machining still influences the residual stress results after etching 0.1 mm of the material. With 0.2 mm of the etched depth, there is still some observable influence in the axial residual stress values. For depths of 0.3 and 0.4 mm, most of the results fall within the uncertainty range of the method. Therefore, the etching depth was set to 0.3 mm for all the measurements.

As shown in Figure 40, the residual stress components determined at the three predefined positions around the segment circumference are almost the same. Such regular distribution of residual stress around the railway axle segment was found for all the etched depths. Therefore, axisymmetric residual stress distribution can be assumed, so using the average of the three measured values as the residual stress magnitude for a given depth can be used.

## 6.1 The Layer-Removal-Based Method

The LRBM consists of two main parts, as outlined in Figure 38. The first part is the actual experiment (corresponding to the first two steps in Figure 38) that involves the design of the experimental setting (dimensions of specimens, number of layers, etc.) and measurements by XRD. The second part (corresponding to steps 3 to 10 in Figure 38) is a set of numerical simulations that finally lead to the corrected residual stress distribution in the whole railway axle.

The specimen for the LRBM is a full segment of the axle (see Figure 39 and detail in Figure 41). The specimen dimensions were chosen, bearing in mind that the manipulation with the whole axle is complicated. Therefore, the influence of the free surface on the stress state was studied to avoid the necessity to use the whole axle for experiments. It was then decided that a symmetrical 433 mm long part (shown in Figure 39) is compact enough. At the same time, the investigated cross-section in the middle of such a segment stays free from the effects of the free surfaces, according to Saint-Venant's principle [223]. The residual stress state is preserved in its original form in the whole axle.



**Figure 41 The measuring points' position for the LRBM**

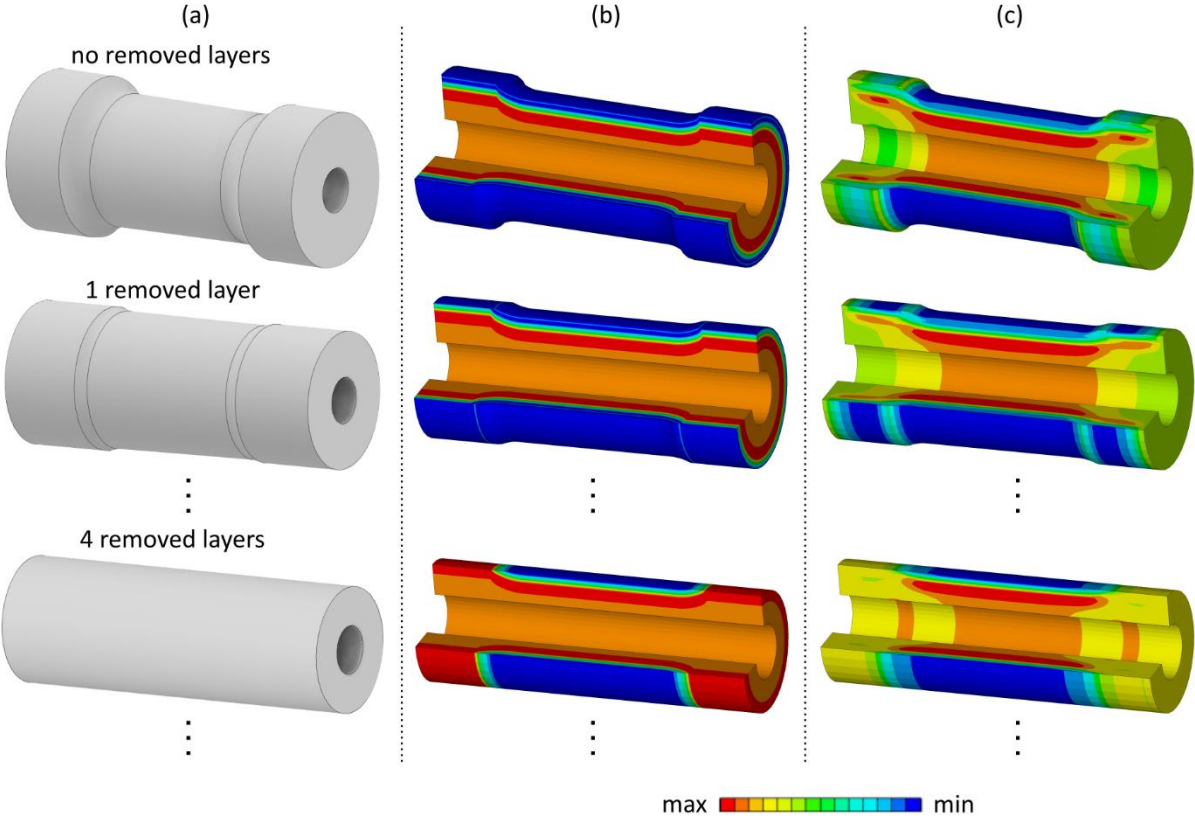
The number of layers for subsequent machining (lathe turning) away was designed to be 17 (the layers did not have uniform thickness). The first residual stress measurement was carried out on the original surface of the axle before cutting the 433 mm long segment out. Then, another measurement was performed on the original surface after the specimen was cut out of the axle. These measurements would reveal the potential influence of free surfaces of segment cut from the axle. After that, three measurements for three removed layers with the thickness of 5 mm were performed (to remove the remaining pairs of wheel seats), followed by 11 measurements and 11 removed layers with the step of 2 mm and the last four measurements and four removed layers were carried out with the step of 5 mm.

The measurements were always carried out at the same spots spaced by 120° on the circumference in the middle of the segment, see Figure 41. The total number of measurements was  $20 \times 3 = 60$ . XRD was employed for all the measurements. Axial and tangential stress components were recorded in each of the three spots on the surface.

Note that measured residual stress values cannot be considered as the original residual stress state in the axle due to removed layers of material with residual stress. Therefore, there is a redistribution of residual stress in the machined segment. Hence, after the measurements, the residual stress values must be corrected. For this, Moore and Evans provided an analytical solution based on the theory of elasticity. In this work, numerical simulations and own analytical procedure were used instead.

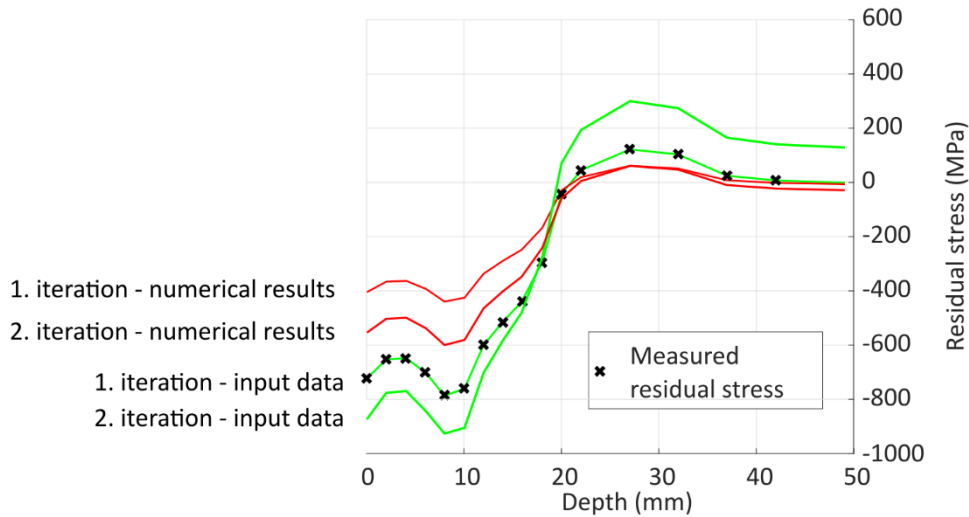
Finite element models of the specimens used in the experiments are created. The discretization was made very fine to be able to describe the residual stress gradient. The biggest model contained about 21 000 quadratic, quadrilateral 2D elements. The material model of the segments was linear elastic isotropic, defined by Young's modulus of 204 GPa and Poisson's ratio of 0.3. The model's initial state was defined using the INISTATE function available in the ANSYS [224].

A 2D axisymmetric representation (see examples of the geometry in Figure 42 (a)) for each measured geometry was created (one measured depth point corresponds to one FEM model). In the next step, the same input residual stress was defined in the model – this state is illustrated in Figure 42 (b). Note that the distribution is defined always starting at the original outer surface of the axle and removing a layer thus means, removing the corresponding part of the stress distribution. After solving the models, the residual stress (which initially is not in equilibrium) redistributes, resulting in the equilibrium distribution in Figure 42 (c). These values are then compared to the measured values on corresponding surfaces. The input stress is then changed based on the obtained difference. The input data are changed and again used as the initial state in the next round of calculations.



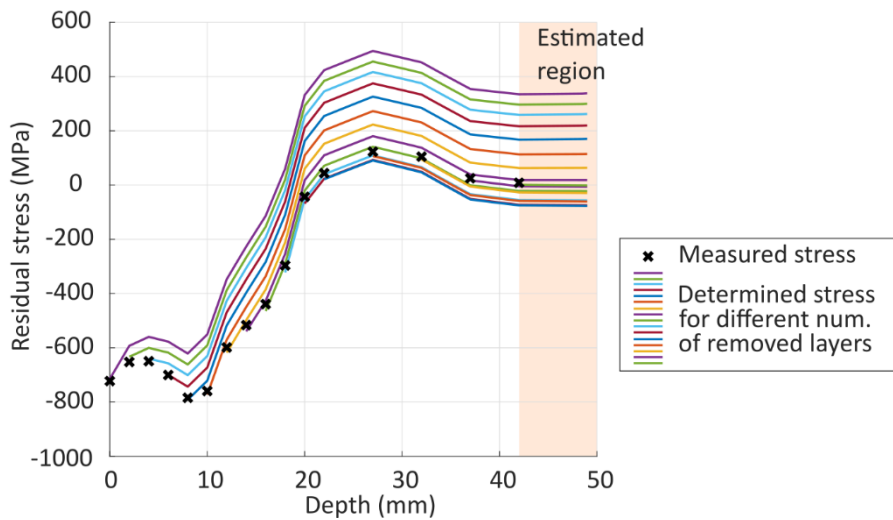
**Figure 42 Illustration of LRBM (a) segment models; (b) defined initial stress state; (c) redistributed equilibrium stress state**

Figure 43 shows the evolution of input residual stress (green lines) for the measured data (black crosses). The goal is to find such input stress (green line) that, after redistributing and achieving equilibrium, the resultant stress (red line) corresponds to the measured data. Residual stresses in the last two measured depths are close to zero. There is a small region between the depths of 42 mm to 49 mm marked as “estimated” in Figure 44, where the residual stress values are estimated by extrapolation of a constant value.



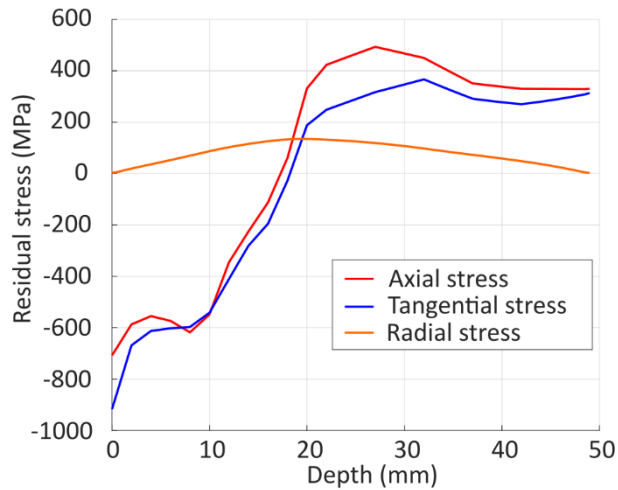
**Figure 43 Schematic evolution of first two iterations of initial state input data for measured axial residual stress**

After several iterations, compliance between numerically and experimentally determined residual stress values was found. Figure 44 shows the measured data points (black crosses) compared to the axial residual stress equilibrium state in each FEM model of the corresponding segment. It can be seen that the measured residual stress obtained on the surface of each segment corresponds to the simulation result at the surface, while the same initial stress state data were used for each of the models – that means this initial stress distribution can be taken for the original stress state in the specimen.



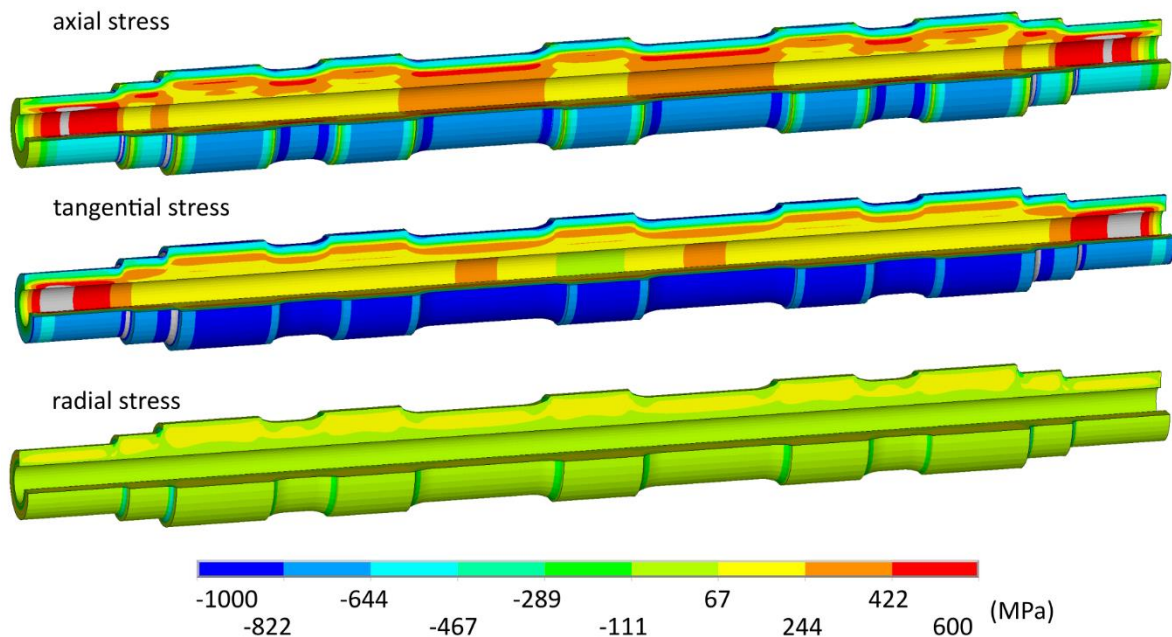
**Figure 44 Optimized solution for simulated segments**

Figure 45 shows the results of axial, tangential, and radial residual stress components. These data correspond to real residual stress distribution in the axle. In the following, they were used as input values for a numerical model of the whole axle.



**Figure 45 Results of residual stresses determined by LRBM**

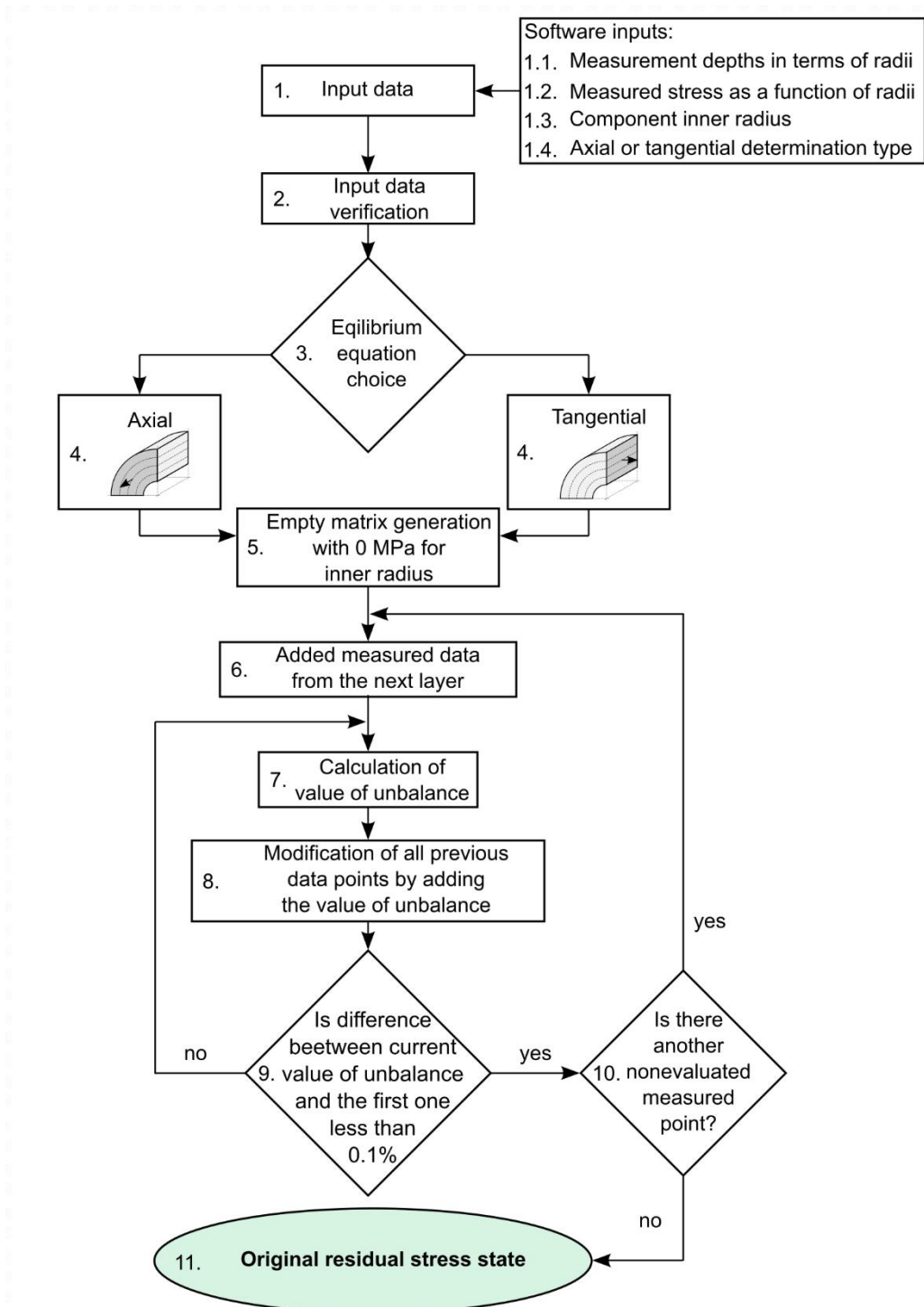
The residual stress state in the whole axle can be estimated after loading the model of the whole axle by the residual stress distribution obtained in the previous FEM analysis. It is important to note here that the residual stress in the whole axle corresponds to the measured values in the parts that were cut out and measured. However, the residual stress distribution differs in other parts of the axle (e.g., the ends or the rounded transitions) because it assumes the most suitable equilibrium there. Figure 46 shows the resultant distribution of residual stress in the whole axle.



**Figure 46 Final residual stress distribution in the whole axle**

### 6.1.1 Analytical Iterative Evaluation of the Original Residual Stress State

After the successful numerical determination of the original residual stress state, another procedure was developed. This quasi-analytical iterative procedure developed in the MATLAB software uses the force equilibrium conditions and the iterative procedure. Evaluation in MATLAB is faster than the numerical evaluation. However, it is applicable only for cylindrical specimens.



**Figure 47 Scheme of the iterative evaluation method for the correction of residual stress values measured by X-ray diffraction**

After the experiment, a set of residual stress values (axial and tangential) were measured in certain positions in the axle segment (defined by radius  $r$ ). The correction procedure is described at the showcase with three removed layers in order to show the principle and keep the text and figures clear. Experimental data are then evaluated at the end of this section.

The iterative procedure is based on repeatedly calculated values of an unbalance  $U$  and searching for such values of residual stress  $\sigma$  that will produce the value of  $U$  close to 0 for the whole specimen.

Therefore, we are looking for the inner equilibrium state of the body. The measured values are used as starting points for the iterative process. The unbalance is calculated as

$$U = \frac{\sum_{i=1}^n F_{dir,i}}{S_{dir,tot}} = \frac{\sum_{i=1}^n S_{dir,i} \sigma_{dir,i}}{S_{dir,tot}}, \quad (26)$$

where  $F$  is reaction force,  $S$  is corresponding area,  $\sigma$  is stress,  $n$  is a number of measured depth points + 1, the  $dir$  subscript corresponds to the evaluated direction ( $dir = ax$  for axial and  $dir = tg$  for tangential), and the  $i$  subscript corresponds to the radius of the evaluated surface ( $i = r_{in}$  corresponds to the inner surface,  $r_{ou}$  is the outer surface radius and  $r_1$  to  $r_n$  are the radii in between).

Two assumptions are made at the beginning of the determination process:

1. A theoretical value of 0 MPa is added to the measured values for the inner radius, assuming that after removing all material (which is physically impossible), 0 MPa, would be measured. This value is added to estimate residual stress in the region, followed by the final physically possible measurement. If there is no hole in the cylinder (solid cylinder), 0 MPa value corresponds to radius  $r_{in} = 0$  mm.
2. The linear residual stress distribution is assumed between each measured point.

The whole procedure was programmed as a MATLAB function. Figure 47 shows the scheme of the procedure.

The determination process itself runs in two nested cycles. The outer cycle determines the portion of layers for the inner cycle to work on, starting from the innermost layer and adding one layer in each step. The inner cycle evaluates the force equilibrium condition for the current portion of layers. It is important to note that the layers must correspond precisely to the removed layers when performing the measurements.

Figure 48 illustrates the evaluation process. The blue points in the figure stand for the measured values. The black X point is the additional theoretical value of 0 MPa. The iterations run as follows:

### 1<sup>st</sup> iteration

The determination starts from the innermost layer (the interval from  $r_{in}$  to  $r_3$ ), in which the 0 MPa bounds at  $r_{in}$  and the last measured point at  $r_3$ . Then, the inner circle works on this interval only. It calculates the value of unbalance  $U$ , and then shifts the values of stress by the calculated unbalance and calculates the unbalance again until it reaches the point when the  $U < 0.1\%$  (chosen calculation error) of the first unbalance (this condition is referred to as the *equilibrium condition* in further text). However, the measured value at  $r_3$  cannot be changed at this point. It is regarded as the boundary condition. The only value that can be shifted is the value of 0 MPa. The equilibrium equation for the first iteration in the case of axial residual stress evaluation is:

$$U = \frac{\sum_{i=1}^{n=2} F_{dir,i}}{S_{dir,tot}} = \frac{\pi \left( r_3^2 - \left( r_{in} + \frac{r_3 - r_{in}}{2} \right)^2 \right) \sigma_{ax,r_3} + \pi \left( \left( r_{in} + \frac{r_3 - r_{in}}{2} \right)^2 - r_{in}^2 \right) \sigma_{ax,r_{in}}}{\pi (r_3^2 - r_{in}^2)} \quad (27)$$

where  $r_3$  is the radius of the last measured point and  $r_{in}$  is zero for the solid cylinder and inner radius for the hollow cylinder.

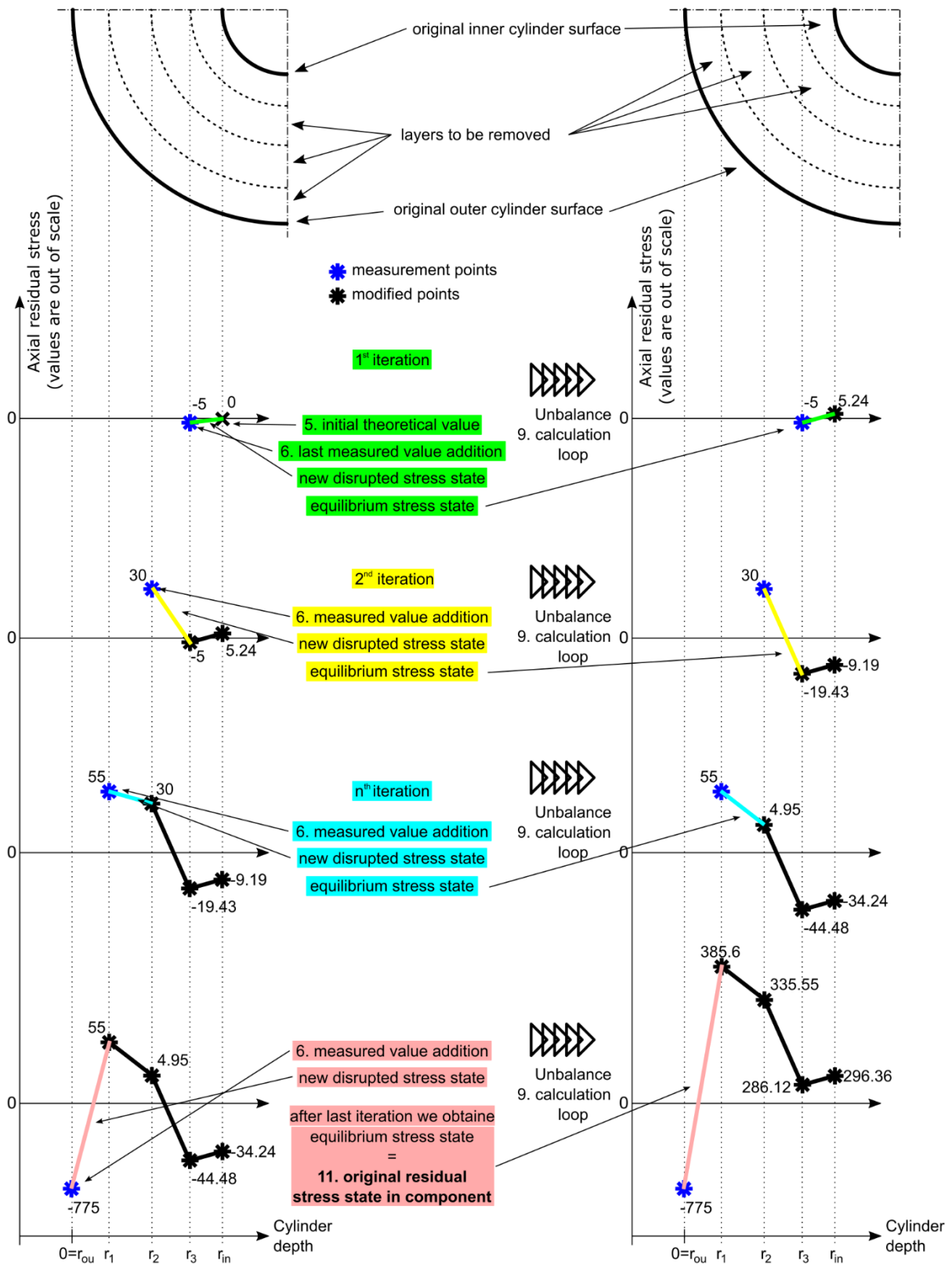


Figure 48 Schematic illustration of the analytical residual stress determination process

To consider the linear stress distribution between the measured points, the area corresponding to the evaluated point must be equal to half of the current layer thickness. Figure 49 shows corresponding areas for the schematic case shown in Figure 48.

The next iteration starts when the equilibrium condition is fulfilled.

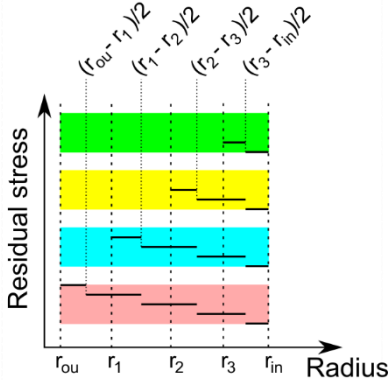


Figure 49 Corresponding area functions behaviour

**2<sup>nd</sup> iteration**

The next layer is added to the innermost layer to form the next interval for the equilibrium search. In the 2<sup>nd</sup> iteration, the interval is from  $r_{in}$  to  $r_2$ . Now, the measured value at  $r_2$  is the boundary condition that cannot be changed. The previous values at  $r_3$  and  $r_{in}$  must be changed now to find the equilibrium state. This is done again by shifting the values by the newly calculated value of unbalance until the equilibrium condition is met ( $U < 0.1\%$  of the first calculated unbalance).

**n<sup>th</sup> iteration**

In every following iteration, the process of adding the next layer and searching for the equilibrium by shifting the previously calculated values is repeated until every measured depth is used and the final equilibrium state is obtained.

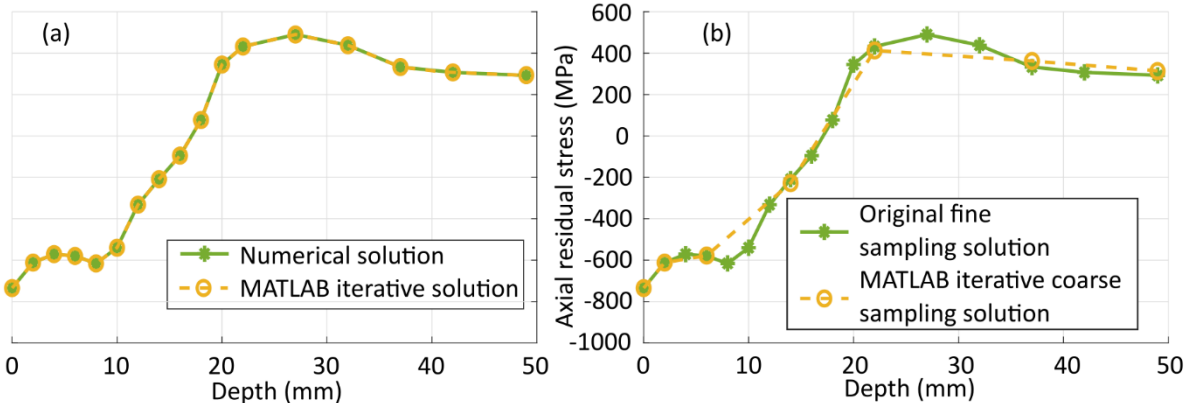


Figure 50 Comparison of axial residual stress evaluated by numerical simulations and developed solution in MATLAB from the same measured data with (a) fine depth sampling and (b) coarse depth sampling

Figure 50 shows that previously proposed numerical and MATLAB iterative evaluations give the same results for the original residual stress state even though fewer measured points are used for the determination.

Residual stress determination by the LRBM shows axisymmetrical stress distribution for the induction hardened railway axle. The results further revealed a gradient through the axle cross-section. High compressive (negative) stress near the outer surface occurs for axial and tangential stress components. Then, both components increase up to 26 and 33 mm depth for axial and tangential components, respectively. After reaching the maximum value, both components slightly decrease and keep constant value through the rest of the axle cross-section. Developed numerical and analytical solutions show the same results. The advantage of LRBM lies in using one measuring segment and the possibility of measuring non-uniformly distributed residual stress around the axis. The main disadvantage of the method is repeated manufacturing which is time-consuming.

### 6.2 The Sectioning-Based Method

The SBM is basically a new method designed to need just two sections from the railway axle. On those, residual stress is measured by the XRD without further machining.

The SBM requires two different specimens manufactured from the studied railway axle (see Figure 39 and detail in Figure 51). One for the axial stress measurement (segment A; an example of the segment A like specimen is shown in Figure 52) and the other for the radial and tangential stress measurements (segment R). The segment A is an exact half of an axle segment cut along the longitudinal axis. The length of the segment is 433 mm, the same as for LRBM. The segment R is a 10 mm thick ring – a lower thickness was chosen to ensure axial residual stress is relaxed and keep the tangential and radial residual stress in the ring.

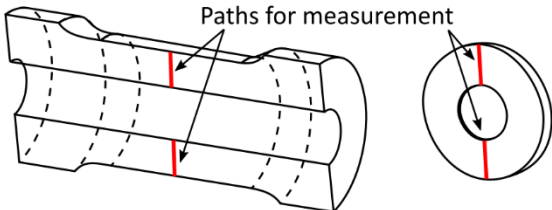


Figure 51 Measuring paths positions for segment A and segment R for SBM

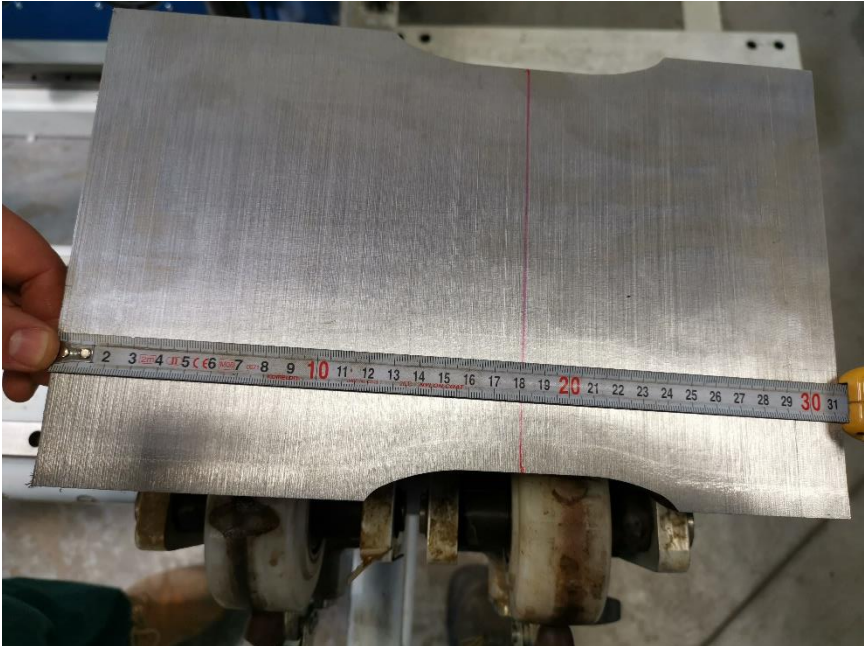
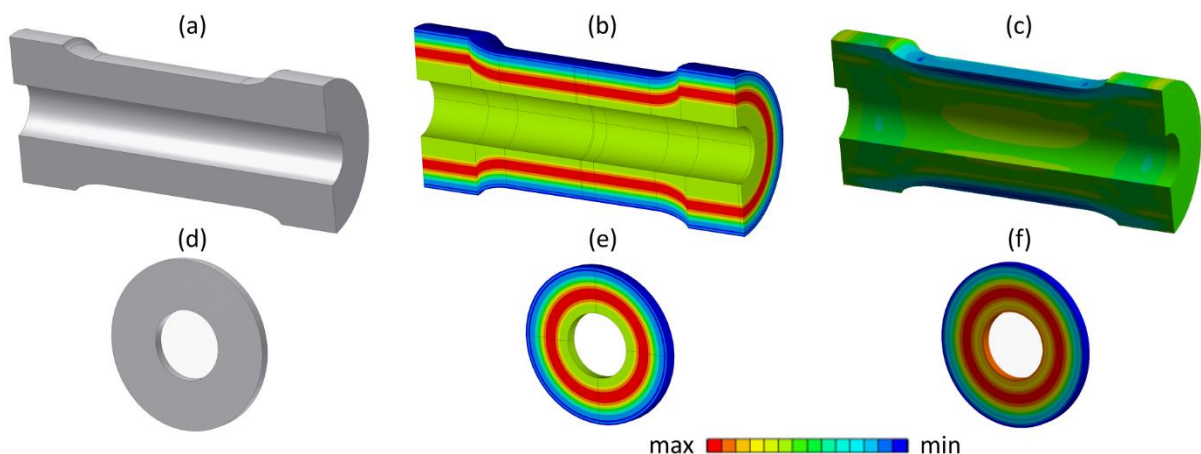


Figure 52 Example of the experimental segment A like specimen manufactured from a different axle

As shown in Figure 51, the measurement location was considered a path connecting the outer surface with the inner surface for both segments. The path in segment A was located precisely in the middle of the segment. The number of measured points was set to 21. The spacing of the points is the following: from the outer diameter to the depth of 6 mm by the step of 1 mm; from 6 mm to the depth of 26 mm by the step of 2 mm, and from 26 to 46 mm (inner surface) by step of 5 mm. Preparation of the surface before measurement and residual stress measurement as described in section 5.2 followed.

One residual stress measurement of the original axle surface was also performed before cutting the segments A and R out of the axle for later verification of the surface values. Due to the probe dimensions, the residual stress near the original outer and inner diameter (close to the edges of the specimens) cannot be reliably measured by the given method. Therefore, the first point I measured at a depth of 2 mm under the outer surface and the last 2 mm before reaching the inner surface. Missing input data from the original outer and inner surfaces were estimated by constant extrapolation of the closest available value.

Like in the case of the LRBM, the measured values must be corrected to obtain the original residual stress distribution. In the case of the SBM, a numerical simulation is the only possible choice for the calculation because no analytical solution is possible for the specimen shapes. Therefore, the numerical procedure for determining the original residual stress field was performed. The procedure was similar to the case of LRBM – repeated cycles of initial state definition, followed by equilibrium state determination and comparison to measured stress values. Instead of simulating 16 different specimens, just the two segments, A and R, were modelled. In this case, 3D models of the specimens were used because segment A is not axisymmetrical and, therefore, not suitable for 2D modelling. Segments A and R discretization were done by 57000 and 2300 quadratic, hexahedral 3D elements, respectively. The material model of the segments was linear elastic isotropic, defined by Young's modulus of 204 GPa and Poisson's ratio of 0.3 as well as for LRBM.



**Figure 53** Illustration of SBM (a), (b), (c) segment A - axial cut; (d), (e), (f) segment R - radial cut; (a), (d) models for measurement; (b), (e) distribution of input stress; (c), (f) redistributed stress after numerical calculation

Figure 53 (a) and (d) show the model's geometry. The initial state of the models before solving for the equilibrium is shown in Figure 53 (b) and (e). Figure 53 (c) and (f) then demonstrate the same model after achieving equilibrium. This state corresponded to the state of the actual specimens when the XRD measured residual stress. As soon as the measured state and the determined

equilibrium agree with a sufficiently slight deviation, the initial state of stress that caused this equilibrium is used for the full-scale axle where the original residual stress is obtained.

The measured data (points) correlation with the calculated equilibrium for segments A and R (solid lines) is plotted in Figure 54 and Figure 55, respectively.

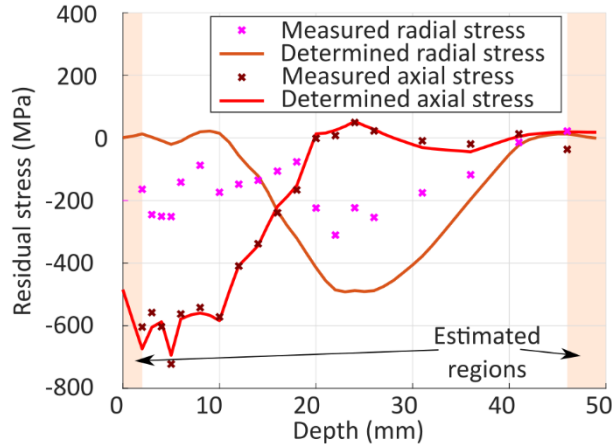


Figure 54 Optimized stress components for segment A (axial cut)

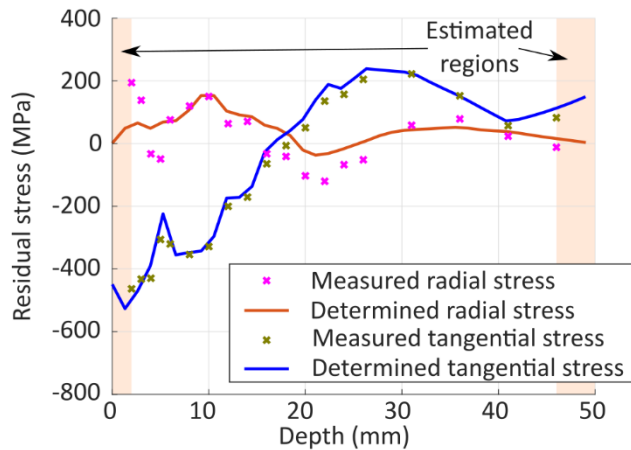


Figure 55 Optimized stress components for segment R (radial cut)

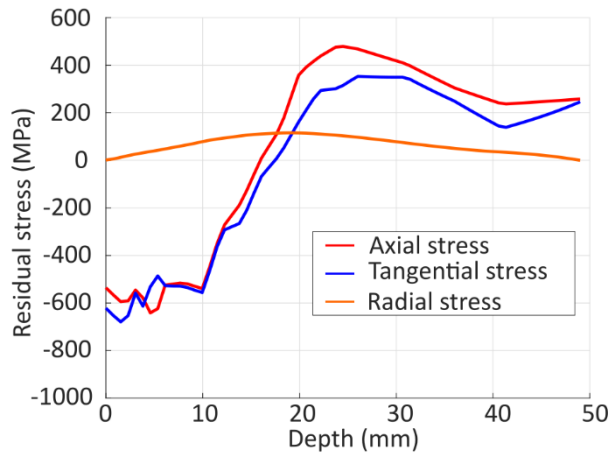


Figure 56 Results of residual stress measurement by SBM

LRBM results show small values of radial stress in comparison with axial and tangential stress. Therefore, radial stress was neglected for the other optimization process, and presented results of radial stress are obtained as a side effect of the equilibrium stress state.

Figure 56 shows the already corrected, original axial, tangential, and radial residual stress distributions determined by the SBM.

The main advantages of the SBM are that it requires fewer measurements than the LRBM and much less time, as no additional manufacturing of the measured segments is needed between the measurements. The disadvantage is that the information of residual stress distribution is determined just in one or two paths (180° rotated to each other) across the cross-section. Therefore, SBM accuracy can be lower than in the LRBM case, where every stress value is determined as the three values average on the circumference.

### 6.3 Discussion and Validation

Two different methods for determining residual stress through the cross-section of railway axles were performed that combine well-established experimental procedures with numerical simulations. Experimental specimens for both methods were manufactured from the same axle.

The axial residual stress distributions obtained from both methods are plotted in Figure 57. There is good agreement between these two methods. The most important residual stress component is the axial component. The most dangerous cracks grow in the radial direction with tensile (positive) axial stress acting as the opening force (the compressive residual stress acts against the opening, thus preventing cracks from growing). For investigated commercially manufactured axle with induction hardening treatment, the compressive (negative) axial residual stress of about -600 MPa was found up to the depth of 8 mm below the axle surface. Then, the axial residual stress rises in the interval from 10 mm to 24 – 27 mm, where it reaches its maximum of 490 MPa. It is essential to note here that the effort to induce a high compressive residual stress close to the surface of the axle also induces high positive stress deeper in the cross-section.

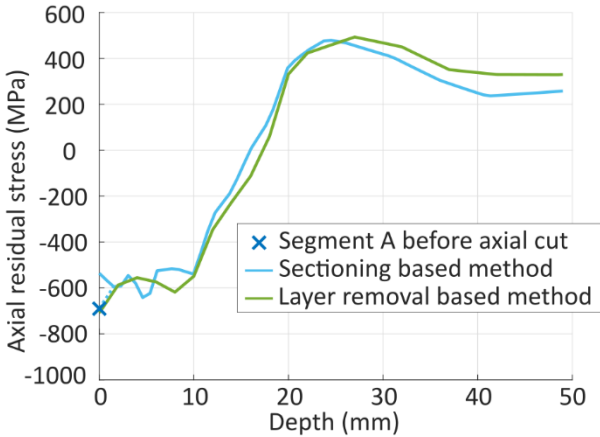


Figure 57 Comparison of axial residual stress measured by different methods

The distributions of the other two components of stress, tangential and radial, are shown in Figure 45 and Figure 56 for LRBM and SBM, respectively.

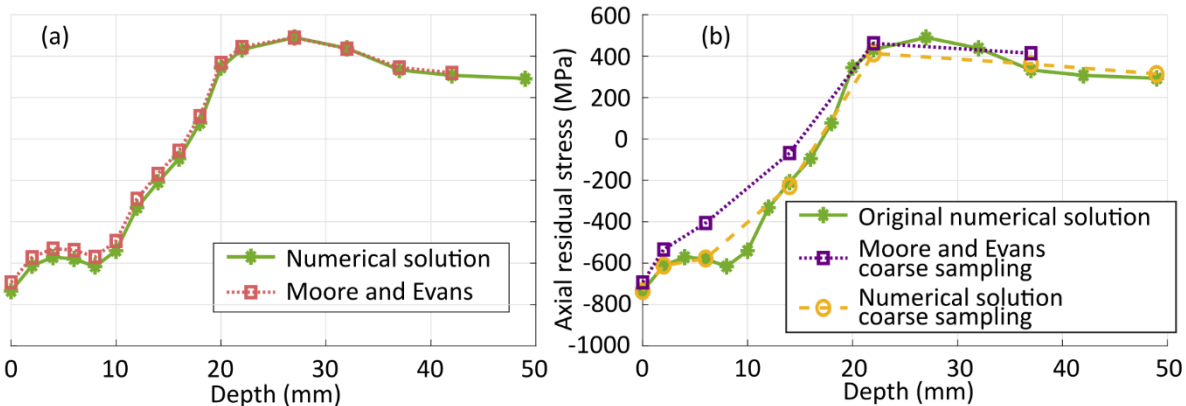
There is a cross in Figure 57 marking the residual stress measurement on the segment A surface before it was cut in half and processed by the SBM. This point could be used as the stress value

in the region on edge, where it was not possible to be measured, instead of using the extrapolated value. However, even with the extrapolations, the residual stress distribution determined by the SBM is sufficiently accurate.

The railway axle's axial and tangential stress were measured precisely, with a relatively low scatter in the values. Thanks to the SBM specimen's shape, it was possible to measure also the radial components (this is impossible in the LRBM). There is a noticeable scatter in the values of radial stress (see Figure 54 and Figure 55). However, radial stress is not very important regarding crack propagation. In a model of the whole axle, the radial component is usually calculated automatically to match the state of the other two components, which are also much more significant in magnitude.

Both presented methods are destructive, so it is impossible to repeat the measurements I production very frequently. That is their biggest drawback. However, it is expected that the measured axle represents the whole series of manufactured axles (with the same technological processes and parameters), which will have similar residual stress distribution. Therefore, sacrificing one axle to be destroyed by the experimental procedure is acceptable.

The advantage of the LRBM, in particular, lies in need for one specimen only. Also, if using FEM is not possible for some reason, there is the possibility of using the developed iterative procedure to evaluate the experimental data. The Moore and Evans formula was also applied to the data measured here, and the residual stress distribution was compared to the numerically obtained distribution. The comparison is plotted in Figure 58 (a) – the obtained distributions are practically identical. However, suppose only some measured values are used for the evaluation, simulating a coarser sampling. In that case, the numerical procedure can produce results closer to reality, see Figure 58 (b). This enhancement gives the proposed LRBM a slight advantage over the original layer removal method with the analytical evaluation.



**Figure 58 Comparison of axial residual stress evaluated by different methodologies from the same measured data with (a) fine depth sampling and (b) coarse depth sampling**

Should the residual stress be non-uniformly distributed around the axis (not axisymmetric)? The LRBM can show the circumference because of the measurements in 3 places (it could be even more). The main disadvantage is the repeated time-consuming machining.

The main advantage of the SBM is that no additional machining of the specimens is needed once they are cut out of the axle, which saves a considerable amount of time and costs. A FEM software is necessary for the final residual stress evaluation, but such equipment is relatively standard in more

prominent industrial manufacturers like railway axle producers. Another minor disadvantage is that measuring residual stress by XRD near original outer and inner surfaces is practically impossible. However, an additional measurement performed before the cutting can reduce this problem for the outer surface.

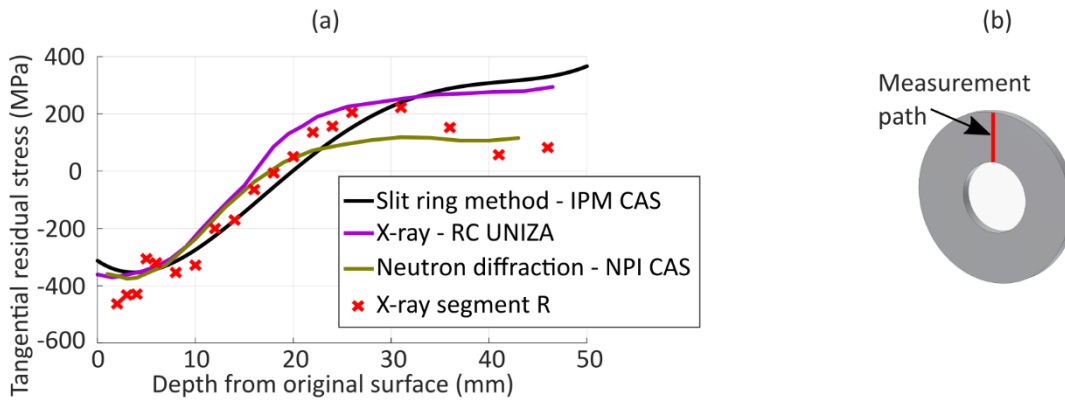
Successful application of the methods described above shows that the XRD applied to an appropriate specimen can provide information about the residual stress distribution not only close to the body surface (ca 10  $\mu\text{m}$ , see Figure 21 – X-ray diffraction method) but also in the whole cross-section, provided that a numerical FEM simulation is applied to obtain the correct results. The LRBM and the SBM require standard tools available in industrial companies, i.e., a set of XRD equipment and FEM software.

The described methods both rely on the use of the same procedure of residual stress measurement – the XRD. Although their compliance is acceptable, and an analytical calculation verified the evaluation procedure, this alone cannot be taken for sufficient validation. Therefore, additional experiments using different techniques were carried out to validate the obtained results.

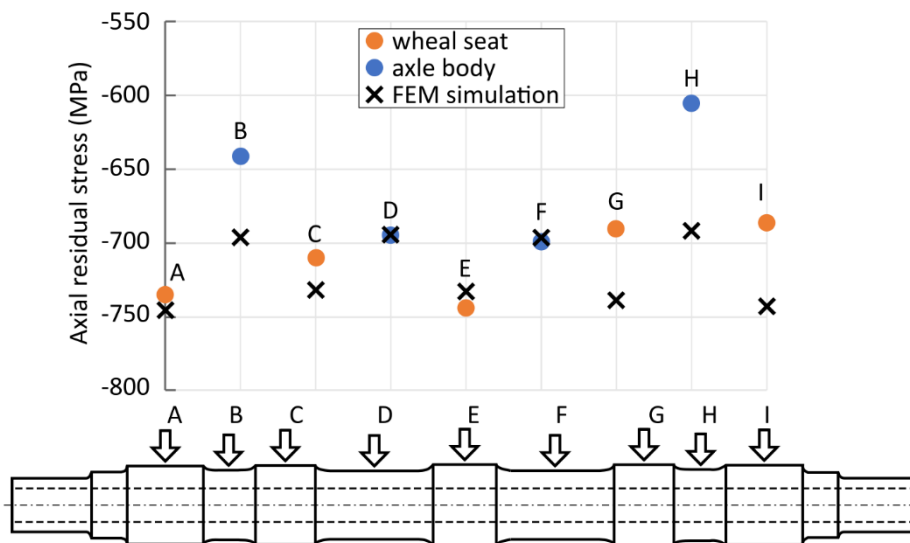
In order to perform the referential measurements, preferably on the same geometry used by one of the two methods above (for the necessity of transporting the specimens), the shape of a ring specimen (the same as the segment R for the SBM) was chosen, see Figure 59 (b). The ring specimens were manufactured from a different axle of the same type as the one studied in this work. The following methods measured tangential residual stress distribution in these specimens:

1. *neutron diffraction* – performed by the Nuclear Physics Institute of the Czech Academy of Sciences, Řež, Czech Republic
2. *slit ring method* – performed at the Institute of Physics of Materials of the Czech Academy of Sciences by the authors of this work; this experiment was already published by Dlhý et al. [225], where the detailed description can be found
3. *X-ray diffraction* – additional XRD measurement performed by the Research Centre of the University of Žilina, Žilina, Slovakia.

The comparison of tangential residual stress obtained by these methods is shown in Figure 59 (a). The solid lines in Figure 59 (a) stand for the referential results from specimens manufactured from a different railway axle. The red points represent the results obtained by the SBM on the segment R, already presented previously. All the methods show similar results up to the depth of 18 mm, where most of the methods show crossing from compression to tensile residual stress distribution. After 18 mm, only tensile residual stress is present in the following depth. Here some differences begin to appear. Only the X-ray measurement of the segment R shows decreasing in the residual stress after 30 mm depth. Other methods show constant value after 30 mm depth. Neutron diffraction shows 100 MPa as the maximum tensile value. Other methods show a maximum tensile value of 200 MPa or higher. As was mentioned above, specimens for different measurements were extracted from different axles after induction hardening. The tensile residual stress is caused in response to the compressive residual stress generated after surface cooling. Therefore, tensile residual stress may vary for different axles and different axle parts. The most important for crack propagation is surface area. In this area, all methods show similar compressive residual stress.



To validate the residual stress estimation for the whole railway axle, the comparison of FEM results and XRD measurement on the surface of the original axle was performed. XRD measurement was performed before any cut-out operation of the specimens for the residual stress measurement. Figure 60 shows the schematic illustration of the measured positions with the FEM data estimation with the measurement data in those positions. Data from positions D and F are directly used in residual stress determination by LRBM and SBM. Other data points are the comparison of FEM estimation on the rest of the railway axle with the measured data. Differences between different positions may be caused by imperfections in the technological procedure and imperfections in FEM estimation. The difference between the axle body and the wheel seat positions is caused by the fact that the diameters in these positions are not identical. Therefore, residual stress is equilibrating in the different volume sizes. Positions B and H on the axle body show the largest difference against FEM estimation. This can be caused by a complicated axle shape where the induction hardening parameters should be improved to get a perfect residual stress profile. G, H and I positions on one side of the axle show a larger difference against A, B and C points on the other side. This suggests some influence of the induction hardening direction. Although with some imperfections, the overall FEM estimate is accurate enough for the SIF determination and following RFL estimation.



### 6.3.1 Additional Hardness and Microstructure Analysis

After the residual stress measurement, hardness measurement and microstructure analyses were performed. Hardness was measured with ZHV30 Vickers ZwickRoell at a load of 1kg applied according to the ASTM E384 standard. Measurement was performed on the segment R specimen used for the SBM residual stress measurement. Three different paths from the original outer axle surface up to the depth of 20 mm were measured with spacing 120° to each other. Figure 61 shows obtained hardness. Hardness is more or less constant from the surface (0 mm depth) up to the 8 mm under the surface, around 530 HV1. Then, hardness values decreased up to the 16 mm depth, where constant hardness distribution, around 225 HV1, is observed again.

In order to observe the microstructure of the axle cross-section, five metallographic samples were manufactured from the segment R for the SBM residual stress measurement. Samples were extracted from 2 mm, 5 mm, 10 mm, 15 mm, and 20 mm of the axle depth. Samples were polished and etched in a Nital Etchant. The microstructure was documented by the light microscope Olympus DSX1000. Figure 62 shows the resultant microstructure of the axle after the induction hardening for different depths. Due to the induction hardening, martensite was observed on the surface. The martensitic structure was present to the depth of 7.5 mm, where a transition area containing bainite occurred. The volume fraction of the bainite was increasing with increasing depth. The transition zone was observed up to 16.2 mm, while also a small amount of ferrite from the depth of 13.6 mm appeared. Above 16.2 mm of the axle depth, sorbit was also detected. Table 3 summarizes the documented microstructure behaviour.

The change in microstructure corresponds to the measured hardness and previously measured residual stress distribution.

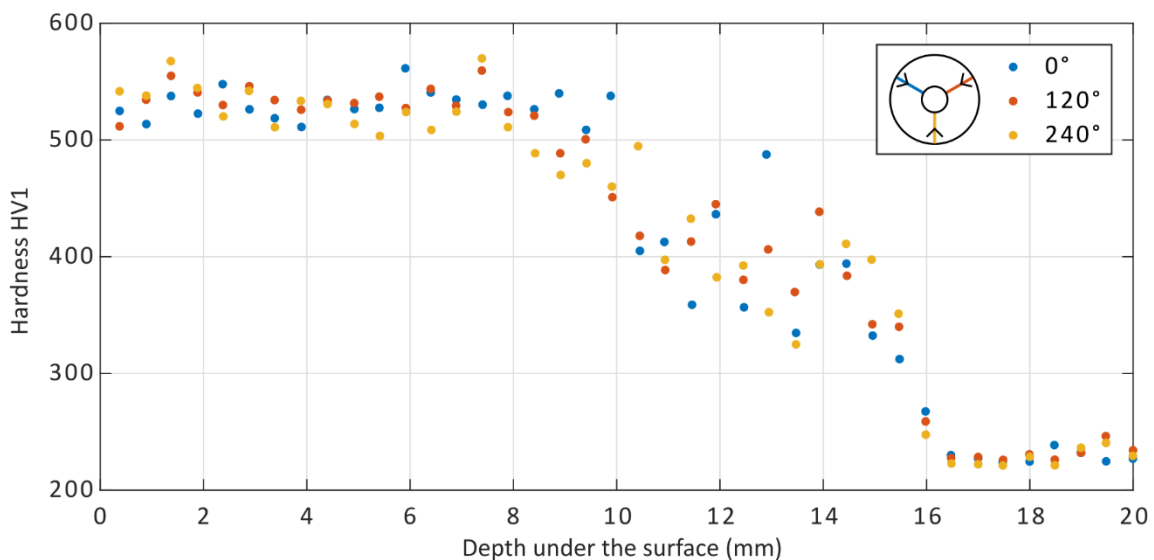
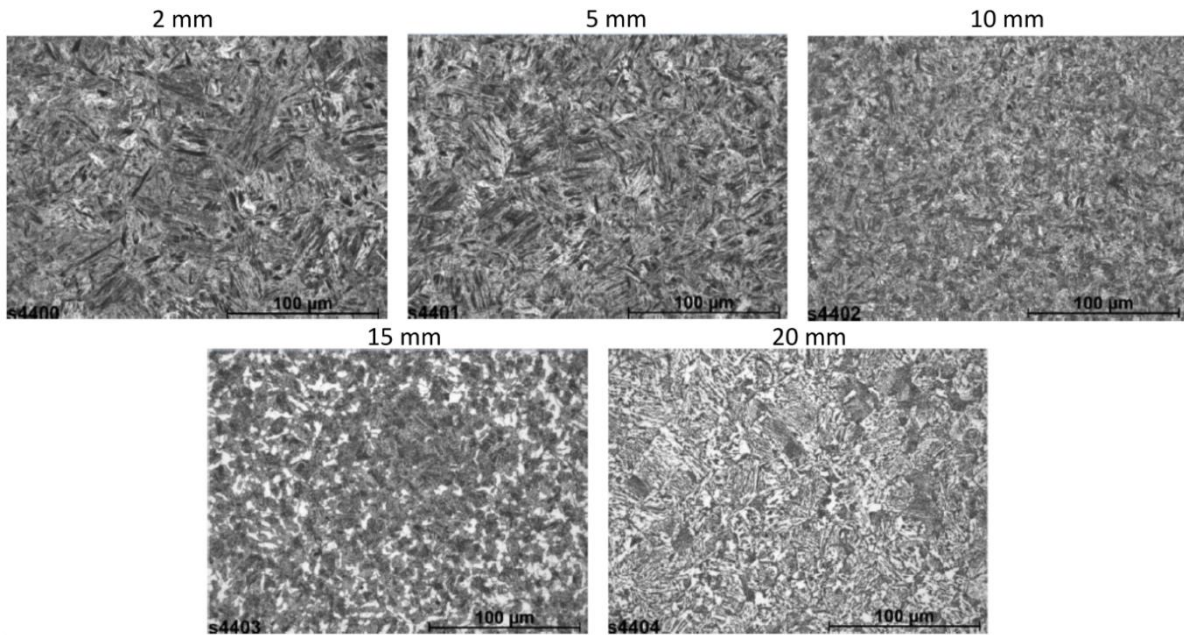


Figure 61 Induction hardened axle hardness

**Table 3 Microstructure summary after the induction hardening**

Depth (mm)	Microstructure
0.0 - 7.5	Martensite
7.5 - 10.7	Martensite + Bainite
10.7 - 13.6	Bainite + Martensite + little Ferrite
13.6 - 16.2	Bainite + Ferrite + little Martensite
16.2 +	Bainite + Ferrite + Sorbit (as before IH)



**Figure 62 Microstructure of the induction hardening axle. Samples were extracted from different axle depths**

The correctness of the numerical evaluation was verified by comparison with a previously published analytical solution for layer-removal residual stress measurement for the axial residual stress component. Then a completely new measurement procedure, SBM, which combines XRD and numerical evaluation, was performed. Both procedures, LRBM and SBM, achieved practically identical results. Additional verification was performed by measuring the tangential residual stress using conventional residual stress measurement methods on ring specimens manufactured from the axle. Obtained tangential results are very similar. Lately, axial residual stress results were compared with externally performed slitting method measurement. The comparison showed the same trend.

## 7 Stress Intensity Factor Determination

The previous text described the stress field determination caused by different loading conditions (bending load, press-fit, and residual stress) and estimated the critical position for the investigated railway axle. In the next section, SIF determination by the numerical simulation is described in detail. Different methods and their accuracy will be discussed. First, SIF determination for the rolling bearing cylinder with the internal crack, then SIF determination for the investigated railway axle will be presented.

The SIF determination is not a trivial process. It is necessary to perform a detailed analysis of the component with the crack. Determined SIFs are typically used in RFL estimation, where the precision of the SIF determination influences the final RFL estimation. Different loading conditions may cause different SIF modes. Therefore, proper investigation of the complex loading condition and precise SIF determination is critical for the correct RFL estimation. During the PhD study, SIF determination for the different project was necessary. Complex analysis and RFL determination of the bearing element with internal crack was performed before the railway axle SIF determination.

### 7.1 Compression Loaded Central Cracked Cylinder

One atypical mechanism of failure of the bearing elements is that the crack propagates from an internal defect until it reaches a critical length and the bearing element breaks. This mechanism is essential for thermoplastic bearing elements, especially cylinders. Thermoplastic cylindrical bearing elements are typically manufactured by injection moulding. However, internal defects occur in the cylinders due to significant shrinkage from the molten polymer solidification in the mould after the injection [226]. When a defected cylinder is installed in a bearing and starts rolling under load, a crack can initiate from the shrinkage defect and start propagating. This process eventually results in the failure of the cylinder. The crack grows under mixed-mode conditions caused by the ever-changing orientation of the crack to the load acting during rolling. As the production defects are complicated to eliminate [226], it is crucial to describe the process that leads to failure and thus enables a reasonable lifetime estimation of these parts.

The frequent presence of mixed-mode conditions in fracture mechanics problems concerning parts such as bearing elements or gears made of thermoplastics such as POM, PEEK, and others, fuel recent interest in obtaining the crack growth conditions in these materials in mixed-mode conditions. It was found that mixed-mode loading conditions lead to an apparent lifetime reduction in the case of mode I/mode III loading [227]. Additionally, during fatigue testing in mixed-mode conditions, a temperature increase caused by friction between crack flanks was observed. This temperature increase depends on the loading frequency and can significantly deteriorate the mechanical properties of the polymer. Therefore, any lifetime prediction for polymeric material that neglects the effect of the mixed-mode conditions leads to strongly non-conservative results.

The detailed knowledge of the mode mixity and accurate estimation of the SIFs during crack propagation is necessary for further lifetime prediction of the component. A thorough FEM simulation of an actual component where crack propagates in mixed-mode conditions is also essential for further practical application of previous research findings on the mixed-mode crack propagation in thermoplastics [227]–[229].

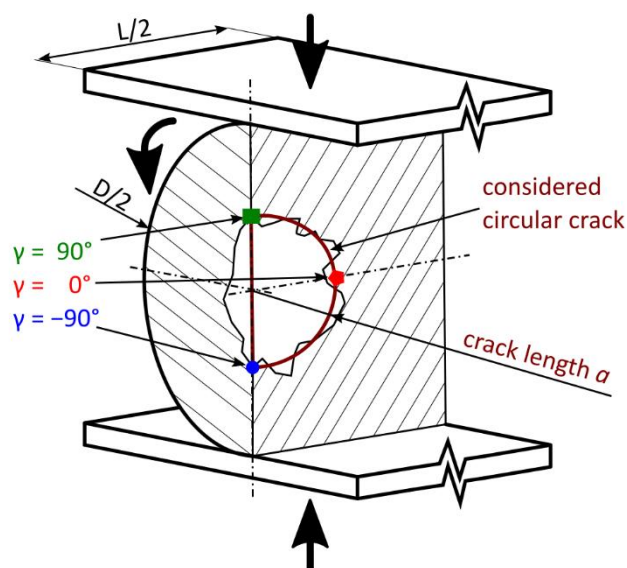
Detailed FEM simulation of the crack propagation in cylindrical bearing elements made of POM during rolling is described in the following section. This study was supported by project PCCL-K1 “K1-Center in Polymer Engineering and Science”, and is a direct follow-up to the work of Berer et al. [226], but it takes into account the presence of the mixed-mode conditions at the crack front. The SIFs for mode I (tensile crack opening), mode II (in-plane shear crack opening), and mode III (out-of-plane shear crack opening) were determined, and their mutual relationship was assessed. Different conditions of the crack propagation were considered in the simulation.

A parametrical numerical model was developed to simulate a growing crack inside a rolling cylinder under different conditions and determine fracture mechanics parameters – the SIFs.

Three different modifications of the model that differ in some features influencing the crack growth were created:

1. *The model with a flat crack* – a model of a cylinder compressed between two steel plates that contains one circular flat crack in the middle. Although the faces of the crack can come in contact, no friction is considered between the faces. Different combinations of dimensions were considered.
2. *The model with a void* – the crack in this model is not flat from the start, but it starts from a three-dimensional void in the middle of the cylinder. Although it starts from the void, the crack is still flat and circular.
3. *The model with a void and friction* – the same as the model with a void, but friction is considered between the crack faces.

The details of the first model only are described and discussed further in work. Results compare different SIF evaluation methods and general equations that assess SIFs for the cylinder's wide range of dimensions. The details of the other two models are shown in the paper by Dlhý et al. [230].

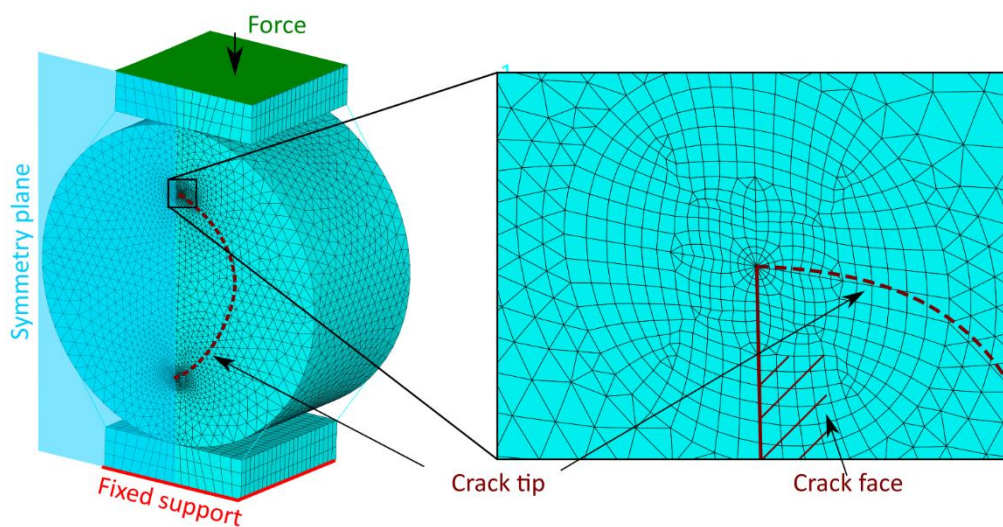


**Figure 63** The situation of the bearing cylinder with an internal defect, compressed between two steel plates and rolling.

The most important part of the model is a cylinder with a flat circular crack in the middle (the crack is modelled directly as a part of the geometry, refer to ANSYS APDL Help for more details about crack analysis [224]). Apart from the cylinder, two steel plates, one at the top and one at the bottom,

compressing the cylinder, were added to model the case of a cylinder installed between rails or bearing rings. The main dimensions of the basic model cylinder are denoted  $D$  (diameter) and  $L$  (length). The crack length is denoted as  $a$ . The model is parametric, which means it is possible to simulate almost any set of dimensions and the change in orientation of the crack during the rotation of the cylinder. See the modelled situation in Figure 63.

Only one-half of the cylinder was modelled to take advantage of the symmetry and reduce the number of elements and computing time. Further reduction of the model was not possible because other planes of symmetry are disrupted by the rotation of the crack inside the cylinder. Quadratic tetrahedral elements were used to mesh most of the model. The mesh was made very fine and a little more regular around the crack front. The quadratic brick mesh was used in the area surrounding the crack front with special quarter-point elements directly at the crack front (see the mesh of the model with a detailed view of the crack front in Figure 64). The material model of the cylinder was a linear elastic, isotropic solid defined by Young's modulus of 3.6 GPa and Poisson's ratio of 0.45. These values are typical for the POM used to make bearing elements.



**Figure 64** The mesh of the whole symmetrical FEM model of the bearing cylinder. The refined area in the vicinity of the crack tip is pictured in the detailed view (note the special crack tip elements in the middle).

The steel plates compressing the cylinder at the top and the bottom were meshed by regular quadratic bricks. The material model of these parts was linear elastic isotropic, with Young's modulus of 210 GPa and Poisson's ratio of 0.3. Mutual contact was defined between the steel plates and the cylinder.

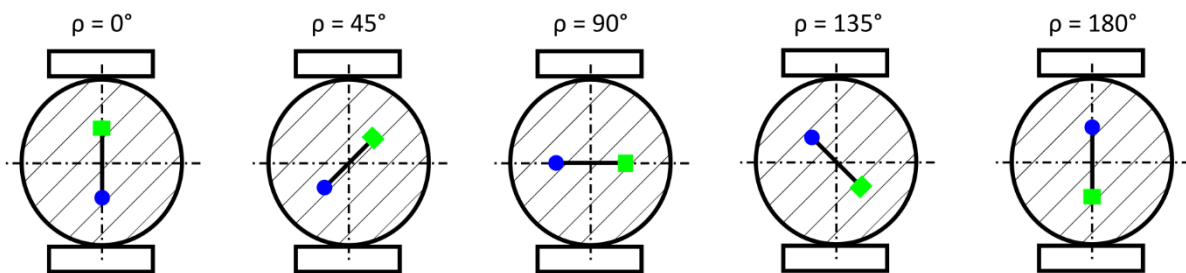
Boundary conditions were defined for the whole model. Symmetrical boundary conditions were defined on the plane of symmetry. Fixed support was defined at the bottom of the lower steel plate. The upper steel plate was loaded by the force of 350 N. The boundary conditions and loads are schematically depicted in Figure 64.

The same basic set of 7 combinations of dimensions  $D \times L$  as in Berer et al.'s previous work [226] was chosen to be modelled (dimensions are in mm):  $3 \times 3$ ,  $4 \times 4$ ,  $5 \times 5$ ,  $6 \times 6$ ,  $6 \times 3$ ,  $6 \times 9$ ,  $6 \times 12$ . Nine more combinations were added to make the set more robust for the intended parametric study:  $3 \times 4$ ,  $3 \times 5$ ,  $3 \times 6$ ,  $3 \times 9$ ,  $3 \times 12$ ,  $4 \times 5$ ,  $4 \times 6$ ,  $5 \times 4$ , and  $6 \times 4$ .

The crack growth inside the cylinder was simulated by modelling the cylinder with the crack length  $a$  going from 0.25 mm up to 1.75 mm by the steps of 0.50 mm. The addition of two extra crack lengths of 0.85 mm and 1.00 mm is done to better compare the models with and without a void inside. Note that, in this case, the crack is circular, and the crack length  $a$  is its radius (as shown in Figure 63).

The SIFs  $K_I$ ,  $K_{II}$ , and  $K_{III}$  were determined along the whole crack front for every crack length. The position on the crack front is defined by the angle  $\gamma$  that goes from  $+90^\circ$  across  $0^\circ$  to  $-90^\circ$  (see Figure 63 for illustration).

The cylinder was considered rolling between the two compressing steel plates to simulate the operation of a bearing element. The rolling was achieved by changing the orientation of the crack in the model. It is important to remark that contact was also defined between the crack faces because they would be pressed against each other in some positions. The crack orientation is defined by the angle  $\rho$  between the crack plane and the model vertical axis (or the direction of forces acting on the steel plates, see Figure 65). The angle  $\rho$  goes from  $0^\circ$  up to  $180^\circ$  by the steps of  $15^\circ$ . For a better description of the change in the values during rolling, eight steps of the angle  $\rho$  were added  $-3.8^\circ$ ,  $7.5^\circ$ ,  $11.2^\circ$ , and  $22.5^\circ$ , as well as  $157.5^\circ$ ,  $168.8^\circ$ ,  $172.5^\circ$  and  $176.2^\circ$ . The range  $0^\circ - 180^\circ$  simulates only a half-turn of the cylinder, but the remaining part of the turn would be symmetrical. The crack growth from 0.25 to 1.75 mm, and the SIF determination was carried out in every rolling step. More than 400 simulations in total were carried out.



**Figure 65 Schematic illustration of the changing orientation of the crack during rolling and the angle  $\rho$  that describes the rolling position.**

In every step of the crack propagation (and in every version of the model), the SIFs were evaluated using three different methods. The first method was the domain integral [231], fully integrated into the software ANSYS. The second method was the determination of SIFs directly from the deformation of the nodes of the special crack tip elements [232]. The third method was the direct method of SIFs determination from the stress field around the crack tip.

At first, the SIFs determined by the model with a flat crack were compared to values published by Berer et al. in [226] to validate the functionality of the new model described previously. The numerical model by Berer et al. represents one-eighth of the bearing cylinder. It was not used to determine the values of SIFs  $K_{II}$  and  $K_{III}$ ; only  $K_I$  was evaluated. The values for the case of the cylinder with  $D \times L = 6 \times 6$  mm in the rolling position  $\rho = 0^\circ$  were taken from the paper and compared to the results that the model produced described here. The comparison is plotted in Figure 66.  $K_I$  values are plotted as a function of the position on the crack front described by the angle  $\gamma$ . The discrepancy between the results of the two models is negligible. Figure 67 compares results produced by these methods for a crack length of 1.25 mm. All methods are in the range  $\pm 1\%$  with Berer's values. All the values presented further in this paper were obtained

by the domain integral method. Note that Berer et al.'s values are in the range of  $0^\circ - 90^\circ$  because the one-eighth type of symmetry was used in their model. It was possible because the values of  $K_I$  are symmetrical, as shown by the newer results. However, it would not be possible to use this type of symmetry to evaluate  $K_{II}$  and  $K_{III}$ .

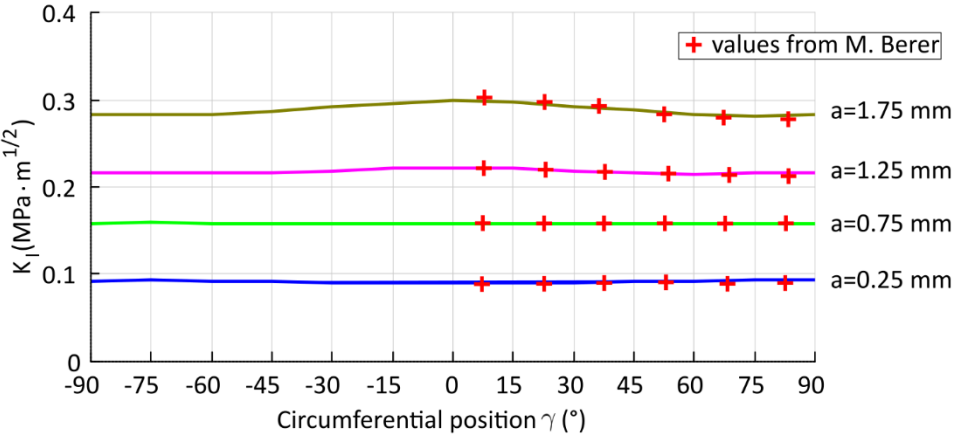


Figure 66 Comparison of  $K_I$  values for different crack lengths from Berer et al. [226] and the newer model described here.

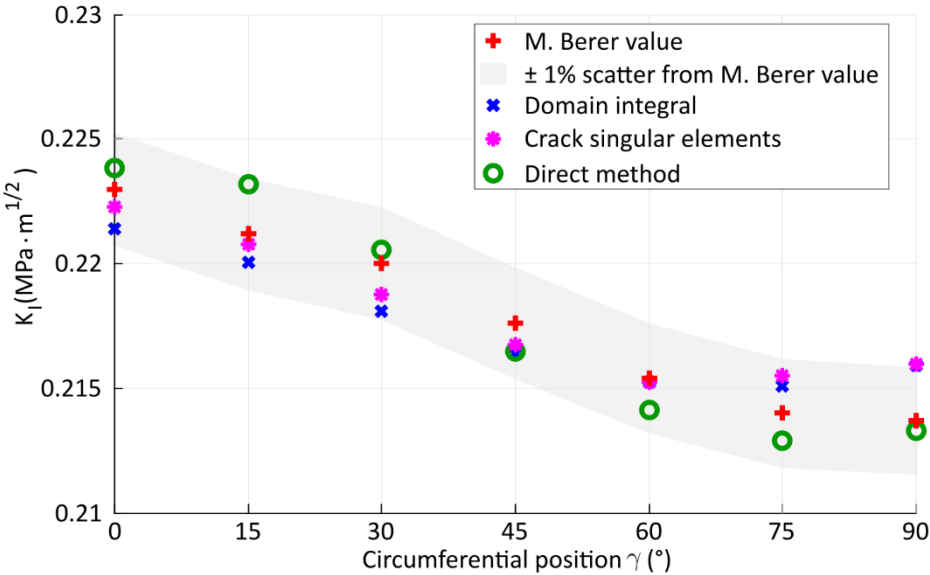


Figure 67 Difference between determined  $K_I$  values for different methods and from Berer et al. [226] for crack length 1.25 mm

7.1.1 The Model with a Flat Crack – Results and Discussion

It was mentioned above that the crack orientation to the acting load changes due to the cylinder rolling. The pure mode I appears only in a few instances during the turn. There is always a combination of modes I, II, and III. The modes and their ratios change depending on the position of the cylinder (angle  $\rho$ ), and they are also different for different positions on the crack front (given by the angle  $\gamma$ ).

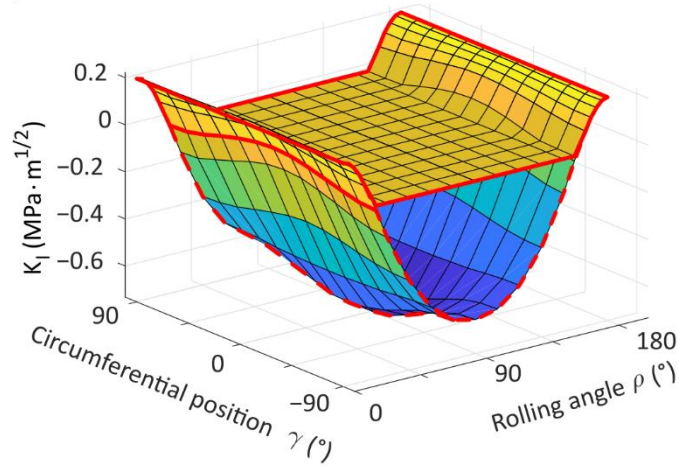


Figure 68 3D plot of  $K_I$  as a function of both, the circumferential position on the crack front  $\gamma$  and the rolling orientation of the crack  $\rho$ , crack length  $a = 1.25$  mm. The upper surface reflects contact between crack faces (highlighted by the solid red line). The lower surface is negative theoretical values of  $K_I$  acquired from a model where no contact was defined between crack faces (highlighted by the dashed red line).

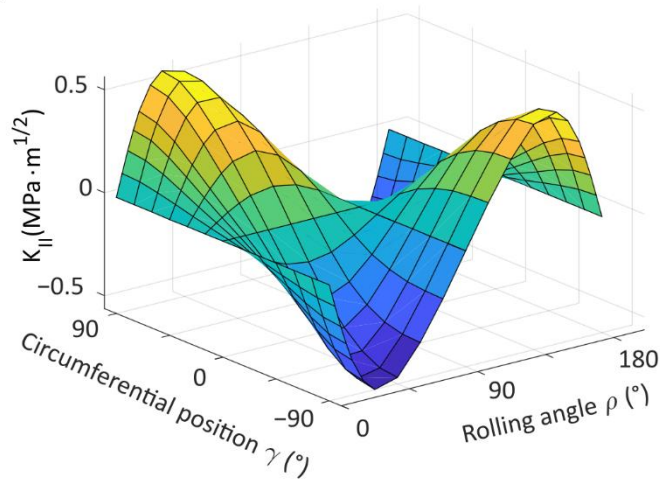


Figure 69 3D plot of  $K_{II}$  as a function of both, the circumferential position on the crack front  $\gamma$  and the rolling orientation of the crack  $\rho$ , crack length  $a = 1.25$  mm.

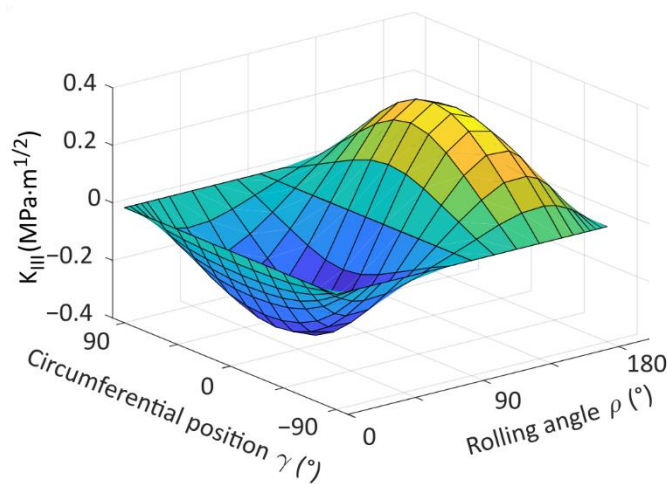


Figure 70 3D plot of  $K_{III}$  as a function of both, the circumferential position on the crack front  $\gamma$  and the rolling orientation of the crack  $\rho$ , crack length  $a = 1.25$  mm.

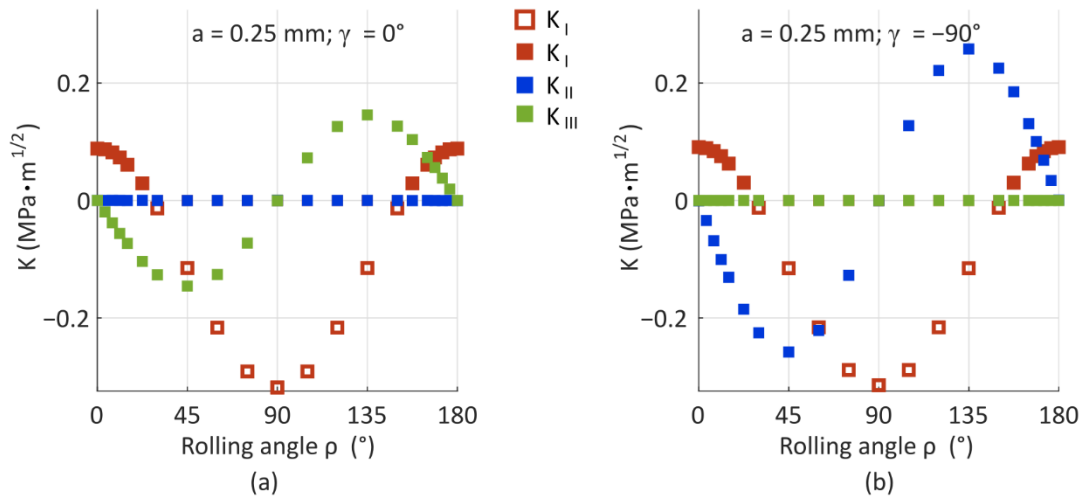


Figure 71 Course of stress intensity factors during rotation in the cylinder  $D \times L = 6 \times 6$  mm, load  $F = 350$  N,  $\alpha = 0.25$  mm, position on the crack front; (a)  $\gamma = 0^\circ$ ; (b)  $\gamma = -90^\circ$ .

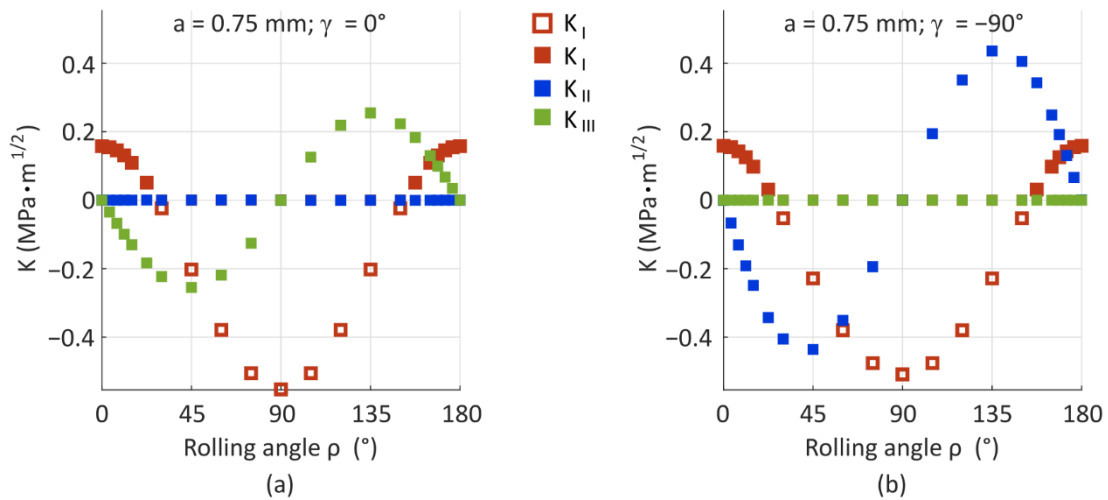


Figure 72 Course of stress intensity factors during rotation in the cylinder  $D \times L = 6 \times 6$  mm, load  $F = 350$  N,  $\alpha = 0.75$  mm, position on the crack front; (a)  $\gamma = 0^\circ$ ; (b)  $\gamma = -90^\circ$ .

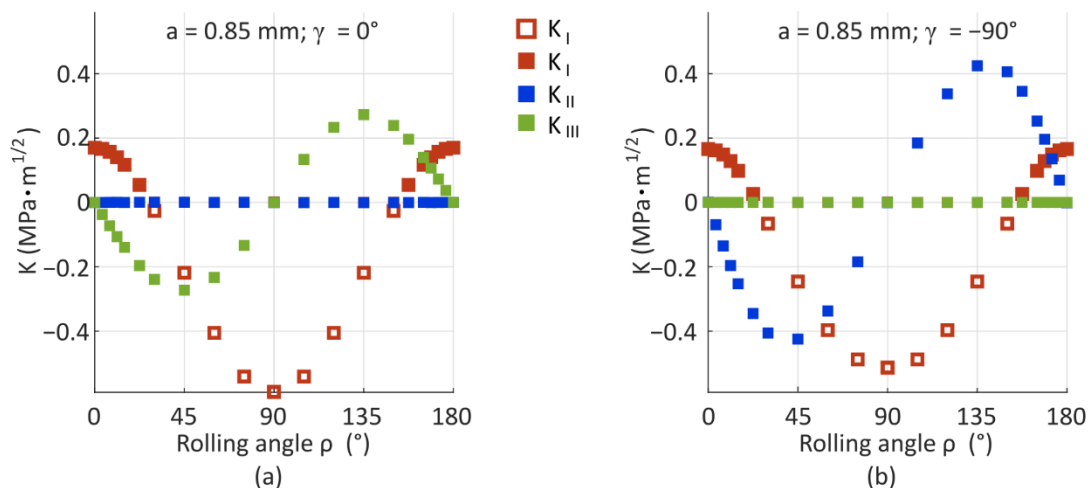


Figure 73 Course of stress intensity factors during rotation in the cylinder  $D \times L = 6 \times 6$  mm, load  $F = 350$  N,  $\alpha = 0.85$  mm, position on the crack front; (a)  $\gamma = 0^\circ$ ; (b)  $\gamma = -90^\circ$ .

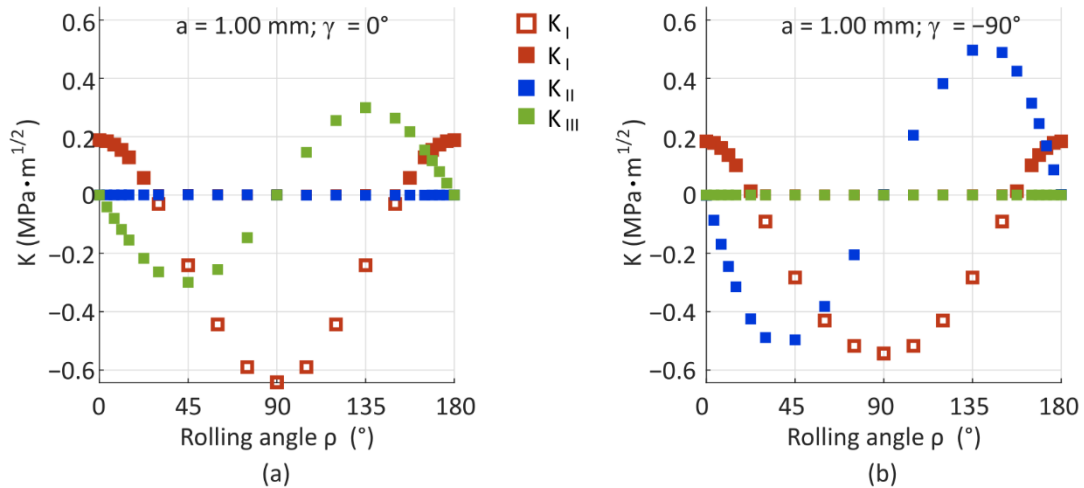


Figure 74 Course of stress intensity factors during rotation in the cylinder  $D \times L = 6 \times 6$  mm, load  $F = 350$  N,  $\alpha = 1.00$  mm, position on the crack front; (a)  $\gamma = 0^\circ$ ; (b)  $\gamma = -90^\circ$ .

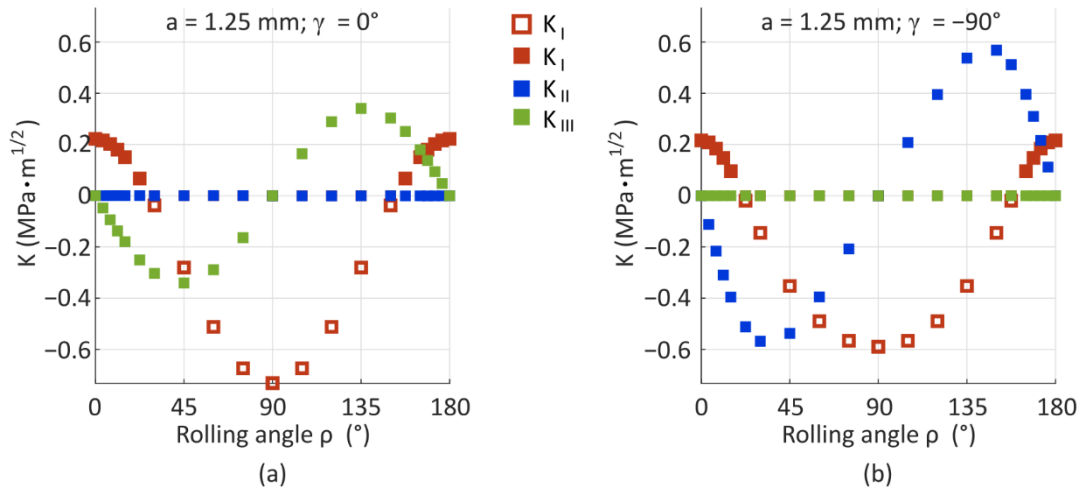


Figure 75 Course of stress intensity factors during rotation in the cylinder  $D \times L = 6 \times 6$  mm, load  $F = 350$  N,  $\alpha = 1.25$  mm, position on the crack front; (a)  $\gamma = 0^\circ$ ; (b)  $\gamma = -90^\circ$ .

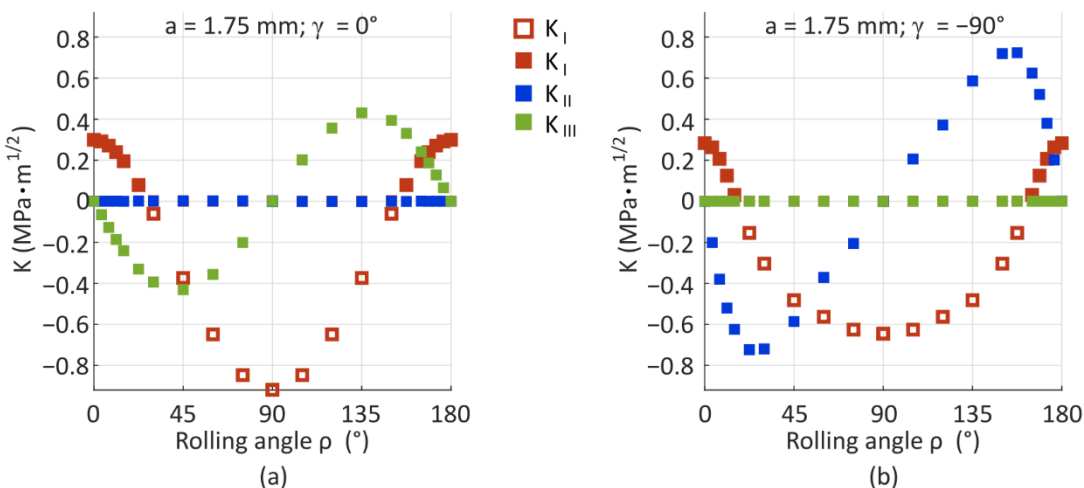


Figure 76 Course of stress intensity factors during rotation in the cylinder  $D \times L = 6 \times 6$  mm, load  $F = 350$  N,  $\alpha = 1.75$  mm, position on the crack front; (a)  $\gamma = 0^\circ$ ; (b)  $\gamma = -90^\circ$ .

The results of the basic model with a flat crack provide an idea of how the modes change during one turn of the cylinder. The presented figures contain plotted results for the cylinder with the dimensions of  $D \times L = 6 \times 6$  mm and loading force  $F = 350$  N unless stated otherwise. The results are plotted in Figure 68 ( $K_I$ ), Figure 69( $K_{II}$ ), and Figure 70 ( $K_{III}$ ) for the one simulated crack length – 1.25 mm. 3D plots were chosen to visualize the overall behaviour of the SIF depending on the position on the crack front  $\gamma$  and the rolling orientation  $\rho$  of the crack. The results were also plotted in 2D plots (from Figure 71 to Figure 76), where the crack length  $a$  and the crack front position  $\gamma$  were fixed, and the SIFs were plotted as a rolling orientation function (angle  $\rho$ ). Only the most interesting 2D plots are included in the work.

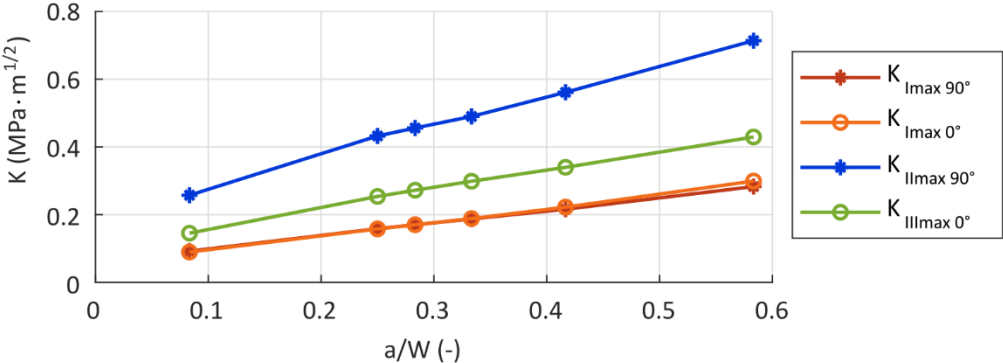
The 3D plot of  $K_I$  (Figure 68) shows that the  $K_I$  values reach their maximum at the beginning and the end of the cylinder turn. During the turn from  $0^\circ$  towards  $180^\circ$ , the values decrease up to the point when the two crack faces come into contact. The crack stays closed until the cylinder comes into a position where the opening stress starts acting on the crack again. The  $K_I$  values are zero when the model's crack faces are in contact. If no contact is defined between the crack faces, the  $K_I$  values become negative in the part of the cycle where the crack is closed (the negative values are also plotted in Figure 68). Negative values of  $K_I$  cannot occur in reality. However, this kind of simulation helps evaluate the cycle of  $K_I$  and its asymmetry.

The values of SIFs for the shear modes, the  $K_{II}$  and  $K_{III}$ , are higher in magnitude than the  $K_I$  in terms of maximum values. At the beginning of the turn, both  $K_{II}$  and  $K_{III}$  are zero along the whole crack front, as the crack is not subjected to shear loading at all. However, the conditions change with the turning. The middle of the crack ( $\gamma = 0^\circ$ ) is subjected to mode III type of loading, and mode II does not appear here at all during the turn. In contrast, the crack front “ends” ( $\gamma = 90^\circ$  and  $-90^\circ$ ) develop mutually opposite values of  $K_{II}$  during the cycle, and  $K_{III}$  remains equal to zero. In between these positions, the  $K_{II}$  and  $K_{III}$  values follow different sine patterns. As the crack becomes perpendicular to the direction of loading ( $\rho = 90^\circ$ ), both shear modes disappear again. Then, in the following part of the turn, the values of  $K_{II}$  and  $K_{III}$  appear again in the same places on the crack front but with opposite signs – see Figure 69 and Figure 70.

The crack tip mixed-mode loading has a completely out-of-phase character. When the  $K_I$  reaches the maximum values, both  $K_{II}$  and  $K_{III}$  are zero. When the  $K_{II}$  and  $K_{III}$  reach their maxima, the crack is closed ( $K_I$  is zero). This means that the crack faces are being forced against each other and into one of the shear modes simultaneously.

The instant values of  $K$  are not very practical for describing the crack growth kinetics in the investigated situation. Using the maximum SIF  $K_{max}$  to describe the whole cycle is more practical. In Figure 77, these values are plotted as a function of the normalized crack length  $a/W$  (where  $a$  is the crack length, and  $W$  corresponds to the radius or half of the length of the whole cylinder depending on position  $\gamma = 90^\circ$  ( $-90^\circ$ ) or  $\gamma = 0^\circ$ , respectively (see Figure 63)). It is important to note here that the rolling position  $\rho$ , at which the maxima and minima of  $K_I$  and  $K_{III}$  are reached, are constant with the growing crack length  $a$ . The maximum of  $K_I$  can always be found at  $\rho = 0^\circ$  and  $\rho = 180^\circ$ , and the (theoretical) minimum at  $\rho = 90^\circ$ . The maximum of  $K_{III}$  stays at  $\rho = 135^\circ$  and the minimum at  $\rho = 45^\circ$ . However, the position where the  $K_{II}$  reaches its extreme (minimum or maximum depending on the position, if  $\gamma = 90^\circ$  or  $-90^\circ$ ) gradually shifts from  $45^\circ$  towards lower values of  $\rho$  with the crack length increasing and similarly the position of the other extreme shifts

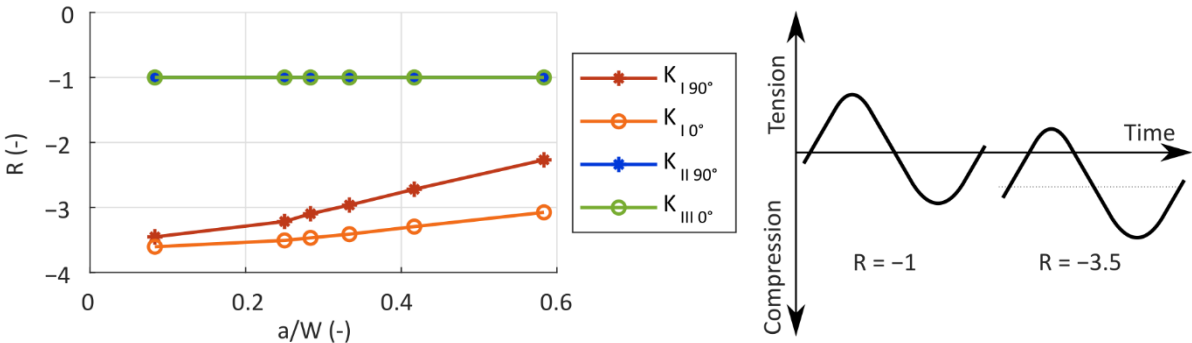
from 135° towards higher values. The shift can be observed in Figure 71 – Figure 76. The cause of this is most likely that the crack becomes more influenced by a complicated stress state in the vicinity of the contact with the loading plates, which manifests itself the most at the positions  $\gamma = 90^\circ$  and  $-90^\circ$ , where  $K_{II}$  reaches its maxima and minima. This shift in the position does not influence the characterization of the SIF cycles using the  $K_{max}$  values, though.



**Figure 77** Maximum stress intensity factors in the rolling cycle for different crack tip positions  $\gamma$  depending on the normalized crack length. The indices  $0^\circ$  and  $90^\circ$  indicate the position  $\gamma$  at the crack front.

However, the magnitude of the SIF itself does not provide information about the character of the cycle. For the loading cycle accurate description, it is necessary to specify also the asymmetry of the cycle in terms of  $R$ -ratio. The  $R$ -ratio is the ratio of the minimum value  $K_{min}$  to the maximum value  $K_{max}$  of the cycle.

In the investigated case, the  $R$ -ratio depends on the position at the crack front and the current crack length. The dependency is plotted in Figure 78. In the case of mode I, the  $R$ -ratio is negative. The ratios of KI in all the positions are rising with the growing crack. Additionally, the difference between the positions becomes more pronounced with the crack growing larger. The reason probably is that the position of  $\gamma = 90^\circ$  ( $-90^\circ$ ) starts to be more influenced by the stress distribution caused by the contact zone of the bearing element and steel plates when the crack length grows larger. In the mode II case, the  $R$ -ratio of -1 (this denotes an asymmetrical cycle) is the same for every crack front position, apart from  $0^\circ$ , where the  $K_{II}$  is 0. Analogically to mode II, the  $R$ -ratio for mode III is equal to -1, apart from the  $90^\circ$  and  $-90^\circ$  positions.



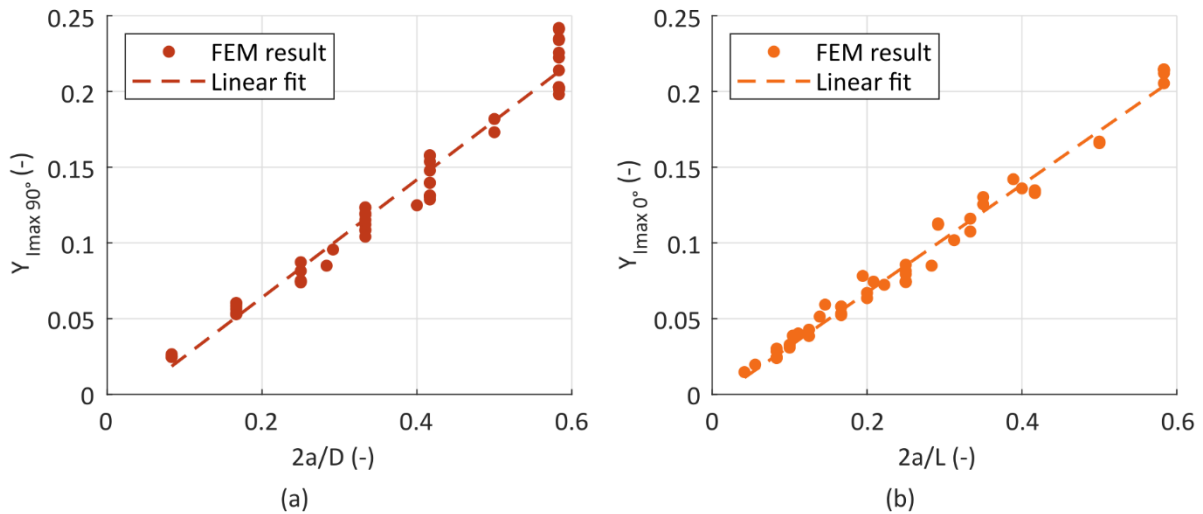
**Figure 78** The  $R$ -ratio for different loading modes at different positions on the crack front during crack growth (left) with a schematic illustration of loading cycles with different  $R$ -ratios (right). The indices  $0^\circ$  and  $90^\circ$  indicate the position  $\gamma$  at the crack front

The  $K_{max}$  values were determined for more combinations of dimensions  $D \times L$ . The considered diameters  $D$  were 3, 4, 5, 6 mm, and the considered lengths  $L$  were 3, 4, 5, 6, 9, and 12 mm.

The entire range of crack lengths, as it is specified previously, was considered for the 6 × 6 mm type of cylinder only. Only some crack lengths were considered for the other combinations of length and diameter. These crack lengths were chosen concerning the articular combination dimensions because some of the lengths did not fit in the particular combination.

The obtained values of  $K_{max}$  were then fitted with parametric functions that define the dependency of the SIFs on the crack length and are generalized concerning the loading force and dimensions of the cylinder. The fits were carried out for every crack face point, where the SIF reaches its maximum during the turn. This means there is one fit for the  $K_{I,max}$  in the  $\gamma = 90^\circ$  position and one for the  $K_{II,max}$  in the  $\gamma = 0^\circ$  position. Two fits for the  $K_{I,max}$  were made, one for the  $90^\circ$  position and another for the  $0^\circ$  position, because the difference between the maxima in these two positions is not very pronounced. However, technically, the global maximum is reached only in the  $0^\circ$  position.

The functions are slightly different for every type of SIF. However, they always feature the loading force  $F$ , the square route of the crack length  $a$ , one of the dimensions of the cylinder (either the diameter  $D$  or the length  $L$ ), and a dimensionless shape function  $Y$  that was found by curve fitting.



**Figure 79 a) Parametric functions fitting the values of  $Y_{I,max 90^\circ}$ ; (b) Parametric functions fitting the values of  $Y_{I,max 0^\circ}$**

The shape function curve fits for the  $K_{I,max 90^\circ}$ , and  $K_{I,max 0^\circ}$  are plotted in Figure 79 (a), (b), respectively. The equation describing the dependencies are the following:

$$K_{I,max 90^\circ} = \frac{F}{\sqrt{10^3} \sqrt{a} L} Y_{I,max 90^\circ} \left( \frac{2a}{D} \right), \quad (28)$$

$$K_{I,max 0^\circ} = \frac{F}{\sqrt{10^3} \sqrt{a} D} Y_{I,max 0^\circ} \left( \frac{2a}{L} \right), \quad (29)$$

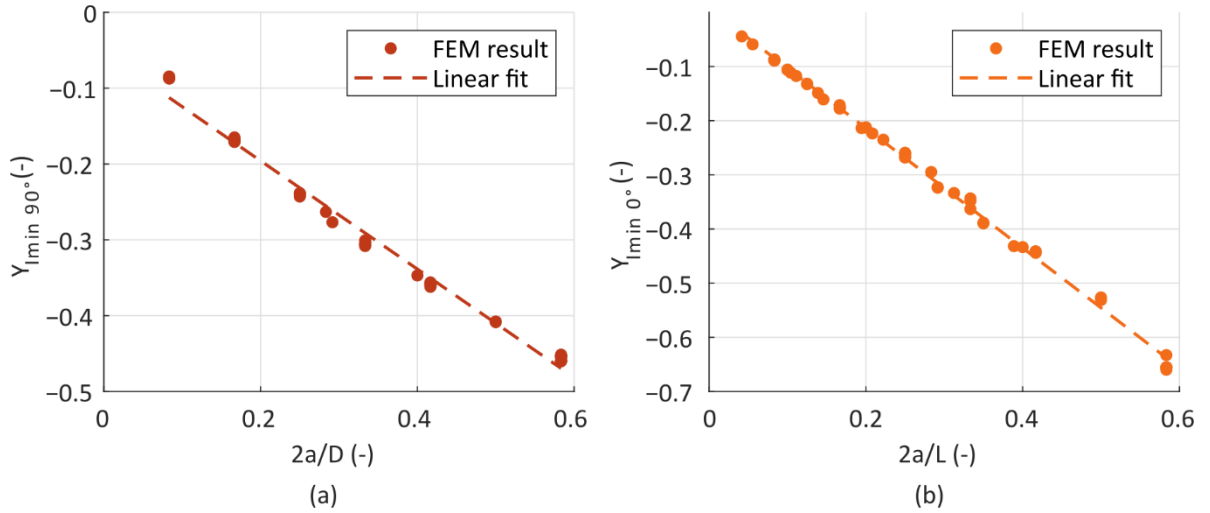
where  $F$  is the loading force in N,  $a$  is the crack length in mm,  $D$  is the cylinder diameter in mm,  $L$  is the cylinder length in mm and  $Y_{I, 90^\circ}$ , and  $Y_{I, 0^\circ}$  are the dimensionless shape functions that have been found in the following form:

$$Y_{I,max 90^\circ} \left( \frac{2a}{D} \right) = 0,389 \left( \frac{2a}{D} \right) - 0,014, \quad (30)$$

$$Y_{I_{max} 0^\circ} \left( \frac{2a}{L} \right) = 0,354 \left( \frac{2a}{L} \right) - 0,004. \quad (31)$$

Even though the dimensions are in mm, the resultant unit of the SIFs calculated using Equations (28) and (29) is in  $\text{MPa}\cdot\text{m}^{1/2}$ , which is the typical unit used for the SIFs. This is ensured by the factor of  $\sqrt{10^3}$  in the denominator of both equations.

The points scattered around the line in Figure 79 determine the level of generalization achieved by the fit, and the difference between the parametric functions and the actual determined values. For  $Y_{I_{max} 0^\circ}$  and  $Y_{I_{max} 90^\circ}$ , the difference is usually not more than 6%. However, for some combinations, it goes up to 30% (especially when there is a more significant difference between  $D$  and  $L$  of the cylinder).



**Figure 80 (a) Parametric functions fitting the values of  $Y_{I_{min} 90^\circ}$ ; (b) Parametric functions fitting the values of  $Y_{I_{min} 0^\circ}$ .**

To describe the cycle of  $K_I$  properly, the  $K_{I_{min}}$  values are also needed because the  $R$ -ratio does not stay constant for the  $K_I$  cycle during the crack propagation (as illustrated in Figure 78). Even though the  $K_{I_{min}}$  values are only theoretical because, in practice, the crack is closed, and the SIF is equal to zero, knowing these values makes it possible to describe the whole cycle in detail and, most importantly, to determine the precise moments of the crack closing and opening. The  $K_{I_{min}}$  functions were created in the same manner as the  $K_{I_{max}}$  functions above. The shape function fits are plotted in Figure 80 (a) and (b). The equations follow:

$$K_{I_{min} 90^\circ} = \frac{F}{\sqrt{10^3} \sqrt{a} L} Y_{I_{min} 90^\circ} \left( \frac{2a}{D} \right), \quad (32)$$

$$K_{I_{min} 0^\circ} = \frac{F}{\sqrt{10^3} \sqrt{a} D} Y_{I_{min} 0^\circ} \left( \frac{2a}{L} \right). \quad (33)$$

The  $Y_{I_{min} 90^\circ}$  and  $Y_{I_{min} 0^\circ}$  are the dimensionless shape functions that have been found in the following form:

$$Y_{I_{min} 90^\circ} \left( \frac{2a}{D} \right) = -0,714 \left( \frac{2a}{D} \right) - 0,053, \quad (34)$$

$$Y_{Imin\ 0^\circ} \left( \frac{2a}{L} \right) = -1,106 \left( \frac{2a}{L} \right) + 0,008. \quad (35)$$

The parametric functions were also found for the  $K_{II\max\ 90^\circ}$  and  $K_{III\max\ 0^\circ}$  values. The fits for these values are plotted in Figure 81 (a), (b), respectively. The generalized  $K_{II\max}$  and  $K_{III\max}$  are much less scattered, which means that the parametric function perfectly estimates the actual SIF values. The parametric functions have a similar form to the previous functions of  $K_{I\max}$ . The equations are the following:

$$K_{II\max\ 90^\circ} = \frac{F}{\sqrt{10^3} \sqrt{a} L} Y_{II\max\ 90^\circ} \left( \frac{2a}{D} \right), \quad (36)$$

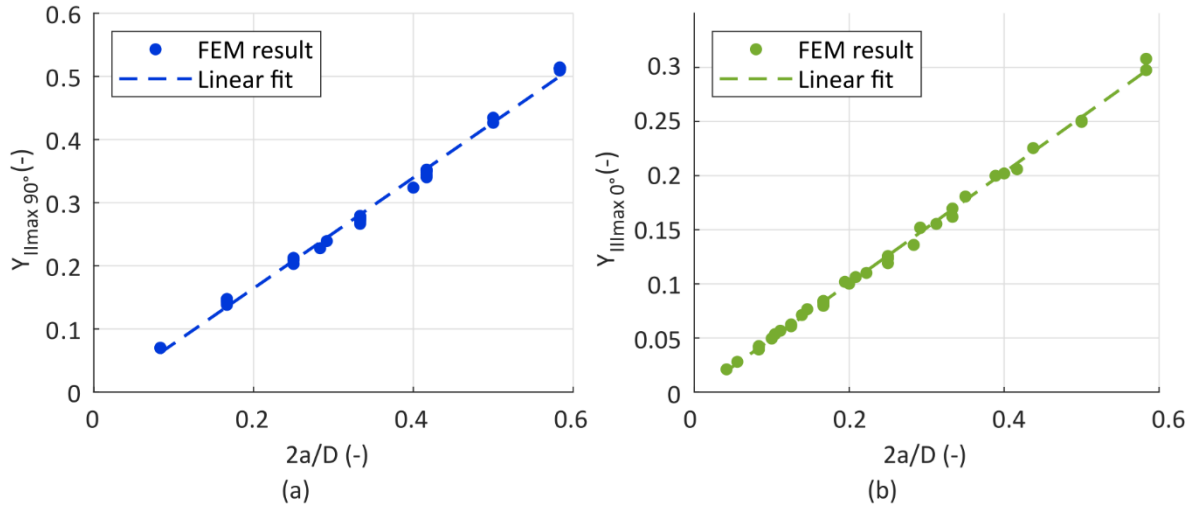
$$K_{III\max\ 0^\circ} = \frac{F}{\sqrt{10^3} \sqrt{a} D} Y_{III\max\ 0^\circ} \left( \frac{2a}{L} \right), \quad (37)$$

The equations describing functions  $Y_{II\ 90^\circ}$  and  $Y_{III\ 0^\circ}$  were found to be the following:

$$Y_{II\max\ 90^\circ} \left( \frac{2a}{D} \right) = 0,884 \left( \frac{2a}{D} \right) - 0,012, \quad (38)$$

$$Y_{III\max\ 0^\circ} \left( \frac{2a}{L} \right) = 0,512 \left( \frac{2a}{L} \right) - 0,002. \quad (39)$$

Again, all the input dimensions in Equations (5) – (8) are in mm, and the load  $F$  in N. The resultant unit of the SIF is  $\text{MPa} \cdot \text{m}^{1/2}$ .



**Figure 81 (a) Parametric functions fitting the values of  $Y_{II\max\ 90^\circ}$ ; (b) Parametric functions fitting the values of  $Y_{III\max\ 0^\circ}$ .**

All of the above stated equations are valid only in the range of  $0 < 2a/D < 0.6$  and  $0 < 2a/L < 0.6$ , respectively, because the SIFs were not evaluated outside this range. Care must also be taken if using the equations for a similar situation with different material parameters. Although the material parameters do not influence the SIFs directly, they can influence the contact zone. This means that SIF values for larger crack lengths  $a$  may be influenced by the material parameters. However, the rest of the cases will not be influenced by changes in material parameters because the SIFs only depend on the loading force and cylinder dimensions.

## 7.2 The Investigated Railway Axle

The previous section demonstrated how to determine SIFs values for different crack opening modes, different SIF evaluation methods compared to each other, and how one can estimate the function for SIF evaluation with comprehensive numerical analyses.

In this section, the railway axle is investigated again. The development of parametrical numerical models of the railway axles (wheel sets) is described to simulate crack growth in the critical position under the different loading conditions (bending, press-fit, residual stress) and to determine fracture mechanics parameters—the SIFs. The previously determined surface position of the defect is considered first. Then another defect position under the surface is considered for the crack growth. In total, six different modifications of the railway wheelset model with a crack have been developed, which differ in loading condition and crack positions:

1. *The wheelset model with the surface crack loaded only by the bending* — model of the investigated railway axle with the mounted wheels, where the crack growth is assumed from the outer surface in the critical position determined previously in section 5.1.
2. *The wheelset model with the surface crack loaded only by the press-fit* — the same as the previous model without considering the bending load but with nonlinear contact definition for accurate press-fit load stress field.
3. *The railway axle model with the surface crack loaded only by the residual stress* — the partial model of the investigated railway axle with surface crack, without modelling the wheels, loaded by the determinate residual stress field.
4. *The wheelset model with the internal crack loaded only by the bending* — the same as the first model, however, considering the internal crack.
5. *The wheelset model with the internal crack loaded only by the press-fit* — the same as the second model, however, considering the internal crack.
6. *The railway axle model with the internal crack loaded only by the residual stress* — the same as the third model, however, considering the internal crack.

The details of models with surface crack and obtained results are described further in the following text. Then, models with internal crack and their results are described.

### 7.2.1 The Investigated Railway Axle with the Surface Crack

Typical fatigue crack can initiate from the surface of the axle, see section 3.1. FEM investigation of the railway axle in section 5 shows the critical position where axial (critical) stress reaches its maximum value. In order to perform the RFL estimation in the damage-tolerant approach, total SIF (as well as static and dynamic components) as a function of the crack length needs to be known. Therefore, an investigation of the railway axle with a surface crack was performed while different loading conditions were considered. The whole railway wheelset is considered in FEM simulations as well as in section 5.

The railway wheelset model consists of the investigated railway axle and two corresponding railway wheels, one on the left side and one on the right side. The total length of investigated railway axle was 2180 mm, and the outer diameter of the axle body area and the wheel seat area were 168 mm and 200 mm, respectively. The hole inside the axle had a diameter of 70 mm. The crack is modelled directly as a part of the geometry [224]. The crack is situated at the surface in the critical position

near the wheel seat. As expected from the real axle failures, the crack growth direction is in the radial direction. The crack is modelled parametrically onto the externally imported model (created in the 3D modelling software based on the documentation provided by representatives of BONATRANS GROUP a.s.) of the railway wheelset, which means the crack distance from the wheel seat can be changed as well as the crack length and width. Different crack lengths from 1 mm up to 25 mm were initially considered.

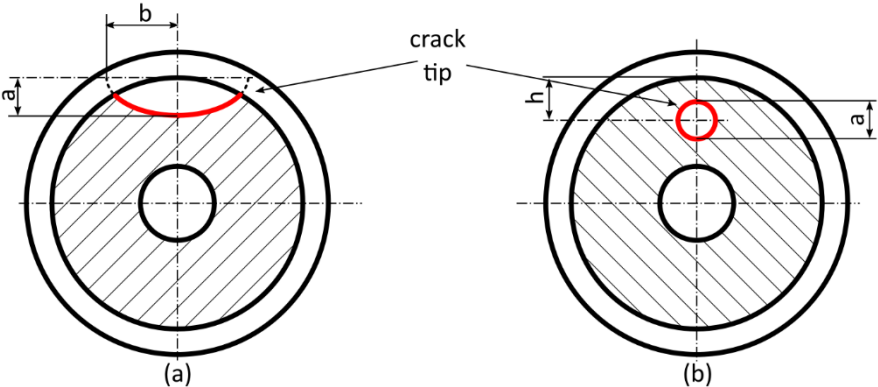


Figure 82 Schematic geometry of the surface (a) and the internal (b) cracks

The semi-elliptical crack shape was considered in the model, see Figure 82 (a). The minor ellipse axis (crack width) is determined according to the shape formula proposed by Náhlík et al. [222]. The crack growth was simulated by modelling the different crack lengths. For every crack length and every presented model, the SIFs  $K_I$  were determined along the whole crack front using the methods described in section 3.2.2. Only the one value of the SIF for the one crack length will be presented in the further text. One value is sufficient due to the optimized crack tip shape and due to practically identical results from the different SIF determination methods (see Figure 67 for method comparison). Optimized crack tip shape shows the constant value of the SIF for most of the crack tip length.

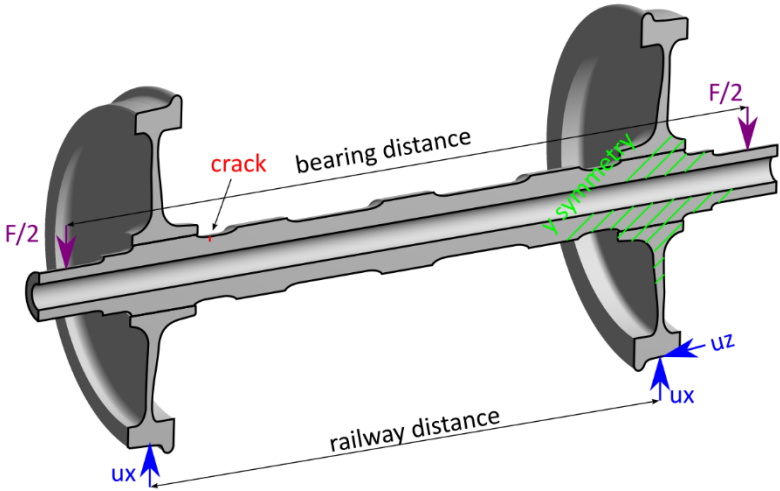
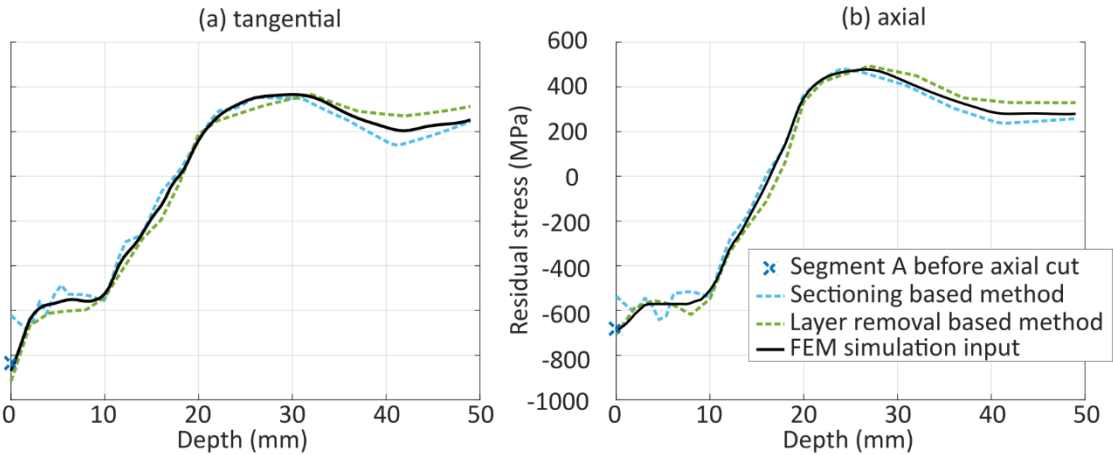


Figure 83 Schematic illustration of the boundary conditions

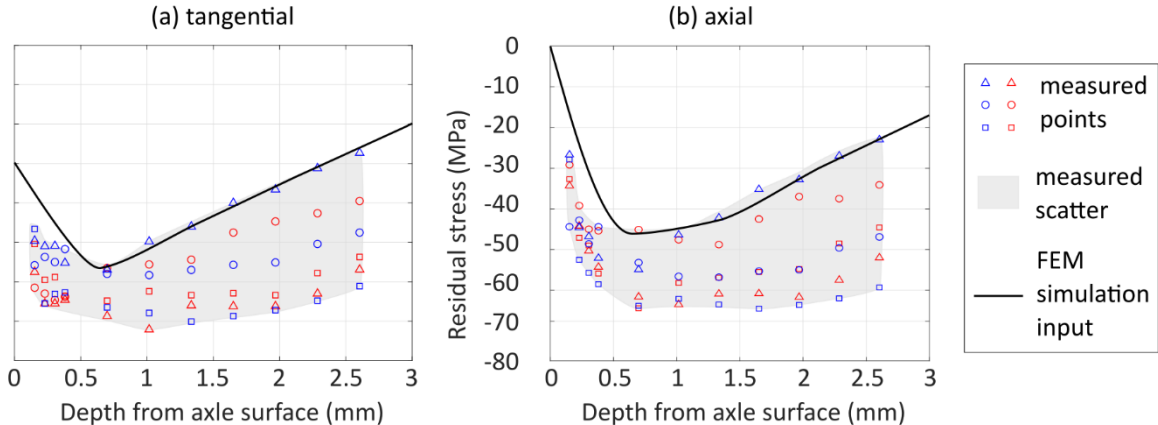
Figure 83 shows a summary of the boundary conditions. The advantage of the one possible symmetry was taken into account. Therefore, only one-half of the wheelset was modelled. Other symmetry planes are excluded due to the presence of the crack. The symmetrical boundary condition (Y direction) was defined on the plane of symmetry. Two nodes were used for the vertical

(X direction) degree of freedom restriction. Nodes are located at the outer diameter of the wheels at the symmetry plane. They are 1500 mm (rail spacing) far from each other, selected symmetrically in the axial direction (750 mm from the middle of the axle). For the axial (Z direction) degree of freedom restriction, the node where the vertical degree of freedom was restricted and is far from the crack position was used. For the axle loading, two nodes were used. Nodes are located at the axle's outer diameter at the symmetry plane. They are 2000 mm (bearing spacing) far from each other, selected symmetrically in the axial direction (1000 mm from the middle of the axle). The total applied force corresponds to the static load (dynamic coefficient  $k = 1$ ) from the loading spectrum.

Quadratic hexahedral elements were used to discretize most of the axle. Hexahedral elements were used in the vicinity of the crack too. The rest of the axle (the transition area between hexahedral elements around the crack and elements in the rest of the model) was discretized by the quadratic tetrahedra elements. Most of the elements were located near the crack due to the fine and regular mesh around the crack. The number of nodes moves from 1 500 000 up to 1 820 000 in dependence on the modelled crack length. The material for the axle was used as a linear elastic, isotropic defined by Young's modulus of 204 GPa and Poisson's ratio of 0.3. These values correspond to EA4T steel. Quadratic hexahedral elements only discretized the wheels. The material model of these parts was identical to axle material.



**Figure 84 Residual stress profile after induction hardening used for the SIF determination; (a) tangential stress, (b) axial stress**



**Figure 85 Residual stress profile after quenching used for the SIF determination; (a) tangential stress, (b) axial stress**

Linear contacts were defined between each wheel and the axle. This type of contact excludes any geometrical overlap between the axle and wheels. Therefore, it was used only for modelling bending load conditions. For the press-fit loading condition, force application was excluded, and the nonlinear frictional contact replaced linear contact with a friction coefficient of 0.6. The press-fit load was applied as the geometrical overlap of 0.3 mm between the axle and wheels.

The third loading condition for the investigated railway axle is residual stress. Due to the superposition principle, the effect of the residual stress on the crack growth can be determined by the separated model as well. As the residual stress determination process showed (see section 5.2), the discretization mesh must cover the stress gradient. Therefore, mesh requirements for the simulation of the residual stress field around the crack tip are high.

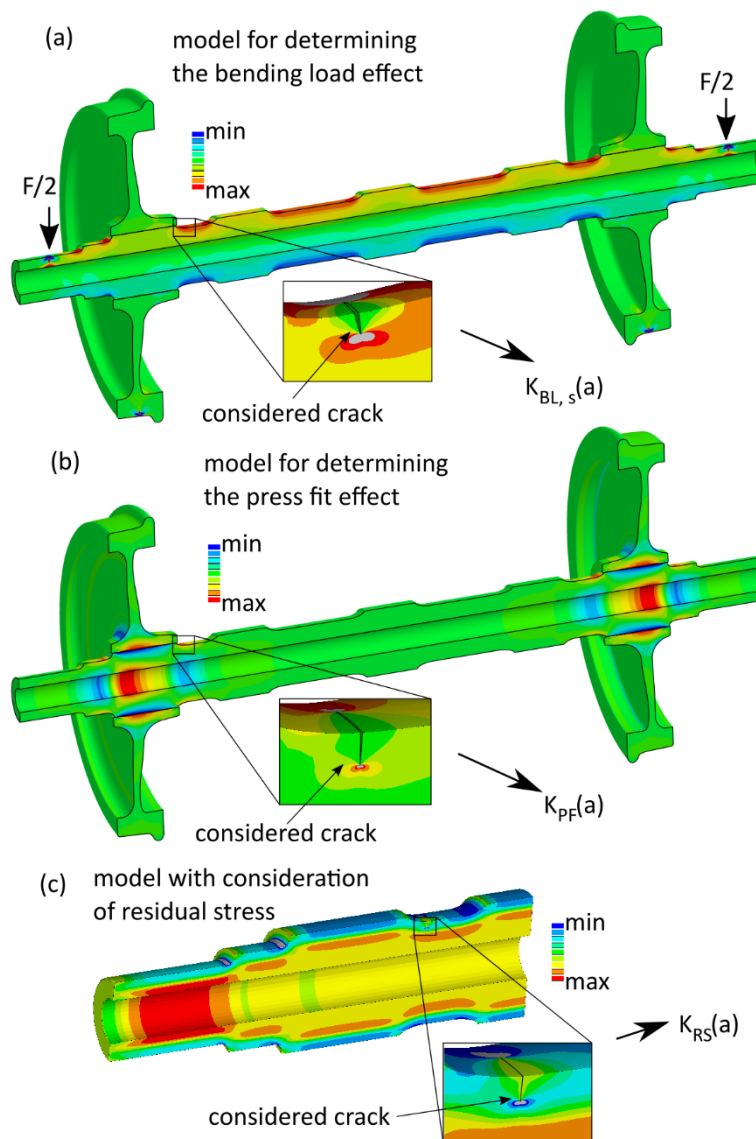
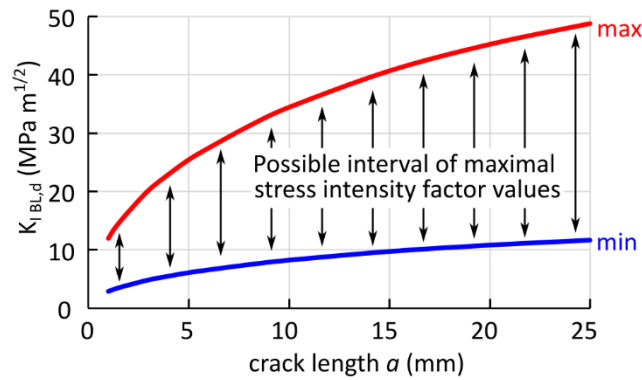


Figure 86 Axial stress results in different models with the surface crack



**Figure 87 Possible stress intensity factor range corresponding to different bending load amplitudes**

In order to preserve fine mesh around the crack tip and fine mesh for the residual stress field description, only shortened model of the axle without wheels was developed. The advantage of the one possible symmetry was retaken into account. The symmetry boundary condition (Y direction) was defined on the plane of symmetry. At the shortened end of the axle, the restriction of the axial degree of freedom (Z direction) was used. To prevent rigid body motion, at least one node in the vertical direction (X direction) must be restricted. Therefore, one node at the shortened end of the axle in the perpendicular plane to the symmetry plane was selected and used for the vertical degree of freedom restriction.

Quadratic hexahedral elements were used in the vicinity of the crack and in most of the model. Again, the quadratic tetrahedral elements were used to transition between the crack tip mesh and the rest of the mesh. The number of nodes moves near 2 500 000. EA4T steel material described above was used.

Loading of the axle by INISTATE command was executed. The residual stress profile was considered axisymmetrical and homogenous along the axial direction. Two residual stress profiles were considered in simulations. The first residual stress profile, see Figure 84, corresponds to the induction hardening surface treatment. The residual stress determination was shown in section 6. The second residual stress profile, see Figure 85, corresponds to the classic quenching surface treatment. Residual stress determination was performed in a similar way as for induction hardening. The semi-elliptical crack shape and different crack lengths were considered again. Crack lengths ranging from 1 mm up to 25 mm were considered again.

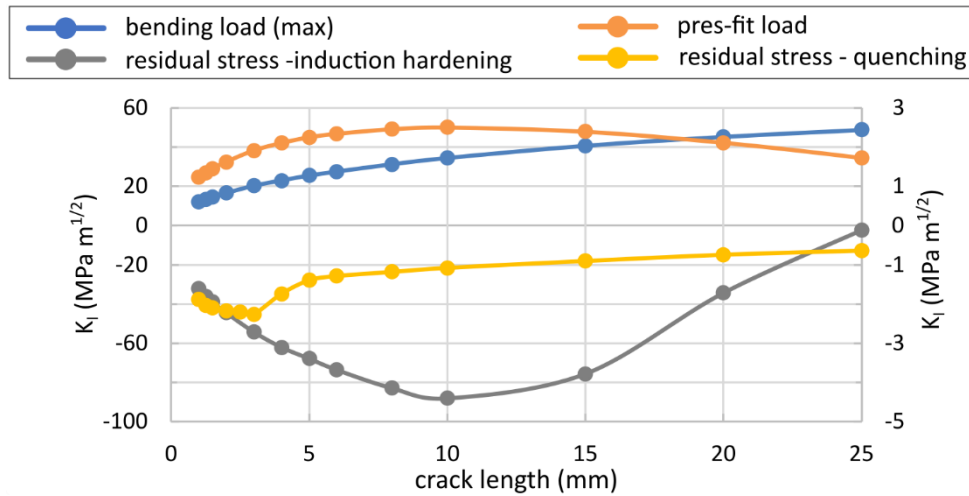
Figure 86 shows axial stress results due to the different loading conditions for one crack length. The assumption of LEFM allowed the use of the superposition principle. The separation of the three types of load led to the expression (40) of the total SIF  $K_{max}$  in the form:

$$K_{max}(a, t) = K_{BL,d}(a, t) + K_{PF}(a) + K_{RS}(a), \quad (40)$$

where  $K_{BL,d}$  is the SIF due to dynamic bending load (depending on crack length  $a$  and load spectrum),  $K_{PF}$  is the SIF due to press-fit load, and  $K_{RS}$  is the SIF corresponding to the residual stress load. A load spectrum describes the variable-amplitude loading caused by the train movement. Figure 87 shows the possible range of the  $K_{BL,d}$  due to the loading spectrum. The so-called dynamic coefficient  $k$  corresponds to the static load multiplication  $K_{BL,s}$  (due to the nominal vehicle weight). The dynamic bending load  $K_{BL,d}$  is given by:

$$K_{BL,d}(a, t) = k(t) \cdot K_{BL,s}(a), \quad (41)$$

where  $k$  is the dynamic coefficient and  $K_{B,s}$  is the SIF corresponding to the static bending load determined from the simulations.



**Figure 88 Stress intensity factor results for the considered surface crack lengths for different loading types**

Figure 88 shows determined SIF values for different crack lengths. Values corresponding to the bending load are shown for the maximum dynamic coefficient. SIF values from the bending load change during the train operation, influencing the amplitude of the SIF cycle. SIF values from the press-fit and residual stress act as a static loading during the train operation, influencing the mean value of the SIF cycle.

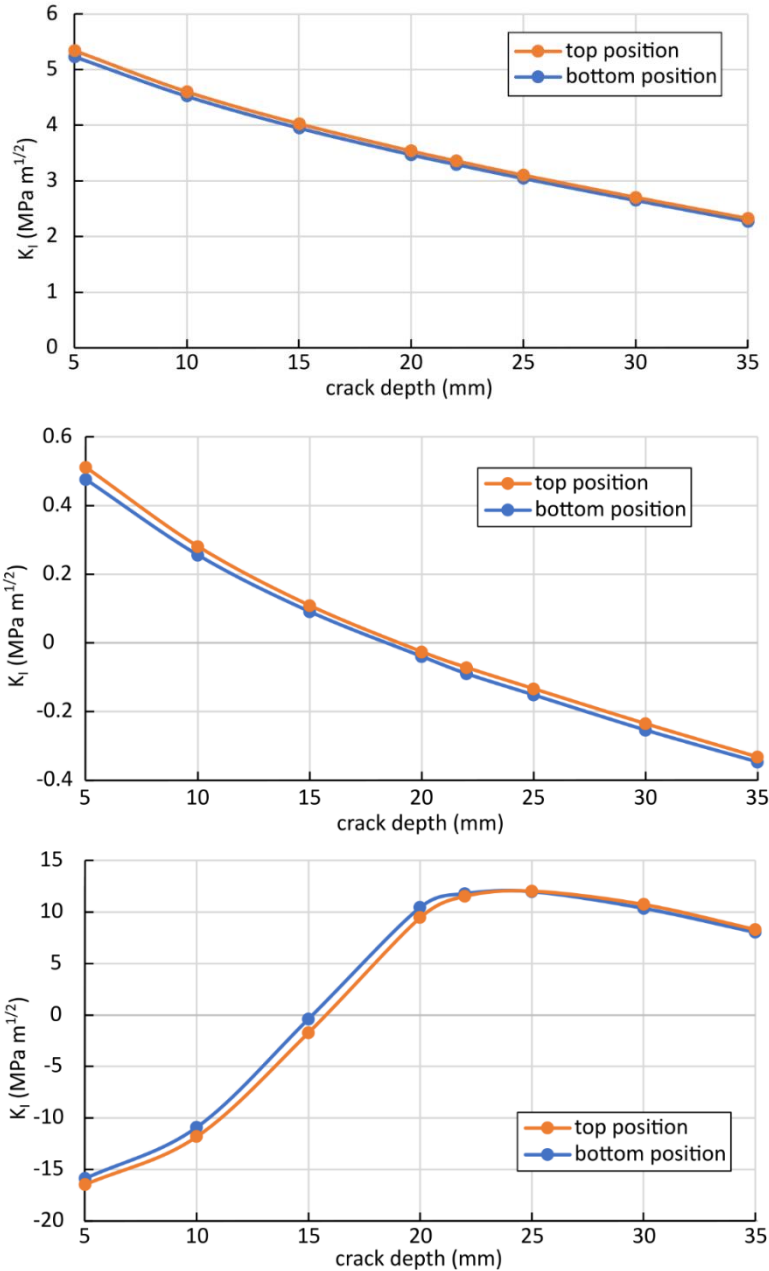
### 7.2.2 The Investigated Railway Axle with the Internal Crack

The SIF from induction hardening residual stress showed negative values in the whole range of the simulated crack lengths. From 1 up to the 10 mm crack length, the SIF decreases from -32 up to -88 MPa m<sup>1/2</sup>. After 10 mm crack length, the SIF increases up to -2 MPa m<sup>1/2</sup>. This means that the total SIF (summation of all three loading conditions; bending + press-fit + residual stress) is negative for most of the crack depths, and the crack should not propagate. Based on this result, a new critical position should be determined for the investigated railway axle. Determining residual stress after induction hardening shows a tensile peak deeper in the axle cross-section. Such tensile stress (residual stress influences the mean value of the loading stress) helps to initiate the crack from defects like inclusions. Therefore, the other three models with the internal crack (see Figure 82 (b)) were developed. The models with the surface crack were redesigned, and the internal crack was introduced in new models.

Material properties, discretization process, and boundary conditions were the same for each model (based on loading conditions) as before for the models with surface cracks. A circular crack shape was considered for the internal crack due to a lack of information about the actual crack shape. The crack length parameter  $a$  is equal to the crack diameter. The crack axial position was considered the same as the surface crack, 29.3 mm from the wheel seat. The depth of the crack was included as a variable to identify the critical position. The crack depth varies from 5 mm up to 35 mm with steps of 5 mm. An additional 22 mm crack depth was considered. First, only 1 mm crack length was considered. Then, a critical position was found, and different crack lengths from 1 mm up to 15 mm (diameters of cracks are 1 mm up to 15mm) were modelled. The SIF is not constant

through the crack front in this configuration. Therefore, values from the bottom and top positions will be presented.

Again, determination of the SIF for all three types of loading was performed. Figure 89 shows the results of the SIF for different loading conditions and different crack depths. The SIF caused by the bending load is getting low with the increasing crack depth, which corresponds to the stress field caused by the bending load, where the maximum stress occurs at the maximum radii. SIF also varies with crack tip position. Therefore, the results of the SIF caused by the bending load at the bottom position of the crack tip (see Figure 82) always show lower values than at the top position. A similar trend can be seen for the SIF results caused by press-fit loading. The press-fit load has a more substantial influence near the axle surface, and with increasing depth, its effect quickly vanishes. Therefore, SIF results move to near-zero values, and its effect is neglectable.



**Figure 89 Stress intensity factors for different crack depths for crack length 1 mm**

SIF values caused by residual stress loading vary enormously with increasing depth, corresponding to the residual stress distribution and gradients under the axle surface. Also, the results vary for different crack tip positions. However, in depth around 22 mm for 1 mm crack length, the maximum SIF position changes from the bottom to the top. Maximum values appear in the depth of 25 mm for both positions.

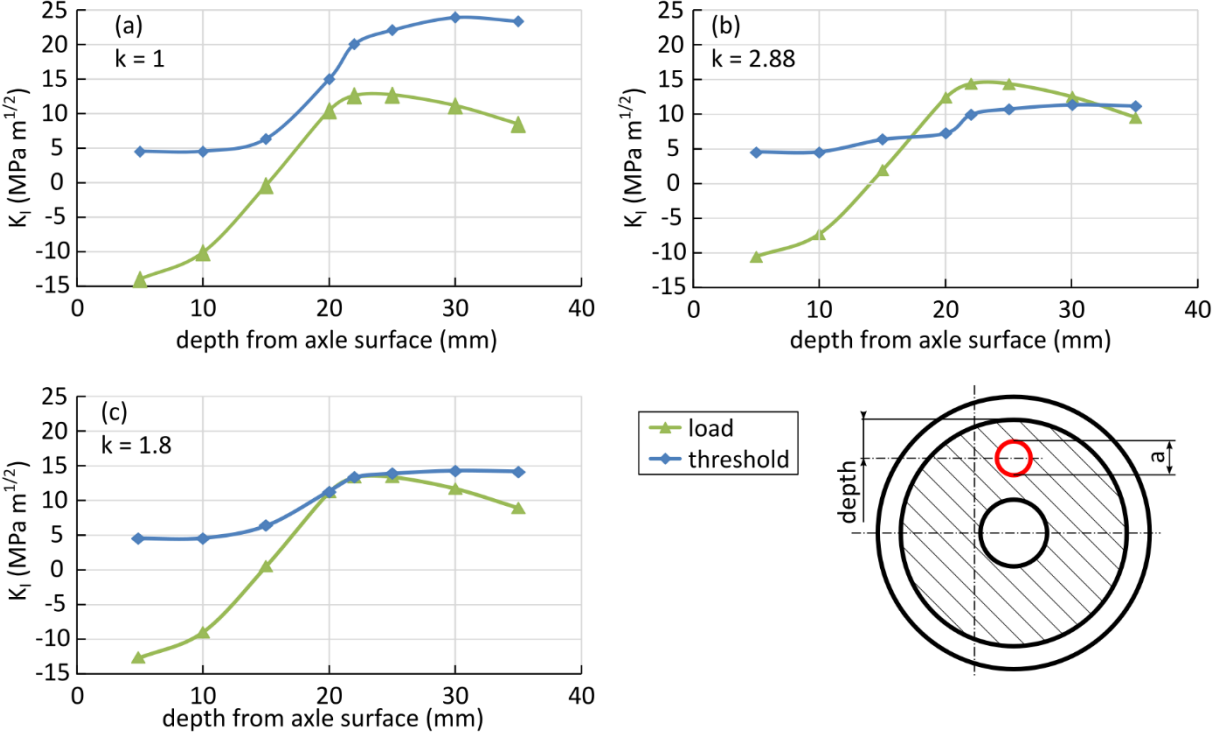


Figure 90 Crack propagation estimation for the dynamic coefficient (a)  $k = 1$  (b)  $k = 2.88$  (c)  $k = 1.8$

The critical position was estimated as a depth where maximum SIF  $K_{max}$  exceeds the threshold value first. Figure 90 compares the maximum SIF and the threshold values obtained for different crack depths for different dynamic coefficients. Figure 90 (a) ( $k = 1$  corresponds to the static load from the loading spectrum) shows that a crack 1 mm long will not propagate for any crack depth. However, Figure 90 (b) shows that the crack can propagate in multiple positions for the maximum load from the loading spectrum. Therefore, the crack depth where  $K_{max}$  for the lowest possible dynamic coefficient reaches the threshold is estimated as a critical position. The most significant number of loading cycles are counted as damaging cycles in this position. Figure 90 (c) shows  $K_{max}$  for the dynamic coefficient  $k = 1.8$ , where  $K_{max}$  just reaches threshold values. Critical depths are considered from 20 mm up to 25 mm range. The 20 mm crack depth is considered the most critical position due to the highest SIF range and is used in further internal crack simulations.

Figure 91 shows an example of the experimentally tested axles while observed internal crack growth. The critical crack depth estimation is in accordance with the experimentally obtained internal crack.

After the critical crack depth estimation, the SIF for the different crack lengths in the critical position was performed. Figure 92 shows determined SIFs for all three different loading types for different crack lengths of the internal crack in critical depth. The difference between the bottom and top positions increases with increasing crack length. For the bending load, SIF values have a similar trend as for the surface crack, with increasing crack length values increasing too. How much depends on the crack tip position (2 % up to 22 % for the crack lengths 1 mm and 15 mm, respectively).

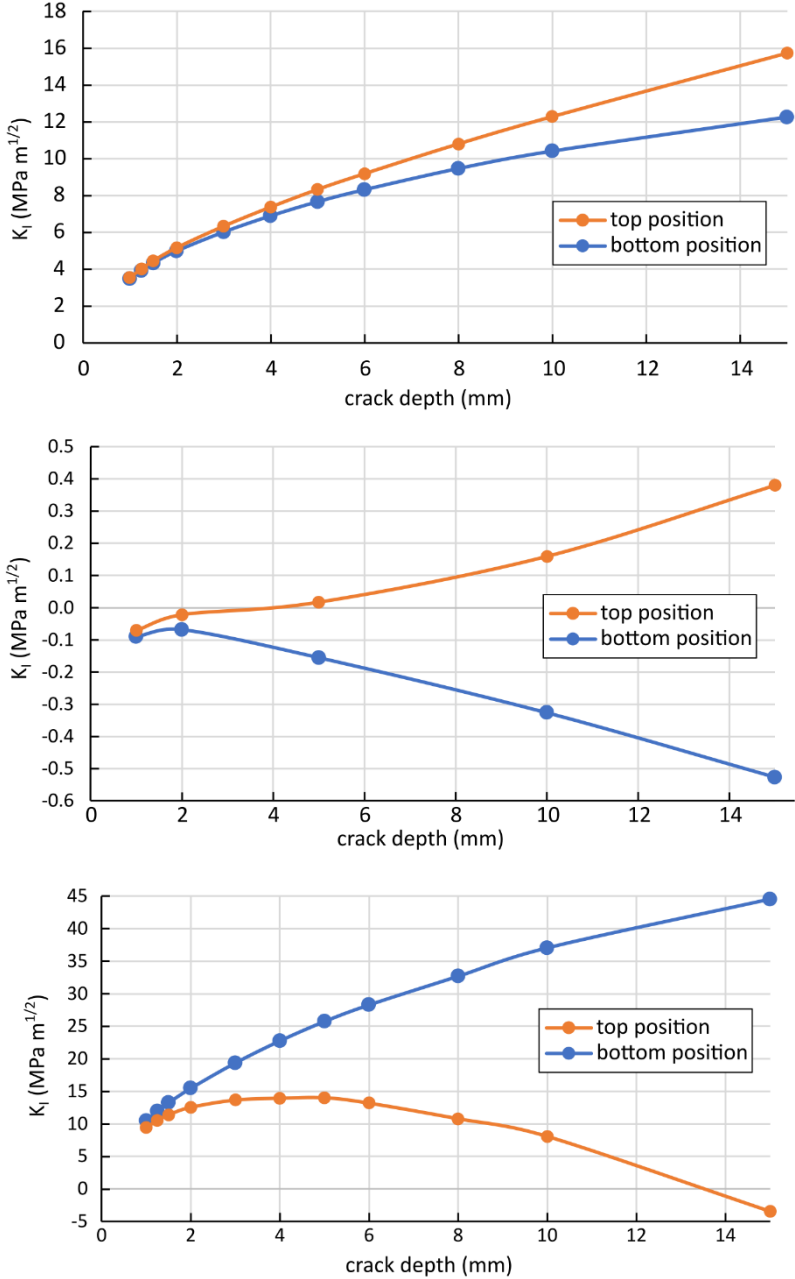
SIF values caused by the press-fit load are moving around zero. Therefore, less crack length spacing was considered. Again, SIF varies with the crack tip position (25 % up to 238 % for the crack lengths 1 mm and 15 mm, respectively). In most cases, the top crack tip position shows positive SIF values, while the bottom crack tip position shows negative values.



**Figure 91 Different railway axles fractured by the internal fatigue crack growth.**

SIF values caused by the residual stress load show different trends for the bottom and top positions (difference from 10 % up to 107 % for the crack lengths 1 mm and 15 mm, respectively). The bottom position values are increasing with increasing crack length. However, values are slightly increasing at the beginning for the top position, then after 5 mm of crack length, values decrease. This behaviour corresponds to the residual stress field. The bottom position is closer to the inner surface, where tensile residual stress occurs. The top position is closer to the compressive residual

stress; therefore, SIF values decrease for the longer cracks. Another important effect of the significant residual stress is the influence on the mean stress. A wide range of the residual stress (from -600 up to +400 MPa) causes a wide range in the asymmetry of the cycle R (from negative up to close to one) for both the surface crack and internal crack. This means a wide range of material data requirements.



**Figure 92 Stress intensity factors for different crack lengths**

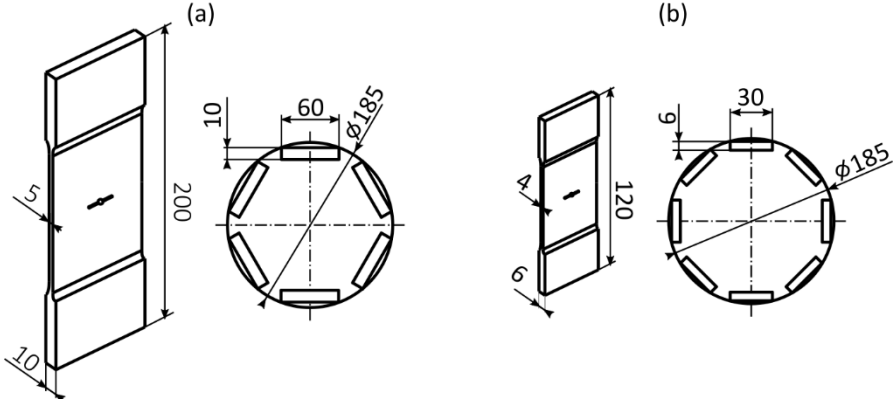
SIF determination for rolling bearing element and railway axle with residual stress were performed. For an internal crack in the bearing element, different SIF evaluation methods were compared to each other. SIFs behaviour during the loading cycle was described. SIFs determination functions were determined for all three loading modes while dimensions of the element and different crack lengths were considered. Different loading conditions were considered for the investigated railway axle. Bending load, press-fit and residual stress after the induction hardening and quenching

were considered. It was found that surface crack should not propagate. The summation of the SIFs shows negative values up to 15 mm crack length. Therefore, a new internal critical position was investigated. The critical position inside of the axle is influenced by the complicated stress field in the loaded axle. It was found that 20-25 mm crack (defect) depth is the most critical.

# 8 Material Data Determination

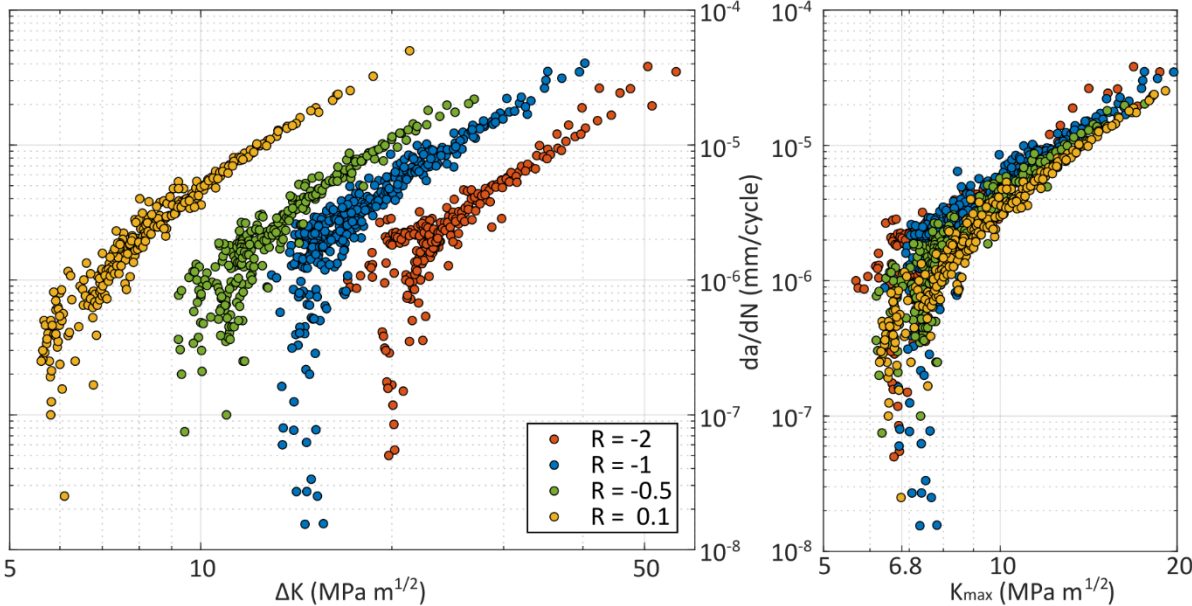
In order to perform the RFL estimation, the EA4T material data ( $v$ - $K$  curve) is still missing. Therefore, correct  $v$ - $K$  curve measurement is critical for the RFL estimation. The  $v$ - $K$  curve is estimated as a fit of the  $v$ - $K$  data points from measurement. The curve can be expressed in a different SIF form (e.g.  $\Delta K$  or  $K_{max}$ ).

The railway axle subjected to bending load only is subjected to the load ratio  $R = -1$ . However, with wheel press-fit and residual stress, which are not constant through the axle cross-section, the total load ratio  $R$  changes with the crack growth and load amplitude. Pokorný et al. [233] showed the effect of the press-fit load on the total load ratio  $R$ , where load ratio  $R$  can vary from  $R = 0.18$  for short crack lengths back to the  $R = -1$  for long crack lengths. The mean stress value (and load ratio  $R$ ) changes even more significant considering the residual stress load. Therefore, crack propagation tests must be carried out on multiple load ratios for the relevant  $v$ - $K$  curve.



**Figure 93 CCT specimen geometry and scheme of the cut-out area from cylindrical part of railway axle (a) standard heat-treated; (b) induction hardened**

For conservative estimation of RFL, it is worth considering  $v$ - $K$  curve, which were measured on the specimen with a lower in-plane constraint factor than the railway axle exhibits [234]. This requirement is fulfilled using the centre-crack tension (CCT) specimen, see Figure 93.



**Figure 94 Fatigue crack growth curves (a)  $v$ - $\Delta K$  (b)  $v$ - $K_{max}$**

The crack growth rate measurement took place in laboratory conditions with a temperature of 23 °C and relative humidity of 50%. The experiments were performed using the resonant testing machine Schenck with the maximal mean force of 30 kN and the maximal force range of ±30 kN. The testing frequency typically was in the range of 40–65 Hz, depending on the crack length, stress ratio, and load level. The  $v$ - $K$  data were determined according to the ASTM E647 standard. The fatigue cracks were initiated from sharp notches (two sides) of a total length of 7 mm, which were manufactured by the electro-discharge method. The force amplitude  $F_a = 23$  kN and the load ratio  $R = -1$  were applied for the crack initiation. After the crack length reached 1 mm at each side, a step-wise load shedding ( $\Delta K$ -decreasing) procedure was applied. Load reduction by 2.5–5% was done after every crack increment of 0.1–0.2 mm until the crack was arrested (propagation rate was lower than  $10^{-7}$  mm/cycle). The crack increments (lengths) were measured optically using two CCD cameras, uEye UI-2280SE-M-GL with objectives Lensagon CMFA2520ND with analogue output. The position of the cameras was measured by universal digital gauges Sylvac CO MFPM 25 with an accuracy of 0.01 mm. Typically, four specimens were tested for one load ratio  $R$ .

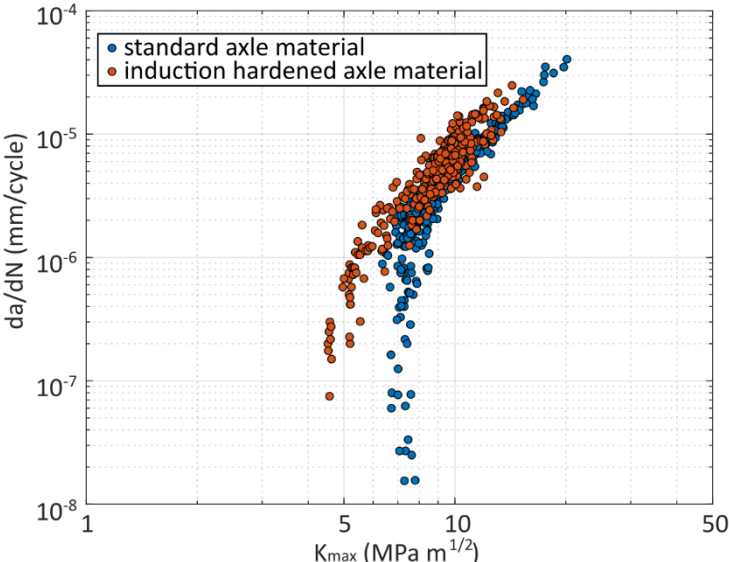


Figure 95 Comparison of  $v$ - $K_{max}$  curves for the classic EA4T material and the induction hardened material

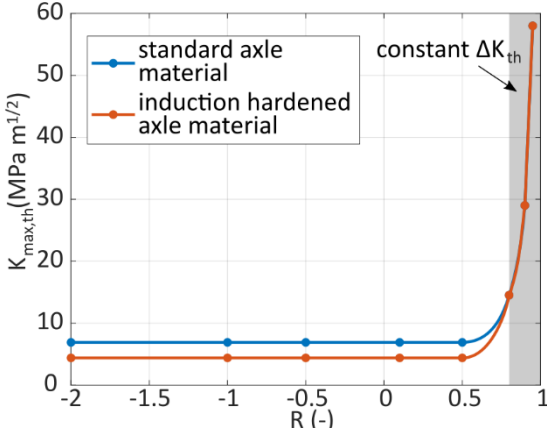


Figure 96  $K_{max, th}$  values for different load ratio  $R$

In order to determine corresponding  $v$ - $K$  data, the specimens manufacturing was considered according to Figure 93. Specimens were manufactured from the surface area of the standard axle. Due to specimen geometry and orientation, the unwanted release of the residual stress is expected. Figure 94 a) shows  $v$ - $\Delta K$  curves for different load ratios  $R$ . Náhlik et al. [222] and Pokorný et al. [233] showed that the  $K_{max}$  parameter could be effectively used for  $v$ - $K_{max}$  data description. Note that the  $K_{max}$  parameter was previously used in [235] and is commonly used for RFL estimation performed by the IPM CAS. Figure 94 b) shows the effect of the using  $K_{max}$  parameter for  $v$  dependence. Crack growth rates for different load ratios  $R$  overlap as the one. The threshold values are nearly constant in this range. This is a massive benefit for the further experimental determination of crack growth rate curves.

Specimens manufactured from the induction hardened axle (see Figure 93 b)) were smaller in order to manufacture specimens from the affected surface area of the railway axle. The width and thickness of the specimen were 30 mm and 4 mm, respectively. Figure 95 compares the standard EA4T  $v$ - $K_{max}$  curve with the induction hardened  $v$ - $K_{max}$  curve. Both were determined for the load ration  $R = -1$ . Induction hardened material shows a smaller threshold value  $K_{max,th} = 4.6 \text{ MPa}\cdot\text{m}^{1/2}$  against the threshold value of  $K_{max,th} = 6.8 \text{ MPa}\cdot\text{m}^{1/2}$  for the standard material. Both materials show very similar crack growth behaviour in the Paris region (region II in Figure 18).

Figure 96 shows the dependence of the threshold value  $K_{max,th}$  on different load ration  $R$ . In the case of the compressive residual stress, correct  $K_{max,th}$  is critical as a parameter that decides whether a given load amplitude will be contributing to crack growth or not.  $K_{max,th}$  parameter was also used in critical crack depth estimation for the internal crack.

## 9 Residual Fatigue Lifetime Estimation

After the necessary data determination in previous sections, this section finally shows the RFL estimation procedure considering the residual stress in the railway axle. As was mentioned previously, residual stress influences the mean value of the loading cycle. Therefore, some parameters still need to be defined to describe SIF functions fully. Each component of SIF is a function of the crack length  $a$ . The sum of press-fit and residual stress loads represents the mean SIF  $K_m$ :

$$K_m(a) = K_{PF}(a) + K_{RS}(a). \quad (42)$$

The amplitude of the total SIF is represented by the dynamic bending load  $K_{B,d}$ :

$$K_a(a, t) = K_{B,d}(a, t). \quad (43)$$

The maximum SIF was already defined by (40). The following equation gives the minimum during the load cycle:

$$K_{min}(a, t) = K_{PF}(a) + K_{RS}(a) - K_{B,d}(a, t), \quad (44)$$

Due to variable bending load and non-zero mean load, the load ratio is also variable. The load ratio  $R$  is expressed as:

$$R(a, t) = \frac{K_{min}(a, t)}{K_{max}(a, t)} = \frac{K_{PF}(a) + K_{RS}(a) - K_{B,d}(a, t)}{K_{PF}(a) + K_{RS}(a) + K_{B,d}(a, t)}. \quad (45)$$

The modified NASGRO equation describes the experimental data, depicted in Figure 94 (b) and Figure 95:

$$\frac{da}{dN} \cong \frac{\Delta a}{\Delta N} = C^* (K_{max})^{n^*} \left(1 - \frac{K_{max,th}}{K_{max}}\right)^{p^*}, \quad (46)$$

where  $C^*$ ,  $n^*$ , and  $p^*$  are material constants with the same meaning as the classic NASGRO approach; however, their values are generally different.  $K_{max}$  as a controlling parameter is suitable where low load ratios occur. Because the crack closure values are very similar in this range of load ratios. The used material constants for NASGRO fit of the EA4T steel were according to Table 4.

**Table 4 NASGRO fitting constants summary**

Material	$C^*$	$n^*$	$p^*$	$K_{max,th}$
Standard EA4T	$1.8 \times 10^{-11}$	2.6	0.25	6.8
Induction hardened EA4T	$1.8 \times 10^{-11}$	2.7	0.35	4.6

The RFL estimation was calculated for initial crack length  $a_0$  up to the critical length  $a_f$ . The increment of the crack length is calculated step by step by the equation:

$$\Delta a = C^* (K_{max})^{n^*} \left(1 - \frac{K_{max,th}}{K_{max}}\right)^{p^*} \Delta N. \quad (47)$$

The crack increment is zero for the loading cycles where  $K_{max} \leq K_{max,th}$ . Calculation runs until the total calculated crack length reaches critical value  $a_{tot} > a_f$ . Then the total number of cycles is estimated. In this case, the calculation runs in loops, where one loop corresponds to 1000 km of train operation, see representative load spectrum in Figure 35. The final number of loops equals the kilometres in service times 1000. The loop starts with the highest load amplitudes up to the lowest ones. Note that this kind of calculation does not consider any additional effects like the overload cycles influence. This simplification makes the estimation conservative.

The other type of axle (as presented in previous sections for the critical position and SIF determination) was considered for the RFL estimation. This other axle was also tested in a full-scale fatigue test, see the next section 9.1.

The RFL was considered as crack growth from initial crack length up to the crack length  $a_f$  25 mm. Propagation of the cracks longer than 25 mm is very fast, and therefore, it has minimal impact on the estimated RFL [222]. Multiple initial crack lengths  $a_0$  2 mm, 3 mm, 5 mm, and 10 mm were considered to evaluate their impact on RFL. Four different loading combinations were considered for the estimation:

1. *Loading only by the bending load without press-fit and residual stress load (BL only)* – loading conditions considers only load ratio  $R = -1$  with variable load amplitudes (defined by loading spectrum, see Figure 35).
2. *Loading by the bending and press-fit load without residual stress load (no RS)* – loading by variable load amplitudes with non-zero mean stress due to press-fit. It means variable load ratio  $R$ .
3. *Loading by the bending and press-fit load considering residual stress load caused by quenching corresponding to the standard state of EA4T steel (RS – quench.)* – loading by variable load amplitudes with variable load ratio. Mean load is the superposition of press-fit load and residual stress load.
4. *Loading by the bending and press-fit load considering residual stress load caused by induction hardening (RS – ind. hard.)* – loading by variable load amplitudes with variable load ratio. Mean load is the superposition of press-fit load and residual stress load.

The first case, loading only by the bending load, is, in reality, impossible. However, it is necessary to demonstrate the mean stress effect of the RFL estimation.

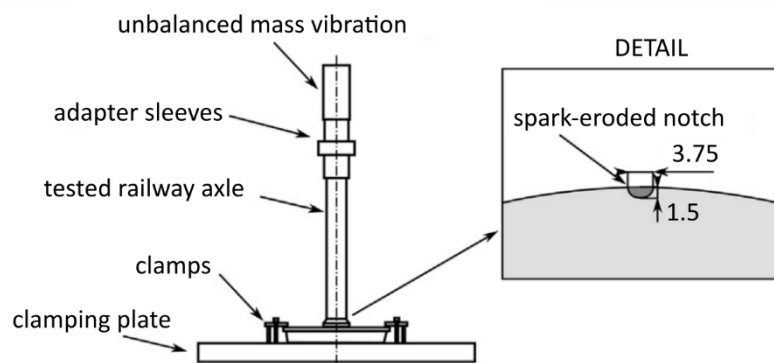
**Table 5 Estimated residual fatigue lifetime in thousands of kilometres (kkm) for the crack growth from  $a_0$  up to 25 mm (DNP - do not propagate)**

Loading conditions	Initial crack length $a_0$			
	2 mm	3 mm	5 mm	10 mm
BL only	17 444	506	138	52
no RS	85	35	16	10
RS - quench.	32 451	154	33	13
RS - ind. hard.	DNP	DNP	DNP	DNP

Table 5 shows estimated RFL in kilometres for different loading conditions and initial crack lengths. As expected, the lowest RFL (85 000 km for  $a_0 = 2$  mm) was estimated for the second case considering the positive mean stress due to the press-fit load only. The effect of the mean stress is more pronounced for the shortest considered initial crack lengths. Therefore, estimations for  $a_0 = 10$  mm for the first three cases (BL only, no RS and RS – quench.) are very similar to each other. On the other hand,  $a_0 = 2$  mm estimation shows a higher mileage difference. It is caused by the residual stress strong influence due to quenching. Quenching causes a compressive residual stress field in the vicinity of the surface; however, its effect fades after a few millimetres of the depth. RFL estimation for the induction hardened railway axle shows unlimited mileage. Due to the enormously high compressive residual stress, the crack does not propagate (DNP), not even from the longest considered initial crack lengths.

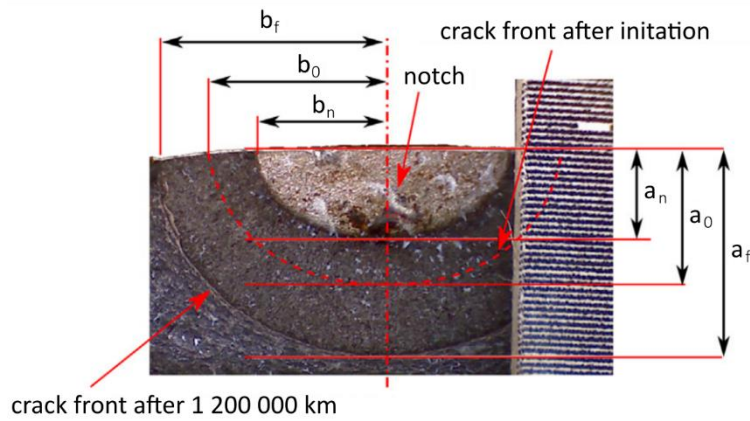
### 9.1 Experimental Validation of the Estimated Residual Fatigue Lifetime

The full-scale experiments were performed to validate the RFL estimation (considering the influence of the residual stress). Experiments were performed in BONATRANS GROUP a.s laboratories. Specimens according to the real axle were manufactured (see Figure 97). The spark erosion method manufactured a semi-elliptical artificial notch in the predicted critical position of the railway axle (the position considered for the SIF determination). The dimensions of the artificial notch were width ( $2b_n$ ) 3.75 mm and depth ( $a_n$ ) 1.5 mm. The axle specimen was press-fitted into the clamped testing wheel. The load was applied by the operation of the unbalanced mass vibration generator. Fatigue pre-crack was initiated from the artificial notch by application of the highest load amplitude from the load spectrum. Crack width was measured optically at the surface of the axle (dimension  $b$  was measured). During the experiment, the crack length  $a$  was derived from the crack width  $b$ . It was considered that the ratio between  $a/b = 1.5/1.875 = 0.8$  was constant during the whole experiment. After the final specimen break, the real crack shape was evaluated.



**Figure 97 Scheme of full-scale experiment**

Three axle specimens were tested after the axle's standard heat treatment (quenched and tempered). The pre-cracking process stopped after the total width reached approx. 6.25 mm (approx. 2.5 mm total depth/crack length). After pre-cracking, the load spectrum (with variable amplitude) was applied. The continuous decreasing sequence (the load amplitudes of the applied spectrum were gradually varied from the highest value to the lowest one) was considered because the resonant testing mechanism is highly limited with the step change in the loading. One experimental sequence of load amplitudes corresponded to 100 000 km. This sequence with load amplitudes in descending order was applied 12× to apply load cycling corresponding to 1 200 000 km of train operation.



**Figure 98 Fracture surface after the experiment**

After applying such mileage, the axle specimen was cut to investigate the fracture surface and evaluate the crack front shape. Figure 98 shows the fracture surface with the marked artificial notch, crack front shape after the pre-cracking, and final crack front shape. Subscripts  $n$ ,  $0$ , and  $f$  refer to the notch dimensions, initial crack dimensions, and final crack dimensions, respectively.

With known real crack lengths, real crack shapes and known applied mileage, experiments were modelled. RFL estimations for all three tested axles were performed. Table 6 summarizes results from the three tested axle specimens with estimated RFLs. The estimated RFL is compared for the cases considering residual stress and without residual stress consideration. There is a nice match between the estimated and applied mileage. Estimation is on the conservative side for every tested specimen. Such conservatism is expected and desired since several conservative considerations were made during the estimation (conservative envelope of the measured residual stress, conservative envelope of measured data, no crack retardation effects, etc.). Table 6 shows that without the residual stress consideration in the RFL estimation, the resultant mileage is lower by one order and even further from the applied mileage. Therefore, consideration of the residual stress is necessary to obtain meaningful RFL estimation.

**Table 6 Experimental and estimated residual fatigue lifetime [99]**

axle number	initial crack length $a_0$ (mm)	final crack length $a_f$ (mm)	tested distance (kkm)	estimated distance (RS - quench.) (kkm)	estimated distance (no RS) (kkm)
1	2.28	3.05	1 200	185	26
2	2.08	2.70	1 200	497	34
3	2.20	3.00	1 200	217	31

Some experiments focused on the induction-hardened axles as well. Experiments followed the same procedure, setup, and notch parameters described for the standard axles. Based on the gathered numerical results (see Table 5), it was expected that a higher load than the maximum load from the service load spectrum would be needed for the crack initiation and growth. Therefore, cyclic loading was applied with the value corresponding to the nominal stress amplitude of 200 MPa (the dynamic coefficient  $k = 5.2$ ). This value is much higher than the maximum load in the load spectrum. Nevertheless, no crack propagation occurred after the application of  $5 \times 10^6$  cycles. Therefore, the load amplitude was further increased to 280 MPa for  $10^7$  cycles and 300 MPa

for  $10^7$  cycles. Even a two-fold increase in the load amplitude did not lead to crack propagation from the initial notch. Finally, fatigue crack propagation was achieved after  $1.1 \times 10^6$  cycles at the nominal stress level of 340 MPa. Such load level corresponds to the dynamic coefficient  $k = 8.8$  (i.e.,  $8.8 \times$  higher than the static load case). The test was terminated due to the excessive load of the experimental stand. The experiment confirmed that applying the standard load spectrum leads to no fatigue crack initiation and propagation in the case of induction-hardened axles with considered surface cracks.

## 10 The Stochastic Residual Fatigue Lifetime Estimation

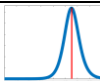
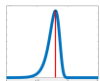
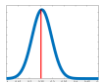
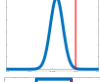

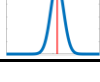
Classic (deterministic) RFL estimation is the commonly used approach in the damage tolerant design approach. However, such an approach averages or fits many variables into one value. Such variables are then used in the RFL estimation. This kind of approach (deterministic) results in one value as a result of the RFL estimation.

Many input variables are stochastic in their nature. Therefore, using the deterministic approach can be misleading (too conservative or not conservative at all) in some cases. The effort of the design engineers is to predict lifetime as accurately as possible and still be conservative. Therefore, stochastic RFL estimation can be helpful in order to predict the variability of the possible outcome. Some work has been done in stochastic railway axle RFL prediction in the past [72], [236]–[238].

In this work, the procedure described in Figure 99 has been developed at the IPM CAS. The developed procedure uses Bayesian techniques [239] for variable parameters description. Input variables are generated within specified limits (limits are set manually at the very beginning) first. Limits are based on the measured range or in the form of some percentage error. Then, residual mileage is estimated as described in the previous 9. section. The various sources of uncertainty, including variations in material properties, loading, and geometry, should be considered. The considered sources of uncertainty in this work were:

1. *Material properties* – the measured scattering of the obtained  $v$ - $K$  curve. Source material data was obtained during the years at the IPM CAS.
2. *Loading conditions* – the statistical nature of the loading condition fluctuations experienced during the actual working conditions of trains. Source data are based on blueprints of the railway wheelset (for press-fit) and scatter obtained during the residual stress measurement.
3. *Numerical uncertainty* – inaccuracy of the used numerical SIF determination. The main point is obtained from Giannella [72], where the author performed the same SIF determination using different numerical methods.

**Table 7 Considered uncertainties**

Uncertainty	Distribution	Probability density function	Expected value	Standard deviation	Deterministic value
$K_{max, th}$ (MPa*m <sup>1/2</sup> )	Log-logistic		6.8	1.029	6.8
$C^*$ (m/cycle)	General extreme value		1.8e-11	0.790935e-12	1.8e-11
$p^*$ (-)	Rician		0.25	0.0427	0.25
Press-fit (mm)	Normal		0.258997	0.04556	0.3
Axial residual stress – min. peak value (MPa)	Uniform		-55	10	-45
Numerical (%)	Normal		100	0.01667	100

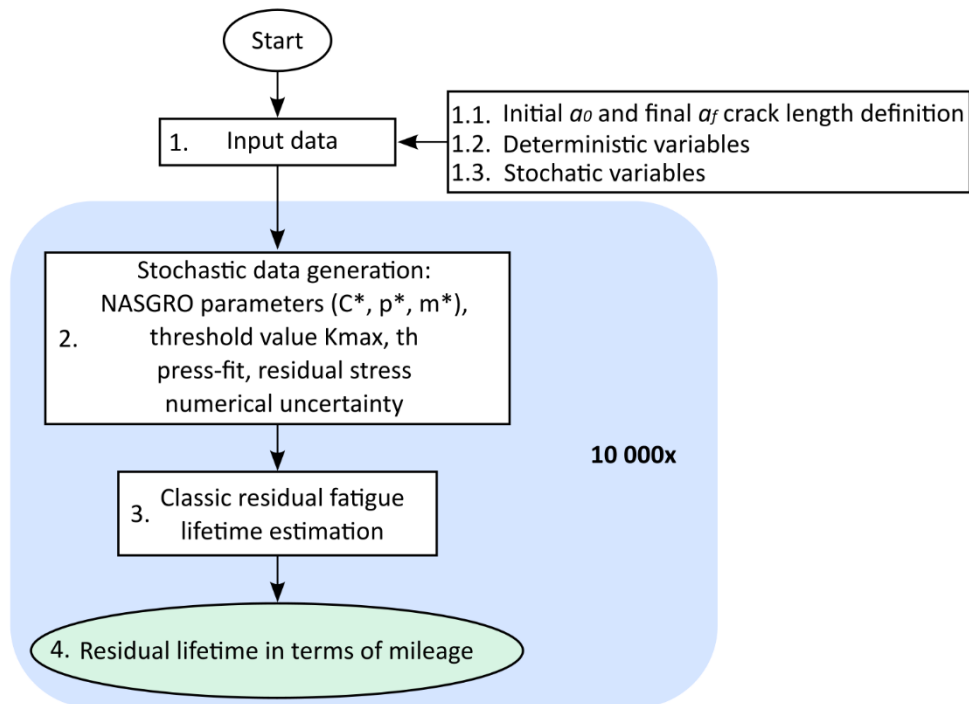


Figure 99 Flow chart of the stochastic lifetime estimation procedure

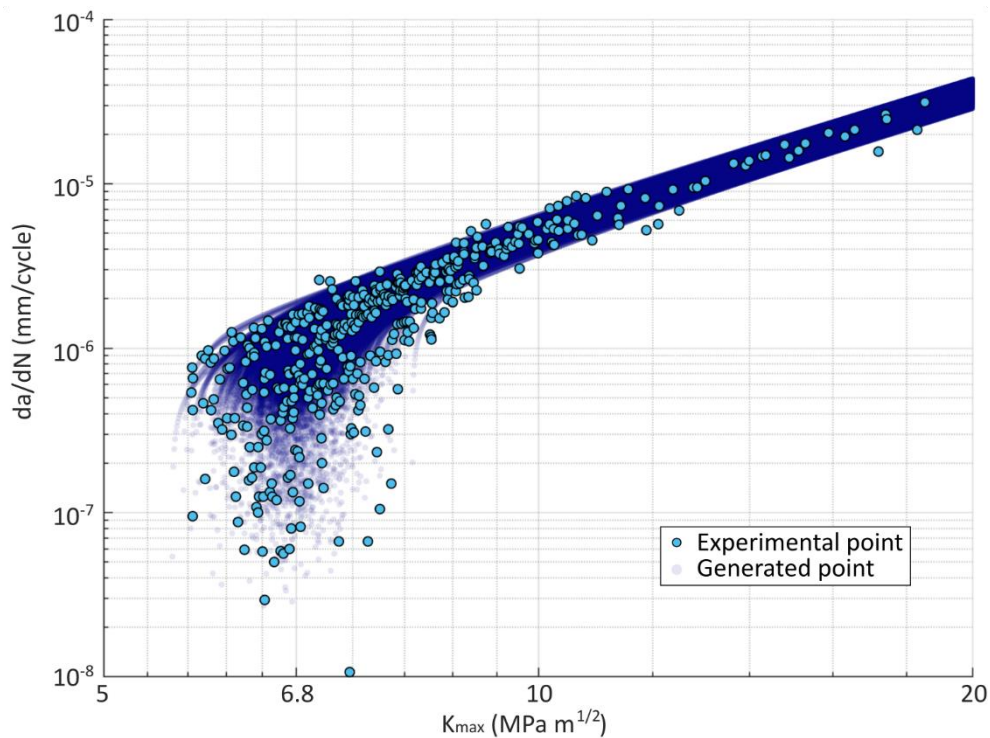


Figure 100 v-K data used for lifetime estimation, experimental points, and generated curves

Considered uncertainties with their distributions are summarised in Table 7. The first considered uncertainty was from the material data scatter. The  $v$ - $K_{max}$  curve is fully characterized by  $K_{max, th}$ ,  $C^*$ ,  $p^*$  and  $n^*$ . The distribution of  $K_{max, th}$ ,  $C^*$ , and  $p^*$  variables were fitted according to measured data scatter. The  $n^*$  parameter was considered constant. This parameter corresponds to the tilt angle in the Paris region. Figure 100 shows generated curves in comparison with measured experimental data. One can see that generated curves are in experimental data scatter.

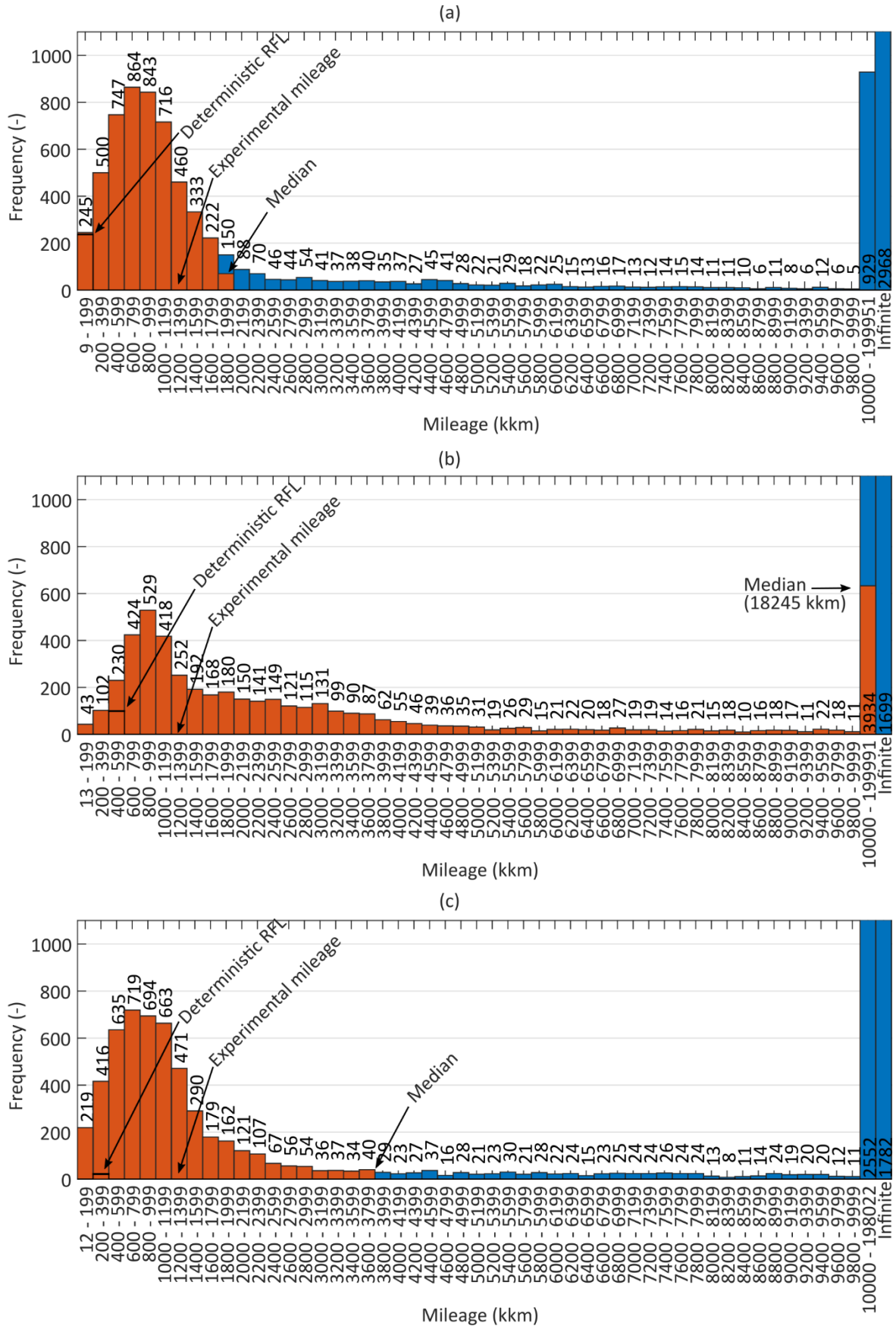


Figure 101 RFL estimation distribution for all three experimentally tested axles with consideration of all uncertainties; (a) axle 1, (b) axle 2, and (c) axle 3

The second considered uncertainty lies in loading conditions. Press-fit uncertainty is in the range of defined geometrical tolerances. The press-fit loading varies from the lowest possible to the highest possible overlap between the axle and wheel. The residual stress uncertainty lies in the measurement itself. This uncertainty considers the scattering of the residual stress measured points (see Figure 85). The residual stress is described as a function of the present residual stress against the axle depth under the surface. Therefore, the residual stress is generated in the form of a function characterized by a minimum peak value. The numerical SIF determination causes the third and last considered uncertainty. Numerical simulation results are generally influenced by the quality of the used mesh and the accuracy of the applied boundary conditions. Giannella [72] performed the same numerical simulation by different numerical methods and obtained different results. Therefore, some uncertainty in determined SIF is appropriate. Variability of  $\pm 5\%$  for the determined SIF is selected as appropriate for numerical uncertainty.

In the previous section, three different axles were experimentally tested. These three axles were considered again, and stochastic RFL estimations were performed considering the mentioned uncertainties. For one axle, 10 000 RFL estimations were performed. Figure 101 shows a histogram of obtained RFL estimations. Obtained results show a wide range of the estimated mileage. Obtained mileages were sorted into 50 groups by 200 kkm range, except for three groups. The first group is in the range from minimum estimated mileage up to 199 kkm. The last group contains estimations where crack does not propagate (infinite mileage). Furthermore, the penultimate group contains estimations from 10 kkm up to the maximum obtained mileage (excluding infinite mileage). This group was formed because a wide range of mileages was achieved. In order to make the histogram readable, the higher mileage groups with low frequencies were merged into one group.

**Table 8 Summary of the deterministic and stochastic residual fatigue lifetime estimation with the experimentally tested mileage**

axle number	tested mileage (kkm)	deterministic estimated mileage (kkm)	the most numerous group (kkm)	frequency of the most numerous group (-)	the second most numerous group (kkm)	frequency of the second most numerous group (-)
1	1 200	185	600 – 799	864	800-999	843
2	1 200	497	800 – 999	529	600 – 799	424
3	1 200	217	600 – 799	719	800 – 999	694

Table 8 summarizes obtained results from the deterministic and stochastic RFL estimation. For all three axles, the mode value of estimated RFLs lies for non-propagating cracks (infinite mileage in Figure 101). If non-propagating cracks are excluded mode value of estimated RFL is higher than the deterministic RFL estimation for all three cases. This means that previous deterministic RFL estimations were performed conservatively. If the mode value of the estimated RFL is compared with experimentally applied mileage, the mode value is lower than the applied mileage for all three cases. This can mean that deterministic RFL estimation is not too conservative. However, one experiment for each axle is not enough to compare real experimental scatter. Therefore, more experimental data are needed to compare stochastic estimations with experimental data meaningfully.

Even without more experiments, the mode value of stochastic RFL estimation can be considered conservative compared to the experiment. It is caused by not considering of the loading history

and retardation effects. Applying the cycles that do not contribute to the crack propagation, an oxidic layer is formed on the crack faces [240]. Such an oxidic layer raises the threshold value for further crack propagation. Therefore, for the short crack, where most loading cycles do not contribute to the crack growth, the threshold value is higher than the conventional one. Overloading cycles have a similar effect. After applying the overload cycle, the crack growth rate is affected, and the plastic zone around the crack tip becomes larger, slowing down the crack propagation. Omitting these effects results in a conservative RFL estimate.

## 11 Conclusions

The presented work was focused on the determination of the residual fatigue life of components with residual stresses. A hardened railway axle was used as an example where the developed procedures find practical application. The work was created under the deep railway axle research ongoing at the Institute of Physics of Materials Cech Academy of Sciences in cooperation with BONATRANS GROUP a.s. company. The main part of the work deals with developing a new affordable methodology for the residual stress determination in sizable components like railway axles. The new methodology is applied twice on the same railway axle, and the influence of the determined residual stress is implemented into the residual fatigue lifetime estimation procedure developed at the IPM CAS. The work further discusses the other processes of the railway axle analysis to maintain the overall clarity and show the complete analysis's complexity. In addition to determining residual stress, the railway axle analysis includes critical position determination and stress intensity factor determination for the crack in the critical position. The finite element simulations provide both. Necessary material data for residual fatigue lifetime estimation were obtained experimentally. The experimental verification of residual fatigue lifetime estimation was performed with success. In order to show the effect of the scatter in loading and material data, the stochastic residual fatigue lifetime estimations were performed.

Eight main aims have been set in the present work. The individual aims and their fulfilment are summarised in the following text.

### *1. Review of literature for estimation of residual fatigue lifetime.*

The literature review showed the ability of fracture mechanics procedures to respond to the stated objectives. The basics of fracture mechanics are presented at the very beginning of the work. The linear elastic fracture mechanics was used in work. Two approaches can be used in terms of the linear elastic fracture mechanics: energy release rate or stress intensity factor approach. Work uses the stress intensity factor approach. Residual fatigue lifetime can be estimated by integrating the crack growth rate curve in terms of the stress intensity factor range. Different formulas can describe this dependence. A complex NASGRO approach was used in this doctoral thesis.

In this work, the railway axle is used as representative of the sizable components. The damage-tolerant approach is widely used in the industry for railway axle design. However, the simplified model of the bent plate with the elliptical surface crack is typically used for the residual fatigue lifetime estimation of the railway axle. Another possibility used in the industry is the usage of specialized software. Implemented software procedures usually use analytical functions in order to perform residual fatigue lifetime estimation. The accuracy of the analytical solution can often be poor, and the fact that the error of the estimate provided is unknown is particularly dangerous.

Note that this work used numerical modelling of the whole railway wheelset with the crack.

### *2. Review of literature for determination of residual stress in engineering components.*

The literature review describes the origin and length scale characterization of the residual stress. During the surface treatment of the component, non-uniform plastic deformation or material phase change causes residual stress. Type I (macroscopic), Type II (microscopic on the scale of the grains), and Type III (microscopic on the scale of one grain) residual stress are generally present

in the component. Residual fatigue lifetime is mainly influenced by the Type I residual stress. The macroscopic residual stress is mostly measured by the relaxation or diffraction methods (some other methods exist like magnetic, ultrasonic, etc.). Relaxation methods are based on the measurement of deformation after the release of residual stress; therefore, they are destructive in general. Diffraction methods measure crystal inter-planar dimensions. They are non-destructive in general; however, their main disadvantage is the shallow depth at which they are able to detect residual stresses.

### *3. Finding of methodology and procedures for determination of residual stress in sizeable components.*

Not many methods permit the residual stress measurement penetration of more than tens of millimetres (inside the sizeable component). Diffraction methods are dependent on the source power and the radiation type used. Neutron diffraction can be used in order to penetrate higher depths; however, there are only several laboratories capable of such measurement. Measurements at greater depths or for bulkier and heavier bodies are not possible. From the relaxation methods, the layer-removing or sectioning method can penetrate through the depth. However, deformation must be recorded during stress relaxation, which is time-consuming and sometimes challenging to perform. The crack compliance method seems possible to use from the relaxation methods. However, its accuracy decreases with the increasing depth of the measurement. The contour method or deep-hole drilling can measure residual stress in higher depths from the new-age methods. However, both methods require specific adjusted equipment, which is expensive and requires specialist technician training.

In conclusion of this part of the work, it can be stated that in the case of bulkier and heavier components, it is basically not possible to use any known experimental equipment, and it is necessary to develop new procedures that will combine experimental measurements with numerical estimates that will allow the determination of residual stresses even at greater depths in the case of sizeable and heavy components.

### *4. Creation or modification of existing methodology for determination of residual stress in sizeable components.*

Because no suitable and affordable residual stress measurement method has been found, a new custom methodology was developed. This methodology uses the experimental measurement of the surface residual stress by X-ray diffraction in combination with numerical simulations. Both types of equipment are commonly used in industry. The developed methodology includes a suitable specimen design in order to maintain the residual stress in the specimen so that it can be measured at the surface. In the case of the railway axle, it means one cylindrical specimen or a combination of two specimens (one with axial cut and the second with radial cut). The methodology was applied twice on the one railway axle after the induction hardening surface treatment.

A cylindrical specimen was used by the Layer-Removal-Based method. Measurement of the residual stress includes repeated layer removal from the surface of the cylinder specimen and measurement of the residual stress on the newly created surface. Layer removal and measurement are repeated until no residual stress is measured. However, this process is very time-consuming. Original residual stress determination is performed by numerical simulations.

For the cylindrical specimen, an analytical solution exists. Numerical results agree with the analytical solution within a 5% difference. A modified iterative analytical procedure was then developed, and exact numerical results were obtained.

A combination of two specimens was used by the Sectioning-Based method. This method uses the full potential of the developed methodology where no analytical solution exists. No additional manufacturing is required; therefore, this method is not time-consuming. Residual stress is measured on the new accessed surfaces, and then the numerical determination of the original residual stress is performed. Obtained results are in agreement with previously obtained results by the Layer-Removal-Based method.

As mentioned above, the necessary procedures combining experimental measurements using X-ray diffraction with numerical procedures using the finite element method have been developed. These procedures make it possible to obtain data on the distribution of residual stresses also at great depths, irrespective of the dimensions or weight of the component.

This is one of the key milestones of the work, which will make it possible to determine the distribution of residual stresses across the cross-section of the component and to use the data obtained to determine the residual fatigue life of the component.

##### *5. Verification of proposed methodology for determination of residual stress on testing sample.*

Next, it was necessary to validate the proposed procedures. Thin ring testing samples manufactured directly from the railway axle were used to verify the developed methodology. Specimens were manufactured from different axles. Three different methods were used to obtain tangential residual stress in specimens. Neutron diffraction by the Nuclear Physics Institute of the Czech Academy of Sciences, X-ray diffraction by the Research Centre of the University of Žilina and Slit ring method by the Institute of Physics of Materials of the Czech Academy of Sciences were performed. Results showed the same results up to the depth of 18 mm. After such depth, results obtained by different methods vary in the obtained values; however, they show a similar trend. This difference may be caused by the difference between the particular axles and their specific processing.

Thus, the validity of the proposed procedures was verified on relatively simple samples.

##### *6. Implementation of residual stress influence into procedures for estimation of residual fatigue lifetime of engineering structures.*

This part of the work consisted of a number of numerical procedures that allowed to determine the influence of all loading components on the body (in the studied case a railway axle) with a crack. The property of linear elastic fracture mechanics, which allows superposition of individual components of applied load, was used. The knowledge of the residual stress distribution, which even formed the dominant component of the load, proved to be quite crucial. A series of extensive numerical calculations allowed the distribution of residual stresses to be iteratively determined over the axle cross-section. Subsequently, further numerical calculations determined the necessary fracture parameters, which serve as inputs for subsequent analytical procedures to estimate the residual fatigue life. Previous extensive experimental works performed at IPM were used to determine the necessary material characteristics for fatigue crack propagation. All formerly

obtained parts were then subsequently used as inputs to the original procedure for estimating the residual fatigue lifetime of components.

*7. Application of proposed methodologies for determination of residual stress on real engineering component and estimation of residual fatigue lifetime.*

The railway axle was used as a suitable application for the proposed procedures. The residual fatigue lifetime estimation for the induction hardened railway axle showed no crack propagation for the considered surface crack. Therefore, the new critical position under the surface was estimated and experimentally validated. However, optic cameras cannot measure crack growth under the surface. Therefore, quenching surface treatment was considered. Residual stress was determined, and residual fatigue lifetime was estimated again. Improved residual fatigue lifetime estimation was applied at three experimentally tested full-scale axles (in co-operation with Bonatrans Group, a.s.).

The inclusion of residual stresses in the procedure for estimating the residual fatigue life of a railway axle resulted in a considerable refinement of the calculation estimates and proved to be crucial in this case, since residual stresses constitute a significant part of a load of induction hardened train axle.

The implementation of stochastic residual fatigue lifetime estimation was also performed. Several variable parameters need to be fit to estimate the residual fatigue lifetime. Therefore, taking their variability into account provides insight into the possible variance of the achieved residual lifetimes. The distribution of the residual fatigue lifetimes compared to the experimental data can help adequately adjust the inspection intervals.

*8. Dissemination of obtained results.*

Due attention was paid to the publication of the results obtained during the PhD studies. Five papers were published in scientific journals with impact factor (Theoretical and Applied Fracture Mechanics (IF = 4.374), Engineering Failure Analysis (IF = 3.634), Materials (IF = 3.748), Journal of the Mechanical Behavior of Biomedical Materials (IF = 4.042) and Additive Manufacturing (IF = 11.632). Some results were also published in four reviewed journals and conference proceedings (see Chapter 16 for details), and presented at international conferences and workshops.

**Note that the procedures proposed in this doctoral thesis are of a general nature and can also be used in other cases of sizable or heavy bodies or components.**

**In conclusion, it can be stated that all the stated objectives of the thesis have been met.**

## 12 References

- [1] P. J. Withers and H. K. D. H. Bhadeshia, "Residual stress. Part 1 – Measurement techniques," *Mater. Sci. Technol.*, vol. 17, no. 4, pp. 355–365, Apr. 2001, doi: 10.1179/026708301101509980.
- [2] T. L. Anderson, *Fracture Mechanics: Fundamental and Applications*, 4th ed. 2017.
- [3] E. E. Gdoutos, *Fracture Mechanics: An Introduction*, Third Edit., vol. 263. 2020.
- [4] H. M. Westergaard, "Bearing Pressure and Cracks," *J. Appl. Mech.*, vol. 6, pp. 49–53, 1939.
- [5] G. R. Irwin, "Analysis of Stresses and Strains Near the End of a Crack Traversing a Plate," *J. Appl. Mech.*, vol. 24, no. 3, pp. 361–364, Sep. 1957, doi: 10.1115/1.4011547.
- [6] I. N. Sneddon, "The distribution of stress in the neighbourhood of a crack in an elastic solid," *Proc. R. Soc. London. Ser. A. Math. Phys. Sci.*, vol. 187, no. 1009, pp. 229–260, Oct. 1946, doi: 10.1098/rspa.1946.0077.
- [7] P. C. Paris and G. C. Sih, "Stress Analysis of Cracks," *ASTM STP*, vol. 381, pp. 30–80, 1965.
- [8] M. L. Williams, "On the Stress Distribution at the Base of a Stationary Crack," *J. Appl. Mech.*, vol. 24, no. 1, pp. 109–114, Mar. 1956.
- [9] A. A. Griffith, "VI. The phenomena of rupture and flow in solids," *Philos. Trans. R. Soc. London. Ser. A, Contain. Pap. a Math. or Phys. Character*, vol. 221, no. 582–593, pp. 163–198, Jan. 1920, doi: 10.1098/rsta.1921.0006.
- [10] A. A. Griffith, "The theory of rupture," *Intern. Congr. Appl. Mech., 1st, Delft*, pp. 55–63, 1924.
- [11] N. E. Dowling, *Mechanical Behavior of Materials: Engineering Methods for Deformation, Fracture, and Fatigue*, Fourth. Essex: Pearson Education, 2013.
- [12] T. L. Anderson, *Fracture mechanics : fundamentals and applications*, Third. Taylor & Francis Group, 2005.
- [13] J. Kunz, *Základy lomové mechaniky*. Praha: ČVUT, 1994.
- [14] J. L. González-Velázquez, *A Practical Approach to Fracture Mechanics*. Amsterdam: Elsevier, 2021.
- [15] J. Poduška et al., "Design of plastic pipes considering content of recycled material," *Procedia Struct. Integr.*, vol. 23, pp. 293–298, 2019, doi: 10.1016/j.prostr.2020.01.102.
- [16] J. R. Rice, "Mechanics of Crack Tip Deformation and Extension by Fatigue," in *Fatigue Crack Propagation*, no. October, 100 Barr Harbor Drive, PO Box C700, West Conshohocken, PA 19428-2959: ASTM International, 1967, pp. 247–65. doi: 10.1520/STP47234S.
- [17] J. R. Rice, "Mathematical Analysis in the Mechanics of Fracture," in *Fracture: An Advanced Treatise (Vol. 2, Mathematical Fundamentals)*, vol. 2, H. Liebowitz, Ed. New York: Academic Press, 1968, pp. 191–311.
- [18] M. Klesnil and P. Lukáš, *Fatigue of Metallic Materials*, 2nd ed. Prague: Academia, 1992.
- [19] J. C. Newman, "Fatigue and crack-growth analyses under Giga-cycle loading on aluminum alloys," *Procedia Eng.*, vol. 101, no. C, pp. 339–346, 2015, doi: 10.1016/j.proeng.2015.02.041.
- [20] J. Schijve, *Fatigue of Structures and Materials*, 2nd ed. Dordrecht: Springer Netherlands, 2008.
- [21] S. Suresh, *Fatigue of Materials*, Second. New York: Cambridge University Press, 1998. doi: 10.1017/CBO9780511806575.
- [22] J. Polák, *Cyclic Deformation, Crack Initiation, and Low-Cycle Fatigue*, no. June 2015. 2016. doi: 10.1016/b978-0-12-803581-8.00890-0.
- [23] A. Wöhler, "Versuche zur Ermittlung der auf die Eisenbahnwagenachsen einwirkenden Kräfte und die Widerstandsfähigkeit des Wagen-Achsen," *Zeitschrift für Bauwes.*, vol. 10, pp. 583–616, 1860.
- [24] J. Polak, "Cyclic plasticity and low cycle fatigue life of metals," in *Materials science monographs 63*, 2nd ed., Prague: Academia, 1991, p. 316. [Online]. Available: <http://www.csa.com/partners/viewrecord.php?requester=gs&collection=TRD&recid=199210720461MD>
- [25] P. Paris and F. Erdogan, "A critical analysis of crack propagation laws," *J. Basic Eng.*, vol. 85, no. 4, pp. 528–533, 1963, doi: 10.1115/1.3656900.
- [26] P. C. Paris, "The Growth of Cracks Due to Variations in Load," Lehigh University, 1962. [Online]. Available: <http://dx.doi.org/10.1016/j.jaci.2012.05.050>
- [27] P. C. Paris, M. P. Gomez, and W. E. Anderson, "A Rational Analytic Theory of Fatigue," *The Trend in Engineering*, vol. 13. pp. 9–14, 1961.

- [28] G. C. Sih, P. C. Paris, and F. Erdogan, "Crack-Tip, Stress-Intensity Factors for Plane Extension and Plate Bending Problems," *J. Appl. Mech.*, vol. 29, pp. 306–312, 1962, doi: 10.1115/1.3640546.
- [29] R. I. Stephens, "Fatigue Design Criteria," *Encycl. Mater. Sci. Technol.*, pp. 2910–2918, 2001, doi: 10.1016/b0-08-043152-6/00518-0.
- [30] U. Zerbst, K. Mädler, and H. Hintze, "Fracture mechanics in railway applications - An overview," *Eng. Fract. Mech.*, vol. 72, no. 2, pp. 163–194, 2005, doi: 10.1016/j.engfracmech.2003.11.010.
- [31] D. R. H. Jones and M. F. Ashby, "Fatigue Design," *Eng. Mater. 1*, pp. 301–324, 2019, doi: 10.1016/b978-0-08-102051-7.00018-x.
- [32] Y. Bai and W.-L. Jin, "Introduction," *Mar. Struct. Des.*, pp. 3–18, 2016, doi: 10.1016/b978-0-08-099997-5.00001-0.
- [33] R. I. Stephens, A. Fatemi, R. R. Stephens, and H. O. Fuchs, *Metal Fatigue in Engineering*, 2nd ed. John Wiley & Sons, Inc., 2000.
- [34] "BS 8535:2011 Railway applications. Wheelsets and bogies. Powered and non-powered axles with inboard bearings. Design method," 2013.
- [35] SKF-Group, *Railway technical handbook - Axleboxes, wheelset bearings, sensors, condition monitoring, subsystems and services*, vol. 1. 2012.
- [36] F. Dikmen, "Axle fractures and precaution in rail vehicles: computer based dynamic analysis and constructive approach," Yildiz Technical University, Istanbul (in Turkish), 1989.
- [37] "EN 13103-1 Railway applications. Wheelsets and bogies. Design method for axles with external journals," 2019.
- [38] "EN 13261 Railway applications. Wheelsets and bogies. Axles. Product requirements," 2021.
- [39] "CEN/TR 17469:2020 Railway applications - Axle design method," 2020.
- [40] "UIC Leaflet 811-1 Technical specification for the supply of axles for tractive and trailing stock," Paris, 1987.
- [41] A. Bracciali, "Railway Wheelsets: History, Research and Developments," *Int. J. Railw. Technol.*, vol. 5, no. 1, pp. 23–52, 2016, doi: 10.4203/ijrt.5.1.2.
- [42] A. Bracciali, "Apparently independently rotating wheelset - A possible solution for all needs?," *Stephenson Conf. Res. Railw. 2015*, vol. 2015-April, pp. 427–440, 2015.
- [43] P. J. Mistry, M. S. Johnson, C. A. McRobie, and I. A. Jones, "Design of a lightweight multifunctional composite railway axle utilising coaxial skins," *J. Compos. Sci.*, vol. 5, no. 3, 2021, doi: 10.3390/jcs5030077.
- [44] D. Sala, "LURSAK : The new high performances axle protection," 2011.
- [45] U. Zerbst, C. Klinger, and D. Klingbeil, "Structural assessment of railway axles - A critical review," *Eng. Fail. Anal.*, vol. 35, pp. 54–65, 2013, doi: 10.1016/j.engfailanal.2012.11.007.
- [46] WIDEM - Wheelset integrated design and effective maintenance, "D7 . 1 – Procedure to define NDT periodicity as function of vehicle service profile," 2008. [Online]. Available: [http://www.widem.org/file.php?id=54&save\\_dialogue=1](http://www.widem.org/file.php?id=54&save_dialogue=1)
- [47] M. Carboni and S. Cantini, "Advanced ultrasonic 'Probability of Detection' curves for designing in-service inspection intervals," *Int. J. Fatigue*, vol. 86, pp. 77–87, 2016, doi: 10.1016/j.ijfatigue.2015.07.018.
- [48] G. A. Georgio and Jacobi Consulting Limited, "Probability of Detection ( PoD ) curves Derivation, applications and limitations," 2006. [Online]. Available: <http://www.hse.gov.uk/research/rrhtm/rr454.htm>
- [49] G. A. Georgiou, "PoD curves, their derivation, applications and limitations," *Insight - Non-Destructive Test. Cond. Monit.*, vol. 49, no. 7, pp. 409–414, Jul. 2007, doi: 10.1784/insi.2007.49.7.409.
- [50] J. N. Gray, T. A. Gray, N. Nakagawa, and R. B. Thompson, "Models for Predicting NDE Reliability," in *ASM Handbook, volume 17, Nondestructive Evaluation and Quality Control*, 1992, pp. 1470–1496.
- [51] S. Cantini, M. Carboni, S. Beretta, and C. Gilardoni, "An overview of optimized inspection plans for high speed axles," *Eur. Conf. NDT*, no. Econdt, 2014.
- [52] D. Meccanica and P. Milano, "Una nuova prospettiva nella derivazione e nella caratterizzazione delle curve POD," 2009.
- [53] G. A. Matzkanin and H. T. Yolken, *A Technology Assessment of Probability of Detection (POD) for Nondestructive Evaluation*, no. August. 2001.

- [54] M. Carboni and S. Cantini, "A ' Model Assisted Probability of Detection ' approach for ultrasonic inspection of railway axles," *18th World Conf. Nondestruct. Test.*, no. April, pp. 16–20, 2012.
- [55] J. A. Benyon and A. S. Watson, "Axle inspection: The use of Monte Carlo analysis and risk assessment to optimize axle inspection interval," 1999.
- [56] R. Singh, "Three Decades of NDI Reliability Assessment (Report No. Karta-3510-99-01)," 2000.
- [57] M. Traupe, S. Jenne, K. Lütkepohl, and I. Varfolomeev, "Experimental validation of inspection intervals for railway axles accompanying the engineering process," *Int. J. Fatigue*, vol. 86, pp. 44–51, 2016, doi: 10.1016/j.ijfatigue.2015.09.020.
- [58] C. Mallor, S. Calvo, J. L. Nuñez, R. Rodriguez-Barrachina, and A. Landaberea, "A probabilistic fatigue crack growth life approach to the definition of inspection intervals for railway axles," *Frat. ed Integrità Strutt.*, vol. 16, no. 59, pp. 359–373, Dec. 2021, doi: 10.3221/IGF-ESIS.59.24.
- [59] U. Zerbst *et al.*, "Safe life and damage tolerance aspects of railway axles – A review," *Eng. Fract. Mech.*, vol. 98, pp. 214–271, Jan. 2013, doi: 10.1016/j.engfracmech.2012.09.029.
- [60] X. Wang and S. B. Lambert, "Local weight functions for semi-elliptical surface cracks in finite thickness plates," *Theor. Appl. Fract. Mech.*, vol. 23, no. 3, pp. 199–208, 1995, doi: 10.1016/0167-8442(95)00022-7.
- [61] X. Wang and S. B. Lambert, "Stress intensity factors for low aspect ratio semi-elliptical surface cracks in finite-thickness plates subjected to nonuniform stresses," *Eng. Fract. Mech.*, vol. 51, no. 4, pp. 517–532, 1995, doi: 10.1016/0013-7944(94)00311-5.
- [62] M. Madia, S. Beretta, M. Schödel, U. Zerbst, M. Luke, and I. Varfolomeev, "Stress intensity factor solutions for cracks in railway axles," *Eng. Fract. Mech.*, vol. 78, no. 5, pp. 764–792, 2011, doi: 10.1016/j.engfracmech.2010.03.019.
- [63] D. Regazzi, S. Cantini, S. Cervello, S. Foletti, A. Pourheidar, and S. Beretta, "Improving fatigue resistance of railway axles by cold rolling: Process optimisation and new experimental evidences," *Int. J. Fatigue*, vol. 137, no. February, p. 105603, 2020, doi: 10.1016/j.ijfatigue.2020.105603.
- [64] M. Rieger *et al.*, "Fatigue crack growth in full-scale railway axles – Influence of secondary stresses and load sequence effects," *Int. J. Fatigue*, vol. 132, no. October 2019, p. 105360, 2020, doi: 10.1016/j.ijfatigue.2019.105360.
- [65] D. Simunek, M. Leitner, M. Rieger, R. Pippan, H. P. Gänser, and F. J. Weber, "Fatigue crack growth in railway axle specimens – Transferability and model validation," *Int. J. Fatigue*, vol. 133, no. October 2019, p. 105421, 2020, doi: 10.1016/j.ijfatigue.2019.105421.
- [66] J. Maierhofer, H. P. Gänser, D. Simunek, M. Leitner, R. Pippan, and M. Luke, "Fatigue crack growth model including load sequence effects – Model development and calibration for railway axle steels," *Int. J. Fatigue*, vol. 132, no. July 2019, p. 105377, 2020, doi: 10.1016/j.ijfatigue.2019.105377.
- [67] H.-P. Gänser, K. Kunter, and F.-J. Weber, "EBFW-3 project: Final report," 2021. [Online]. Available: [http://www.ebfw3.net/EBFW3\\_FinalReport\\_rev\\_1\\_2021-07-30\\_withAppendix.pdf](http://www.ebfw3.net/EBFW3_FinalReport_rev_1_2021-07-30_withAppendix.pdf)
- [68] M. Luke, I. Varfolomeev, K. Lütkepohl, and A. Esderts, "Fatigue crack growth in railway axles: Assessment concept and validation tests," *Eng. Fract. Mech.*, vol. 78, no. 5, pp. 714–730, 2011, doi: 10.1016/j.engfracmech.2010.11.024.
- [69] A. R. Torabi and M. R. M. Aliha, "Determination of permissible defect size for solid axles loaded under fully-reversed rotating bending," *Eng. Solid Mech.*, vol. 1, no. 1, pp. 27–36, Jan. 2013, doi: 10.5267/j.esm.2013.06.003.
- [70] A. Pourheidar, S. Beretta, D. Ragazzi, and C. Baykara, "Comparison of SIF solutions for cracks under rotating bending and their impact upon propagation lifetime of railway axles," *Procedia Struct. Integr.*, vol. 8, pp. 610–617, 2018, doi: 10.1016/j.prostr.2017.12.060.
- [71] O. Yasniy, Y. Lapusta, Y. Pyndus, A. Soroachak, and V. Yasniy, "Assessment of lifetime of railway axle," *Int. J. Fatigue*, vol. 50, pp. 40–46, 2013, doi: 10.1016/j.ijfatigue.2012.04.008.
- [72] V. Giannella, "Stochastic approach to fatigue crack-growth simulation for a railway axle under input data variability," *Int. J. Fatigue*, vol. 144, no. November 2020, p. 106044, 2021, doi: 10.1016/j.ijfatigue.2020.106044.
- [73] J. C. Martínez, L. V. Vanegas Useche, and M. A. Wahab, "Numerical prediction of fretting fatigue crack trajectory in a railway axle using XFEM," *Int. J. Fatigue*, vol. 100, pp. 32–49, 2017, doi: 10.1016/j.ijfatigue.2017.03.009.
- [74] V. Giannella, R. Sepe, A. Borrelli, G. De Michele, and E. Armentani, "Numerical investigation on the

- fracture failure of a railway axle," *Eng. Fail. Anal.*, vol. 129, no. August, p. 105680, 2021, doi: 10.1016/j.engfailanal.2021.105680.
- [75] M. Madia, S. Beretta, and U. Zerbst, "An investigation on the influence of rotary bending and press fitting on stress intensity factors and fatigue crack growth in railway axles," *Eng. Fract. Mech.*, vol. 75, no. 8, pp. 1906–1920, 2008, doi: 10.1016/j.engfracmech.2007.08.015.
- [76] A. T. Zehnder, *Fracture Mechanics*, vol. 62. Dordrecht: Springer Netherlands, 2012. doi: 10.1007/978-94-007-2595-9.
- [77] "ANSYS Help, 2019R3, 2.4. Fracture-Parameter Calculation Typers (28.07.2021)."
- [78] J. R. Rice, "A Path Independent Integral and the Approximate Analysis of Strain Concentration by Notches and Cracks," *J. Appl. Mech.*, vol. 35, no. 2, pp. 379–386, 1968, doi: 10.1115/1.3601206.
- [79] J. Kunz, *Aplikovaná lomová mechanika*. Prague: ČVUT, 2005.
- [80] ANSYS, "ANSYS Mechanical Fracture Mechanics 2019 R3 - Module 04: Fracture Parameter Evaluation." p. 28.
- [81] R. D. Henshell and K. G. Shaw, "Crack tip finite elements are unnecessary," *Int. J. Numer. Methods Eng.*, vol. 9, no. 3, pp. 495–507, 1975, doi: 10.1002/nme.1620090302.
- [82] R. S. Barsoum, "On the use of isoparametric finite elements in linear fracture mechanics," *Int. J. Numer. Methods Eng.*, vol. 10, no. October 1974, pp. 25–37, 1976.
- [83] A. R. Ingraffea and C. Manu, "Stress-intensity factor computation in three dimensions with quarter-point elements," *Int. J. Numer. Methods Eng.*, vol. 15, no. 10, pp. 1427–1445, 1980, doi: 10.1002/nme.1620151002.
- [84] C. Manu, "Quarter-point elements for curved crack fronts," *Comput. Struct.*, vol. 17, no. 2, pp. 227–231, 1983, doi: 10.1016/0045-7949(83)90010-X.
- [85] J. Schijve, Ed., "Fatigue Crack Growth. Analysis and Predictions," in *Fatigue of Structures and Materials*, Dordrecht: Springer Netherlands, 2008, pp. 209–256. doi: 10.1007/978-1-4020-6808-9\_8.
- [86] "NASGRO<sup>®</sup> Fracture Mechanics and Fatigue Crack Growth Analysis Software - Reference manual," 2002.
- [87] J. C. J. Newman, "(NASA-TM-81941) A Crack-Closure Model for Predicting Fatigue-Crack Growth under Aircraft Spectrum Loading," 1981. [Online]. Available: <https://ntrs.nasa.gov/archive/nasa/casi.ntrs.nasa.gov/19810009887.pdf>
- [88] R. G. Forman, V. E. Kearney, and R. M. Engle, "Numerical analysis of crack propagation in cyclic-loaded structures," *J. Fluids Eng. Trans. ASME*, vol. 89, no. 3, pp. 459–463, 1967, doi: 10.1115/1.3609637.
- [89] E. K. Priddle, "High cycle fatigue crack propagation under random and constant amplitude loadings," *Int. J. Press. Vessel. Pip.*, vol. 4, no. 2, pp. 89–117, 1976, doi: 10.1016/0308-0161(76)90014-4.
- [90] K. Walker, *The effect of Stress Ratio During Crack Propagation and Fatigue for 2024-T3 and 7075-T6 Aluminum*. ASTM Special Technical Publication, 1970. doi: 10.1520/stp462-eb.
- [91] M. Klesnil and P. Lukáš, "Influence of strength and stress history on growth and stabilisation of fatigue cracks," *Eng. Fract. Mech.*, vol. 4, no. 1, pp. 77–92, 1972, doi: 10.1016/0013-7944(72)90078-1.
- [92] P. J. Withers, "Residual stress and its role in failure," *Reports Prog. Phys.*, vol. 70, no. 12, pp. 2211–2264, 2007, doi: 10.1088/0034-4885/70/12/R04.
- [93] D. Löhe, K.-H. Lang, and O. Vöhringer, "Residual Stresses and Fatigue Behavior," in *Handbook of Residual Stress and Deformation of Steel*, 2002, pp. 27–53. doi: 10.1361/hrsd2002p027.
- [94] A. G. Youtsos, Ed., *Residual Stress and Its Effects on Fatigue and Fracture*. Springer, 2006.
- [95] J. O. Bunch and M. R. Mitchell, *Residual Stress Effects on Fatigue and Fracture Testing and Incorporation of Results into Design*. 100 Barr Harbor Drive, PO Box C700, West Conshohocken, PA 19428-2959: ASTM International, 2007. doi: 10.1520/STP1497-EB.
- [96] A. K. Vasudevan, K. Sadananda, and G. Glinka, "Critical parameters for fatigue damage," *Int. J. Fatigue*, vol. 23, no. SUPPL. 1, pp. 39–53, 2001, doi: 10.1016/s0142-1123(01)00171-2.
- [97] P. Hutař, M. Ševčík, A. Frank, L. Náhlík, J. Kučera, and G. Pinter, "The effect of residual stress on polymer pipe lifetime," *Eng. Fract. Mech.*, vol. 108, pp. 98–108, 2013, doi: 10.1016/j.engfracmech.2013.04.014.
- [98] H.-J. Schindler, "Effect of Residual Stresses on Safe Life Prediction of Railway Axles," *Procedia Struct. Integr.*, vol. 4, pp. 48–55, 2017, doi: 10.1016/j.prostr.2017.07.008.
- [99] P. Pokorný *et al.*, "Influence of heat treatment-induced residual stress on residual fatigue life of railway

- axles," *Theor. Appl. Fract. Mech.*, vol. 109, no. July, p. 102732, Oct. 2020, doi: 10.1016/j.tafmec.2020.102732.
- [100] E. Brinksmeier, J. T. Cammett, W. König, P. Leskovar, J. Peters, and H. K. Tönshoff, "Residual Stresses — Measurement and Causes in Machining Processes," *CIRP Ann.*, vol. 31, no. 2, pp. 491–510, 1982, doi: 10.1016/S0007-8506(07)60172-3.
- [101] J. Epp, "X-ray diffraction (XRD) techniques for materials characterization," in *Materials Characterization Using Nondestructive Evaluation (NDE) Methods*, Elsevier, 2016, pp. 81–124. doi: 10.1016/B978-0-08-100040-3.00004-3.
- [102] Y. B. Guo, W. Li, and I. S. Jawahir, "Surface integrity characterization and prediction in machining of hardened and difficult-to-machine alloys: a state-of-art research review and analysis," pp. 437–470, 2009, doi: 10.1080/10910340903454922.
- [103] J. Lu, "Prestress engineering of structural material: A global design approach to the residual stress problem," in *Handbook of Residual Stress and Deformation of Steel*, 2002, pp. 11–26. doi: 10.1361/hrsd2002p011.
- [104] G. S. Schajer and C. O. Ruud, "Overview of Residual Stresses and Their Measurement," in *Practical Residual Stress Measurement Methods*, Chichester, UK: John Wiley & Sons, Ltd, 2013, pp. 1–27. doi: 10.1002/9781118402832.ch1.
- [105] P. J. Withers, "Residual Stress: Definition," in *Encyclopedia of Materials: Science and Technology*, 2001, pp. 8110–8112.
- [106] E. Macherauch, H. Wohlfahrt, and U. Wolfstieg, "Zur zweckmäßigen Definition von Eigenspannungen," *HTM - Haertere-Technische Mitteilungen*, vol. 28, no. 3, pp. 201–211, 1973.
- [107] F. A. Kandil, J. D. Lord, A. T. Fry, and P. V. Grant, "A Review of Residual Stress Measurement Methods - A Guide to Technique Selection," 2001.
- [108] M. R. James and J. Lu, "Introduction," in *Handbook of measurement of residual stresses*, 1996, pp. 6–9.
- [109] D. L. Ball *et al.*, "The impact of forging residual stress on fatigue in aluminum," in *56th AIAA/ASCE/AHS/ASC Structures, Structural Dynamics, and Materials Conference*, Jan. 2015, no. January, pp. 1–16. doi: 10.2514/6.2015-0386.
- [110] A. Abvabi, B. Rolfe, P. D. Hodgson, and M. Weiss, "The influence of residual stress on a roll forming process," *Int. J. Mech. Sci.*, vol. 101–102, pp. 124–136, Oct. 2015, doi: 10.1016/j.ijmecsci.2015.08.004.
- [111] X. Ficquet, A. Bowman, D. Goudar, M. Körner, and E. J. Kingston, "Measurement of bending residual stress on a hull section of a submarine," *Proc. Int. Conf. Offshore Mech. Arct. Eng. - OMAE*, vol. 6, pp. 117–127, 2012, doi: 10.1115/OMAE2012-83378.
- [112] N. T. Rudkins, G. F. Modlen, and P. J. Webster, "Residual stresses in cold extrusion and cold drawing: a finite element and neutron diffraction study," *J. Mater. Process. Tech.*, vol. 45, no. 1–4, pp. 287–292, 1994, doi: 10.1016/0924-0136(94)90354-9.
- [113] S. Jeelani, S. Biswas, and R. Natarajan, "Effect of cutting speed and tool rake angle on residual stress distribution in machining 2024-T351 aluminium alloy - unlubricated conditions," *J. Mater. Sci.*, vol. 21, no. 8, pp. 2705–2710, 1986, doi: 10.1007/BF00551476.
- [114] W. Ding, L. Zhang, Z. Li, Y. Zhu, H. Su, and J. Xu, "Review on grinding-induced residual stresses in metallic materials," *Int. J. Adv. Manuf. Technol.*, vol. 88, no. 9–12, pp. 2939–2968, 2017, doi: 10.1007/s00170-016-8998-1.
- [115] J. Y. Song and J. Yu, "Residual stress measurements in electroless plated Ni-P films," *Thin Solid Films*, vol. 415, no. 1–2, pp. 167–172, 2002, doi: 10.1016/S0040-6090(02)00556-4.
- [116] M. Kattoura, S. R. Mannava, D. Qian, and V. K. Vasudevan, "Effect of laser shock peening on residual stress, microstructure and fatigue behavior of ATI 718Plus alloy," *Int. J. Fatigue*, vol. 102, pp. 121–134, 2017, doi: 10.1016/j.ijfatigue.2017.04.016.
- [117] G. Donzella, R. Gerosa, C. Petrogalli, B. Rivolta, G. Silva, and M. Beretta, "Evaluation of the residual stresses induced by shot peening on some sintered steels," *Procedia Eng.*, vol. 10, pp. 3399–3404, 2011, doi: 10.1016/j.proeng.2011.04.560.
- [118] H. Hizli and C. H. GÜR, "Applicability of the Magnetic Barkhausen Noise Method for Nondestructive Measurement of Residual Stresses in the Carburized and Tempered 19CrNi5H Steels," *Res. Nondestruct. Eval.*, vol. 29, no. 4, pp. 221–236, Oct. 2018, doi: 10.1080/09349847.2017.1359711.
- [119] B. A. Szost *et al.*, "A comparative study of additive manufacturing techniques: Residual stress and microstructural analysis of CLAD and WAAM printed Ti-6Al-4V components," *Mater. Des.*, vol. 89, pp.

- 559–567, 2016, doi: 10.1016/j.matdes.2015.09.115.
- [120] S. K. Bate, P. Hurrell, A. Francis, and M. Turski, “Uk research programme on residual stresses - A review of progress,” *Am. Soc. Mech. Eng. Press. Vessel. Pip. Div. PVP*, vol. 6, no. PARTS A AND B, pp. 251–258, 2008, doi: 10.1115/PVP2008-61073.
- [121] A. A. Keste, S. H. Gawande, and C. Sarkar, “Design optimization of precision casting for residual stress reduction,” *J. Comput. Des. Eng.*, vol. 3, no. 2, pp. 140–150, 2016, doi: 10.1016/j.jcde.2015.10.003.
- [122] L. de C. F. Canale and M. Narazaki, *Quenching and cooling, residual stress and distortion control*. 2010. [Online]. Available: <http://www.tandfonline.com/doi/full/10.1179/174951410X12712449937405>
- [123] P. J. Withers, W. M. Stobbs, and O. B. Pedersen, “The application of the eshelby method of internal stress determination to short fibre metal matrix composites,” *Acta Metall.*, vol. 37, no. 11, pp. 3061–3084, Nov. 1989, doi: 10.1016/0001-6160(89)90341-6.
- [124] N. S. Rossini, M. Dassisti, K. Y. Benyounis, and A. G. Olabi, “Methods of measuring residual stresses in components,” *Mater. Des.*, vol. 35, pp. 572–588, 2012, doi: 10.1016/j.matdes.2011.08.022.
- [125] G. S. Schajer, Ed., *Practical Residual Stress Measurement Methods*. Chichester, UK: John Wiley & Sons, Ltd, 2013. doi: 10.1002/9781118402832.
- [126] J. Guo, H. Fu, B. Pan, and R. Kang, “Recent progress of residual stress measurement methods: A review,” *Chinese J. Aeronaut.*, Nov. 2019, doi: 10.1016/j.cja.2019.10.010.
- [127] D. I. Crecraft, “The measurement of applied and residual stresses in metals using ultrasonic waves,” *J. Sound Vib.*, vol. 5, no. 1, pp. 173–192, 1967, doi: 10.1016/0022-460X(67)90186-1.
- [128] K. Y. Jhang, H. H. Quan, J. Ha, and N. Y. Kim, “Estimation of clamping force in high-tension bolts through ultrasonic velocity measurement,” *Ultrasonics*, vol. 44, no. SUPPL., pp. 1339–1342, 2006, doi: 10.1016/j.ultras.2006.05.190.
- [129] Y. Sasaki and M. Hasegawa, “Effect of anisotropy on acoustoelastic birefringence in wood,” *Ultrasonics*, vol. 46, no. 2, pp. 184–190, 2007, doi: 10.1016/j.ultras.2007.01.009.
- [130] S. Chaki, G. Corneloup, I. Lillamand, and H. Walaszek, “Combination of longitudinal and transverse ultrasonic waves for in situ control of the tightening of bolts,” *J. Press. Vessel Technol. Trans. ASME*, vol. 129, no. 3, pp. 383–390, 2007, doi: 10.1115/1.2748821.
- [131] E. Hu, Y. He, and Y. Chen, “Experimental study on the surface stress measurement with Rayleigh wave detection technique,” *Appl. Acoust.*, vol. 70, no. 2, pp. 356–360, 2009, doi: 10.1016/j.apacoust.2008.03.002.
- [132] M. Liu, J. Y. Kim, L. Jacobs, and J. Qu, “Experimental study of nonlinear Rayleigh wave propagation in shot-peened aluminum plates Feasibility of measuring residual stress,” *NDT E Int.*, vol. 44, no. 1, pp. 67–74, 2011, doi: 10.1016/j.ndteint.2010.09.008.
- [133] T. Leon-Salamanca and D. F. Bray, “Residual stress measurement in steel plates and welds using critically refracted longitudinal (LCR) Waves,” *Res. Nondestruct. Eval.*, vol. 7, no. 4, pp. 169–184, 1996, doi: 10.1080/09349849609409576.
- [134] R. B. Thompson, W.-Y. Lu, and A. V. J. Clark Jr., “Ultrasonic Methods,” in *Handbook of measurement of residual stresses*, 1996, pp. 153–182.
- [135] W. Song, C. Xu, Q. Pan, and J. Song, “Nondestructive testing and characterization of residual stress field using an ultrasonic method,” *Chinese J. Mech. Eng. (English Ed.)*, vol. 29, no. 2, pp. 365–371, 2016, doi: 10.3901/CJME.2015.1023.126.
- [136] E. R. Leeman, “The Measurement of Stress in Rock Part I: The Principles of Rock Stress Measurements,” *J. south african Inst. Min. Andm.*, pp. 45–81, 1964, [Online]. Available: [https://hdl.handle.net/10520/AJA0038223X\\_4882](https://hdl.handle.net/10520/AJA0038223X_4882)
- [137] E. R. Leeman, “The Measurement of Stress in Rock Part II: The Principles of Rock Stress Measurements: Borehole Rock Stress Measuring Instruments,” *J. south african Inst. Min. Andm.*, pp. 82–114, 1964.
- [138] E. R. Leeman, “The Measurement of Stress in Rock Part III: The Results of some Rock Stress Investigations,” *J. south african Inst. Min. Andm.*, pp. 254–284, 1964, [Online]. Available: [https://hdl.handle.net/10520/AJA0038223X\\_4945](https://hdl.handle.net/10520/AJA0038223X_4945)
- [139] C. Fairhurst, “Stress estimation in rock: A brief history and review,” *Int. J. Rock Mech. Min. Sci.*, vol. 40, no. 7–8, pp. 957–973, 2003, doi: 10.1016/j.ijrmms.2003.07.002.
- [140] D. J. Smith, “Deep Hole Drilling,” in *Practical Residual Stress Measurement Methods*, 2013, pp. 65–87. doi: 10.1002/9781118402832.ch3.

- [141] R. H. Leggatt, D. J. Smith, S. D. Smith, and F. Faure, "Development and experimental validation of the deep hole method for residual stress measurement," *J. Strain Anal. Eng. Des.*, vol. 31, no. 3, pp. 177–186, 1996, doi: 10.1243/03093247V313177.
- [142] A. T. DeWald and M. R. Hill, "Improved data reduction for the deep-hole method of residual stress measurement," *J. Strain Anal. Eng. Des.*, vol. 38, no. 1, pp. 65–78, 2003, doi: 10.1243/030932403762671908.
- [143] D. J. Smith, P. J. Bouchard, and D. George, "Measurement and prediction of residual stresses in thick-section steel welds," *J. Strain Anal. Eng. Des.*, vol. 35, no. 4, pp. 287–305, 2000, doi: 10.1243/0309324001514422.
- [144] R. S. E. VEQTER, "The Deep-Hole Drilling Technique," 2020. <https://www.veqter.co.uk/residual-stress-measurement/deep-hole-drilling>
- [145] A. H. Mahmoudi, S. Hossain, C. E. Truman, D. J. Smith, and M. J. Pavier, "A New Procedure to Measure Near Yield Residual Stresses Using the Deep Hole Drilling Technique," *Exp. Mech.*, vol. 49, no. 4, pp. 595–604, Aug. 2009, doi: 10.1007/s11340-008-9164-y.
- [146] A. H. Mahmoudi, C. E. Truman, D. J. Smith, and M. J. Pavier, "The effect of plasticity on the ability of the deep hole drilling technique to measure axisymmetric residual stress," *Int. J. Mech. Sci.*, vol. 53, no. 11, pp. 978–988, 2011, doi: 10.1016/j.ijmecsci.2011.08.002.
- [147] D. M. Goudar, C. E. Truman, and D. J. Smith, "Evaluating uncertainty in residual stress measured using the deep-hole drilling technique," *Strain*, vol. 47, no. 1, pp. 62–74, 2011, doi: 10.1111/j.1475-1305.2009.00620.x.
- [148] D. Biermann, F. Bleicher, U. Heisel, F. Klocke, H. C. Möhring, and A. Shih, "Deep hole drilling," *CIRP Ann.*, vol. 67, no. 2, pp. 673–694, 2018, doi: 10.1016/j.cirp.2018.05.007.
- [149] S. Vaidyanathan and I. Finnie, "Determination of residual stresses from stress intensity factor measurements," *J. Fluids Eng. Trans. ASME*, vol. 93, no. 2, pp. 242–246, 1971, doi: 10.1115/1.3425220.
- [150] W. Cheng and L. Finnie, "A method for measurement of axisymmetric axial residual stresses in circumferentially welded thin-walled cylinders," *J. Eng. Mater. Technol. Trans. ASME*, vol. 107, no. 3, pp. 181–185, 1985, doi: 10.1115/1.3225799.
- [151] W. Cheng, I. Finnie, and Vardar, "Measurement of residual stresses near the surface using the crack compliance method," *J. Eng. Mater. Technol. Trans. ASME*, vol. 113, no. 2, pp. 199–204, 1991, doi: 10.1115/1.2903392.
- [152] W. Cheng, I. Finnie, M. Gremaud, A. Rosselet, and R. D. Streit, "The Compliance Method for Measurement of Near Surface Residual Stresses—Application and Validation for Surface Treatment by Laser and Shot-Peening," *J. Eng. Mater. Technol.*, vol. 116, no. 4, pp. 556–560, Oct. 1994, doi: 10.1115/1.2904328.
- [153] I. Finnie and W. Cheng, "Residual stress measurement by the introduction of slots or cracks," *Localized Damage IV Comput. Aided Assess. Control Localized Damage – Proc. Int. Conf. 1996*, vol. 13, pp. 37–51, 1996.
- [154] I. Finnie and W. Cheng, "A summary of past contributions on residual stresses," *Mater. Sci. Forum*, vol. 404–407, pp. 509–514, 2002, doi: 10.4028/www.scientific.net/msf.404-407.509.
- [155] M. B. Prime, "Residual Stress Measurement by Successive Extension of a Slot: The Crack Compliance Method," *Appl. Mech. Rev.*, vol. 52, no. 2, pp. 75–96, Feb. 1999, doi: 10.1115/1.3098926.
- [156] W. Cheng and I. Finnie, *Residual Stress Measurement and the Slitting Method*. Boston, MA: Springer US, 2007. doi: 10.1007/978-0-387-39030-7.
- [157] M. R. Hill, "The Slitting Method," in *Practical Residual Stress Measurement Methods*, 2013. doi: 10.1002/9781118402832.ch4.
- [158] M. J. Lee and M. R. Hill, "Intralaboratory repeatability of residual stress determined by the slitting method," *Exp. Mech.*, vol. 47, no. 6, pp. 745–752, 2007, doi: 10.1007/s11340-007-9085-1.
- [159] M. J. Lee and M. R. Hill, "Effect of strain gage length when determining residual stress by slitting," *J. Eng. Mater. Technol. Trans. ASME*, vol. 129, no. 1, pp. 143–150, 2007, doi: 10.1115/1.2400263.
- [160] H. J. Schindler, W. Cheng, and I. Finnie, "Experimental determination of stress intensity factors due to residual stresses," *Exp. Mech.*, vol. 37, no. 3, pp. 272–277, 1997, doi: 10.1007/BF02317418.
- [161] H. J. Schindler and P. Bertschinger, "Some steps towards automation of the crack compliance method to measure residual stress distributions," *Proc. 5th Int. Conf. Res. Stress. ICRS-5*, vol. 1, no. January, pp. 682–687, 1997, [Online]. Available: <http://www.mat-tec.ch/2002/bibli/ICRS5.pdf>

- [162] M. R. Hill and J. E. Vandalen, "Evaluation of residual stress corrections to fracture toughness values," *J. ASTM Int.*, vol. 5, no. 8, pp. 1–11, 2008, doi: 10.1520/JAI101713.
- [163] T. Ghidini and C. D. Donne, "Fatigue crack propagation assessment based on residual stresses obtained through cut-compliance technique," *Fatigue Fract. Eng. Mater. Struct.*, vol. 30, no. 3, pp. 214–222, 2007, doi: 10.1111/j.1460-2695.2006.01059.x.
- [164] M. B. Prime and A. R. Gonzales, "The contour method: Simple 2-D mapping of residual stresses," *Am. Soc. Mech. Eng. Press. Vessel. Pip. Div. PVP*, vol. 415, no. January 2000, pp. 121–127, 2000.
- [165] M. B. Prime, "Cross-sectional mapping of residual stresses by measuring the surface contour after a cut," *J. Eng. Mater. Technol. Trans. ASME*, vol. 123, no. 2, pp. 162–168, 2001, doi: 10.1115/1.1345526.
- [166] H. F. Bueckner, "The Propagation of Cracks and the Energy of Elastic Deformation," *Trans. Am. Soc. Mech. Eng. Am. Soc. Mech. Eng.*, vol. 80, no. 6, pp. 1225–1230, Aug. 1958, [Online]. Available: <https://linkinghub.elsevier.com/retrieve/pii/0043164859902790>
- [167] H. F. Bueckner, "Novel Principle for the Computation of Stress Intensity Factors," *Zeitschrift fuer Angew. Math. Mech.*, vol. 50, no. 9, pp. 529–546, 1970.
- [168] H. F. Bueckner, "Field singularities and related integral representations," in *Methods of analysis and solutions of crack problems*, Dordrecht: Springer Netherlands, 1973, pp. 239–314. doi: 10.1007/978-94-017-2260-5\_5.
- [169] P. C. Paris, "The Mechanics of Fracture Propagation and Solutions to Fracture Arrestor Problem (D2-2195)," 1957.
- [170] J. D. Eshelby, "The determination of the elastic field of an ellipsoidal inclusion, and related problems," *Proc. R. Soc. London. Ser. A. Math. Phys. Sci.*, vol. 241, no. 1226, pp. 376–396, Aug. 1957, doi: 10.1098/rspa.1957.0133.
- [171] M. B. Toparli, M. E. Fitzpatrick, and S. Gungor, "Improvement of the Contour Method for Measurement of Near-Surface Residual Stresses from Laser Peening," *Exp. Mech.*, vol. 53, no. 9, pp. 1705–1718, 2013, doi: 10.1007/s11340-013-9766-x.
- [172] Y. Li, Y. Wu, H. Gong, and F. Xiao, "FEM and contour method study of quenching residual stress of 7050 aluminum alloy cross-shaped component," *Mater. Sci. Forum*, vol. 887 MSF, pp. 89–95, 2017, doi: 10.4028/www.scientific.net/MSF.887.89.
- [173] Y. L. Sun, M. J. Roy, A. N. Vasileiou, M. C. Smith, J. A. Francis, and F. Hosseinzadeh, "Evaluation of Errors Associated with Cutting-Induced Plasticity in Residual Stress Measurements Using the Contour Method," *Exp. Mech.*, vol. 57, no. 5, pp. 719–734, 2017, doi: 10.1007/s11340-017-0255-5.
- [174] M. D. Olson, A. T. DeWald, M. B. Prime, and M. R. Hill, "Estimation of Uncertainty for Contour Method Residual Stress Measurements," *Exp. Mech.*, vol. 55, no. 3, pp. 577–585, 2015, doi: 10.1007/s11340-014-9971-2.
- [175] M. D. Olson, A. T. DeWald, and M. R. Hill, "Validation of a Contour Method Single-Measurement Uncertainty Estimator," *Exp. Mech.*, vol. 58, no. 5, pp. 767–781, 2018, doi: 10.1007/s11340-018-0385-4.
- [176] F. Hosseinzadeh and P. J. Bouchard, "Mapping Multiple Components of the Residual Stress Tensor in a Large P91 Steel Pipe Girth Weld Using a Single Contour Cut," *Exp. Mech.*, vol. 53, no. 2, pp. 171–181, 2013, doi: 10.1007/s11340-012-9627-z.
- [177] G. Johnson, "Residual stress measurements using the contour method," University of Manchester, 2008. [Online]. Available: <https://www.lanl.gov/contour/docs/GregJohnsonPhDThesis.pdf>
- [178] M. B. Prime and A. T. DeWald, "The Contour Method," in *Practical Residual Stress Measurement Methods*, 2013. doi: 10.1002/9781118402832.ch5.
- [179] G. S. Schajer, "Relaxation Methods for Measuring Residual Stresses: Techniques and Opportunities," *Exp. Mech.*, vol. 50, no. 8, pp. 1117–1127, 2010, doi: 10.1007/s11340-010-9386-7.
- [180] J. F. Flavenot, "Layer Removal Method," in *Handbook of measurement of residual stresses*, 1996, pp. 35–48.
- [181] A. A. Denton, "Determination of Residual Stresses," *Metall. Rev.*, vol. 11, no. 1, pp. 1–23, Jan. 1966, doi: 10.1179/mtlr.1966.11.1.1.
- [182] G. G. Stoney, "The Tension of Metallic Films Deposited by Electrolysis," *Proc. R. Soc. London. Ser. A, Contain. Pap. a Math. Phys. Character*, vol. 82, no. 553, pp. 172–175, May 1909, doi: 10.1098/rspa.1909.0021.
- [183] M. Östlund, S. Östlund, L. A. Carlsson, and C. Fellers, "Experimental determination of residual stresses

- in paperboard," *Exp. Mech.*, vol. 45, no. 6, pp. 493–497, Dec. 2005, doi: 10.1007/BF02427902.
- [184] F. Hospers and L. B. Vogelesang, "Determination of Residual Stresses in Aluminum-alloy Sheet Material," *Exp. Mech.*, vol. 15, no. 3, pp. 107–110, Mar. 1975, doi: 10.1007/BF02320640.
- [185] J. G. Williams, J. M. Hodgkinson, and A. Gray, "The determination of residual stresses in plastic pipe and their role in fracture," *Polym. Eng. Sci.*, vol. 21, no. 13, pp. 822–828, 1981, doi: 10.1002/pen.760211304.
- [186] G. Sachs, "Der Nachweis Innerer Spannungen in Stange und Rohren/The Detection of Internal Stresses in Bars and Tubing," *Zitschrift für Met.*, vol. 19, pp. 352–357, 1927.
- [187] G. Sachs, "Internal Stresses in Piston Rods of a Large Diesel Engine Ocean Liner," *Trans. Am. Soc. Met.*, vol. 27, pp. 821–836, 1939.
- [188] G. Sachs and G. Espey, "The measurement of residual stresses in metal," *Iron Age*, pp. 63–71, 1941.
- [189] G. Sachs and G. Espey, "Method for Determination of Stress Distribution in Thin-walled Tubing," *Met. Technol.*, 1941.
- [190] L. Tahvilian, "Determination and Modeling of Residual Stress in Functionally Graded WC-Co," The University of Utah, 2014.
- [191] K. R. Van Horn, "Residual Stresses Introduced During Metal Fabrication," *Jom*, vol. 5, no. 3, pp. 405–422, 1953, doi: 10.1007/bf03398965.
- [192] S. X. Yuan, X. Q. Li, S. M. Y. C. Zhang, and Y. D. Gong, "Measurement of the residual stress distribution in a thick pre-stretched aluminum plate," *Fourth Int. Symp. Precis. Mech. Meas.*, vol. 7130, no. 1, p. 71302D, 2008, doi: 10.1117/12.819625.
- [193] H. Guo, D. Zuo, F. Yin, Y. He, J. Xu, and B. Chen, "Study on the residual stresses distribution in thick pre-stretched aluminum plate," *Key Eng. Mater.*, vol. 764, pp. 49–57, 2018, doi: 10.4028/www.scientific.net/KEM.764.49.
- [194] D. J. Hornbach, P. S. Prevéy, and P. W. Mason, "X-Ray Diffraction Characterization of the Residual Stress and Hardness Distributions in Induction Hardened Gears," *Proc. First Int. Conf. Induction Hardened Gears Crit. Components, Indianapolis, IN, May 15-17, 1995, Gear Res. Inst.*, no. 513, pp. 69–76, 1995.
- [195] M. Mahmoodi, M. Sedighi, and D. A. Tanner, "Investigation of through thickness residual stress distribution in equal channel angular rolled Al 5083 alloy by layer removal technique and X-ray diffraction," *Mater. Des.*, vol. 40, pp. 516–520, 2012, doi: 10.1016/j.matdes.2012.03.029.
- [196] S. Gungor and C. Ruiz, "Measurement of thermal residual stresses in continuous fibre composites," *Key Eng. Mater.*, vol. 127–131, no. Pt 2, pp. 851–860, 1997, doi: 10.4028/www.scientific.net/kem.127-131.851.
- [197] R. G. Treuting and W. T. Read, "A mechanical determination of biaxial residual stress in sheet materials," *J. Appl. Phys.*, vol. 22, no. 2, pp. 130–134, 1951, doi: 10.1063/1.1699913.
- [198] M. G. Moore and W. P. Evans, "Mathematical correction for stress in removed layers in X-ray diffraction residual stress analysis," *SAE Tech. Pap.*, vol. 45, pp. 340–345, 1958, doi: 10.4271/580035.
- [199] L. Liu, J. Sun, W. Chen, and P. Sun, "Modified Layer-Removal Method for Measurement of Residual Stress in Pre-stretched Aluminium Alloy Plate," *J. Harbin Inst. Technol.*, vol. 22, no. 2, pp. 24–40, 2015, doi: 10.11916/j.issn.1005-9113.2015.02.005.
- [200] Y. Ueda, "Sectioning Methods," in *Handbook of measurement of residual stresses*, L. Jian, Ed. Farnibt Press, 1996, pp. 49–70.
- [201] N. Kalakoutsky, "The Study of Internal Stresses in Cast Iron and Steel," London (1888), also St. Petersburg (1889), 1888.
- [202] N. Tebedge, G. Alpsten, and L. Tall, "Residual-stress measurement by the sectioning method," *Exp. Mech.*, vol. 13, no. 2, pp. 88–96, 1973, doi: 10.1007/bf02322389.
- [203] Y. Ueda and K. Fukuda, "New Measuring Method of Three-Dimensional Residual Stresses in Long Welded Joints Using Inherent Strains as Parameters—Lz Method," *J. Eng. Mater. Technol.*, vol. 111, no. 1, pp. 1–8, Jan. 1989, doi: 10.1115/1.3226427.
- [204] J. R. Shadley, E. F. Rybicki, and W. S. Shealy, "Application guidelines for the parting out step in a through thickness residual stress measurement procedure," *Strain*, vol. 23, no. 4, pp. 157–166, 1987, doi: 10.1111/j.1475-1305.1987.tb00640.x.
- [205] Y. Ueda, K. Fukuda, and Y. C. Kim, "New measuring method of axisymmetric three-dimensional residual stresses using inherent strains as parameters," *J. Eng. Mater. Technol. Trans. ASME*, vol. 108, no. 4, pp.

- 328–334, 1986, doi: 10.1115/1.3225890.
- [206] M. T. Hutchings, P. J. Withers, T. M. Holden, and T. Lorentzen, *Introduction to the Characterization of Residual Stress by Neutron Diffraction*, 1st ed. Boca Raton: Taylor & Francis Group, 2005. doi: 10.1201/9780203402818.
- [207] G. A. Webster and R. C. Wimpory, “Non-destructive measurement of residual stress by neutron diffraction,” *J. Mater. Process. Technol.*, vol. 117, no. 3, pp. 395–399, 2001, doi: 10.1016/S0924-0136(01)00802-0.
- [208] M. Francois *et al.*, “X-ray Diffraction Method,” in *Handbook of measurement of residual stresses*, 1996, pp. 71–132.
- [209] C. Ruud, “Measurement of Residual Stresses,” in *Handbook of Residual Stress and Deformation of Steel*, 2002, pp. 99–117. doi: 10.1361/hrsd2002p099.
- [210] O. Anderoglu, “Residual Stress Measurement Using X-Ray Diffraction,” Texas A&M University, 2004. [Online]. Available: <http://hdl.handle.net/1969.1/1507>
- [211] T. M. Holden, “Neutron Diffraction,” in *Practical Residual Stress Measurement Methods*, 2013. doi: 10.1002/9781118402832.ch8.
- [212] C. E. Murray and I. Cevdet Noyan, “Applied and Residual Stress Determination using X-Ray Diffraction,” in *Practical Residual Stress Measurement Methods*, 2013. doi: 10.1002/9781118402832.ch6.
- [213] “ENSA - European Neutron Scattering Association,” 2020. <http://www.neutrons-ensa.eu/>
- [214] M. Novosad, R. Fajkoš, B. Řeha, and R. Řezníček, “Fatigue tests of railway axles,” *Procedia Eng.*, vol. 2, no. 1, pp. 2259–2268, 2010, doi: 10.1016/j.proeng.2010.03.242.
- [215] P. Pokorný, T. Vojtek, L. Náhlík, and P. Hutař, “Crack closure in near-threshold fatigue crack propagation in railway axle steel EA4T,” *Eng. Fract. Mech.*, vol. 185, pp. 2–19, 2017, doi: 10.1016/j.engfracmech.2017.02.013.
- [216] T. Vojtek, P. Pokorný, I. Kuběna, L. Náhlík, R. Fajkoš, and P. Hutař, “Quantitative dependence of oxide-induced crack closure on air humidity for railway axle steel,” *Int. J. Fatigue*, vol. 123, no. February, pp. 213–224, 2019, doi: 10.1016/j.ijfatigue.2019.02.019.
- [217] A. Pourheidar, L. Patriarca, S. Beretta, and D. Regazzi, “Investigation of Fatigue Crack Growth in Full-Scale Railway Axles Subjected to Service Load Spectra: Experiments and Predictive Models,” *Metals (Basel)*, vol. 11, no. 9, p. 1427, Sep. 2021, doi: 10.3390/met11091427.
- [218] T. Vojtek *et al.*, “Classically determined effective  $\Delta K$  fails to quantify crack growth rates,” *Theor. Appl. Fract. Mech.*, vol. 108, no. April, p. 102608, 2020, doi: 10.1016/j.tafmec.2020.102608.
- [219] M. Traupe, H. Meinen, and H. Zenner, “Sichere und wirtschaftliche Auslegung von Eisenbahnfahrwerken,” 2004.
- [220] P. Pokorný, P. Hutař, and L. Náhlík, “Residual fatigue lifetime estimation of railway axles for various loading spectra,” *Theor. Appl. Fract. Mech.*, vol. 82, pp. 25–32, 2016, doi: 10.1016/j.tafmec.2015.06.007.
- [221] P. Pokorný, L. Náhlík, and P. Hutař, “Comparison of different load spectra on residual fatigue lifetime of railway axle,” *Procedia Eng.*, vol. 74, pp. 313–316, 2014, doi: 10.1016/j.proeng.2014.06.269.
- [222] L. Náhlík, P. Pokorný, M. Ševčík, R. Fajkoš, P. Matušek, and P. Hutař, “Fatigue lifetime estimation of railway axles,” *Eng. Fail. Anal.*, vol. 73, pp. 139–157, Mar. 2017, doi: 10.1016/j.engfailanal.2016.12.014.
- [223] R. V. Mises, “On Saint Venant’s principle,” *Bull. Am. Math. Soc.*, vol. 51, no. 8, pp. 555–562, 1945, doi: 10.1090/S0002-9904-1945-08394-3.
- [224] “ANSYS Inc., ANSYS Help Release 2020 R2.” ANSYS Inc.
- [225] P. Dlhý, J. Poduška, P. Pokorný, L. Náhlík, R. Fajkoš, and P. Hutař, “Methodology for estimation of residual stresses in hardened railway axle,” *Procedia Struct. Integr.*, vol. 23, pp. 185–190, 2019, doi: 10.1016/j.prostr.2020.01.084.
- [226] M. Berer, I. Mitev, and G. Pinter, “Finite element study of mode I crack opening effects in compression-loaded cracked cylinders,” *Eng. Fract. Mech.*, vol. 175, pp. 1–14, 2017, doi: 10.1016/j.engfracmech.2017.03.008.
- [227] A. Gosch *et al.*, “Mixed Mode I/III fatigue fracture characterization of Polyoxymethylene,” *Int. J. Fatigue*, vol. 130, no. September 2019, 2020, doi: 10.1016/j.ijfatigue.2019.105269.
- [228] A. Gosch, F. J. Arbeiter, M. Berer, T. Vojtek, P. Hutař, and G. Pinter, “Fatigue characterization of polyethylene under mixed mode I/III conditions,” *Int. J. Fatigue*, vol. 145, no. August 2020, 2021, doi:

- 10.1016/j.ijfatigue.2020.106084.
- [229] P. Schrader, A. Gosch, M. Berer, and S. Marzi, "Fracture of thin-walled polyoxymethylene bulk specimens in modes i and iii," *Materials (Basel)*, vol. 13, no. 22, pp. 1–18, 2020, doi: 10.3390/ma13225096.
- [230] P. Dlhý *et al.*, "Crack Propagation Analysis of Compression Loaded Rolling Elements," *Materials (Basel)*, vol. 14, no. 10, p. 2656, May 2021, doi: 10.3390/ma14102656.
- [231] C. F. Shih, B. Moran, and T. Nakamura, "Energy release rate along a three-dimensional crack front in a thermally stressed body," *Int. J. Fract.*, vol. 30, no. 2, pp. 79–102, 1986, doi: 10.1007/BF00034019.
- [232] A. R. Ingraffea and C. Manu, "Stress-intensity factor computation in three dimensions with quarter-point elements," *Int. J. Numer. Methods Eng.*, vol. 15, no. 10, pp. 1427–1445, Oct. 1980, doi: 10.1002/nme.1620151002.
- [233] P. Pokorný, L. Náhlík, and P. Hutař, "Influence of variable stress ratio during train operation on residual fatigue lifetime of railway axles," *Procedia Struct. Integr.*, vol. 2, pp. 3585–3592, 2016, doi: 10.1016/j.prostr.2016.06.447.
- [234] P. Hutař, S. Seitzl, and T. Kruml, "Effect of specimen geometry on fatigue crack propagation in threshold region," *12th Int. Conf. Fract. 2009, ICF-12*, vol. 4, pp. 2914–2922, 2009.
- [235] A. K. Vasudevan and K. Sadananda, "Application of unified fatigue damage approach to compression-tension region," *Int. J. Fatigue*, vol. 21, no. SUPPL. 1, pp. 263–273, 1999, doi: 10.1016/s0142-1123(99)00097-3.
- [236] S. Beretta and M. Carboni, "Experiments and stochastic model for propagation lifetime of railway axles," *Eng. Fract. Mech.*, vol. 73, no. 17, pp. 2627–2641, 2006, doi: 10.1016/j.engfracmech.2006.04.024.
- [237] S. Beretta and D. Regazzi, "Probabilistic fatigue assessment for railway axles and derivation of a simple format for damage calculations," *Int. J. Fatigue*, vol. 86, pp. 13–23, 2016, doi: 10.1016/j.ijfatigue.2015.08.010.
- [238] C. Mallor, S. Calvo, J. L. Núñez, R. Rodríguez-Barrachina, and A. Landaberea, "On the use of probabilistic fatigue life estimation in defining inspection intervals for railway axles," *Procedia Struct. Integr.*, vol. 33, pp. 391–401, 2021, doi: 10.1016/j.prostr.2021.10.047.
- [239] A. Gelman, J. B. Carlin, H. S. Stern, D. B. Dunson, A. Vehtari, and D. B. Rubin, *Bayesian Data Analysis*. CRC Press, 2014.
- [240] P. Pokorný, T. Vojtek, M. Jambor, L. Náhlík, and P. Hutař, "Effect of underload cycles on oxide-induced crack closure development in cr-mo low-alloy steel," *Materials (Basel)*, vol. 14, no. 10, pp. 1–22, 2021, doi: 10.3390/ma14102530.

## 13 List of Abbreviations

2D	two-dimensional
3D	three-dimensional
a	actual crack length
a/W	Normalised crack length
a <sub>0</sub>	Initial crack length
A	material constant for Paris-Erdogan region definition
A1	C35 steel
A2	22MnCrV5 steel
A3	C45 steel
A4	25CrMo4 steel
A5	42CrMo4 steel
A <sub>5</sub>	strain at failure
a <sub>c</sub>	critical size of crack length
a <sub>f</sub>	final crack length
A <sub>j</sub>	set of coefficients
a <sub>n</sub>	notched crack depth
ASTM	American Society for Testing and Materials
A <sub>t</sub>	amplitude of t <sup>th</sup> term
ax	axial
b	semi-major axis of the crack shape ellipse
BL	bending load
b <sub>n</sub>	notched crack width
c	fatigue ductility exponent
C	material constant for NASGRO approach definition
C	flexibility function
C	Carbon
C*	material constant for modified NASGRO approach definition
CCD	charge-coupled device
CCT	centre-crack tension
CEN/TR	European Committee for Standardization / technical report
Cr	Chromium
Cu	Copper
d	hole diameter after trepaning
d	distance between the diffracting planes
D	diameter dimension of the cylinder
d'	hole diameter before trepaning
d <sub>0</sub>	nominal reference hole diameter
d <sub>0</sub> <sup>hkl</sup>	stress-free lattice spacing
da/dN, v	crack propagation (growth) rate
DHD	Deep Hole Drilling
dir	direction
DNP	do not propagate
E	Young's modulus
EDM	electrical discharge machining
EN	European Norm (standard)
etc.	Et cetera; and other things; and so on
EU	European Union
F	reaction force
f <sub>A</sub>	area A fraction
FE	finite element

FEM	finite element method
G	energy release rate
$G_c$	critical value of energy release rate
$g_{ij(t)}$	shape function of $t^{\text{th}}$ term
GPa	gigapascal
h	crack depth
HV	Vickers Pyramid Number
i	subscript corresponds to the radius of the evaluated surface
IH	induction hardening
IPM CAS	Institute of Physics of Materials of the Czech Academy of Sciences
J	J-integral
k	constant which is related to the stress intensity factor
k	dynamic coefficient
$K^*$	pseudo stress intensity factor
$K_a$	amplitude of the stress intensity factor
$K_{BL,d}$	dynamic stress intensity factor caused by bending load
$K_{BL,s}$	static stress intensity factor caused by bending load
$K_C$	critical value of stress intensity factor
$K_{\text{eff}}$	effective stress intensity factor
$K_{Ic}$ $K_C$	fracture toughness
$K_I$	stress intensity factor from mode I loading
$K_I^{(A)}, K_I^{(B)}, K_I^{(C)}$	stress intensity factor components corresponding to different loads
$K_{II}$	stress intensity factor from mode II loading
$K_{III}$	stress intensity factor from mode III loading
$K_I^{\text{total}}, K^{\text{total}}$	total stress intensity factor
kkm	thousands of kilometers
km	kilometers
$K_m$	mean of the stress intensity factor
km/h	kilometers per hour
$K_{\text{max}}$	maximum of the stress intensity factor
$K_{\text{max,th}}$	maximum stress intensity factor threshold
$K_{\text{min}}$	minimum stress intensity factor
kN	kilonewtons
$K_{PF}$	stress intensity factor caused by press-fit
$K_{RS}$	stress intensity factor caused by residual stress
$K_{\text{th}}$	stress intensity factor threshold
kV	kilovolts
L	length dimension of the cylinder
$l_1, l_2$	finite element dimensions
LCR	ultrasonic critically refracted longitudinal wave
LEFM	linear elastic fracture mechanics
LRBM	layer-removal-based method
mA	milliampere
m	material constant for Paris-Erdogan region definition
mm	millimeters
Mn	Manganese
Mo	Molybdenum
MPa	megapascal
$\text{MPa}\cdot\text{m}^{1/2}$	megapascal per meter
$\text{MPa}\cdot\text{mm}^{1/2}$	megapascal per millimeter
N	normalised / tempered
N	number of cycles

n	integer
n	number of measured depth points + 1
N	Newton
n	material constant for NASGRO approach definition
n*	material constant for modified NASGRO approach definition
NDT	non-destructive testing
N <sub>f</sub>	number of cycles to the failure
Ni	Nickel
n <sub>j</sub>	outward unit vector
NPI CAS	Nuclear Physics Institute of the Czech Academy of Sciences
P	Phosphorus
p	material constant for NASGRO approach definition
p*	material constant for modified NASGRO approach definition
PF	press-fit load
P <sub>j</sub> (x)	Legendre basis interpolation functions
PoD	probability of detection
POM	Polyoxymethylene
q	material constant for NASGRO approach definition
r	radial polar coordinate
R	stress (or stress intensity factor) ratio of the cycle
RFL	residual fatigue lifetime
r <sub>in</sub>	inner surface radius
r <sub>ou</sub>	outer surface radius
RS	residual stress
RS UNIZA	Research Centre of the University of Žilina
S	Sulphur
S	corresponding area
SBM	sectioning-based method
Si	Silicon
SIF, K	stress intensity factor
S-N	stress – number of cycles to the failure
T	heat-treated
tg	tangential
T <sub>i</sub>	components of the line load acting perpendicular to the integration path $\Gamma$
U	unbalance
u, v, w	displacement in cartesian coordinates
u <sub>i</sub>	vector of displacements,
UIC	International Union of Railways
UK	United Kingdom
V	Vanadium
W	strain energy density
x, y, z	cartesian coordinates
X-ray	Röntgen ray
XRD	X-ray diffraction
Y <sub>i</sub> (a/W)	function corresponding to the component geometry
z	depth through the core thickness
Z	influence function
$\langle \sigma_1 \rangle_A^{II,III}$	micro residual stresses of type II and III at A area
$\langle \sigma_1 \rangle^{II}$	micro residual stresses of type II
$\langle \sigma_2 \rangle_A^{II,III}$	micro residual stresses of type II and III at A area
$\langle \sigma_2 \rangle^{II}$	micro residual stresses of type II
$\gamma$	crack tip position angel

$\Delta d$	hole diameter difference
$\Delta K$	stress intensity factor range
$\Delta d_{xx}^{hkl}$	difference in lattice spacing
$\lambda$	wavelength of the electromagnetic radiation
$\nu$	Poisson ratio
$\rho$	cylinder rotation angle
$\sigma$	far-field applied stress
$\sigma_0$	flow stress
$\sigma_{ij}$	stress tensor
$\sigma_u$	ultimate tensile stress
$\sigma_y$	yield stress
$\sigma_{y,c}$	cyclic yield stress
$\Gamma$	integration path
$\varepsilon_{ap}$	plastic strain amplitude
$\varepsilon_f'$	fatigue ductility coefficient
$\varepsilon_{ij}$	strain tensor
$\varepsilon_{xx}^{hkl}$	lattice strain in local x direction
$\theta$	angle polar coordinate; angular orientation
$\theta$	Bragg angle
$\pi$	Pi (mathematical constant)
$\sigma_{xy}$	shear stress component
$\sigma_{yy}$	opening stress
$\sigma_{zz}$	Stress in Z direction

## 14 List of Figures

Figure 1 Examples of some typical ways in which residual stress is developed in engineering materials [1] .....	10
Figure 2 Stress components near crack tip a) cartesian coordinate system b) polar coordinate system [3] .....	12
Figure 3 Modes of crack loading [14] .....	13
Figure 4 Schematic illustration of stress field portability from test specimen to actual structure [12] 14	14
Figure 5 Typical stress-life (S-N) curve [19] .....	14
Figure 6 Different phases of the fatigue life with schematic illustration [20], [24] .....	15
Figure 7 Wheelset design types; a) outboard bearings arrangement, b) inboard bearing arrangement, c) the axlebridge design principle, d) independent wheel arrangement with bearings on both sides [35] .....	17
Figure 8 Types of wheelsets with external journals; a) pure wheelset, b) wheelset with brake discs on the axle, c) wheelset with brake discs on the wheels, d) wheelset with asymmetric gear position, e) wheelset with symmetric gears position [36] .....	17
Figure 9 Example of coated axle [44] .....	18
Figure 10 New axles in development; (a) axle with torque limiter [42], (b) composite axle [43] .....	18
Figure 11 Ultrasound testing probe position: (a) solid axle, (b) hollow axle [45] .....	19
Figure 12 (a) PoD curve comparison for solid and hollow axle [46], (b) Master PoD curve through naturally fatigued cracked hollow axles [47] .....	20
Figure 13 Typical fatigue crack locations for the railway axle [45], [59] .....	21
Figure 14 Scheme of a crack in bent plate. The basic model for SIF estimation [61] .....	21
Figure 15 SIF ahead of the crack tip with extrapolation value for estimation of SIF at the crack tip [12] .....	22
Figure 16 Integration path used for the calculation [79], [80] .....	23
Figure 17 2D and 3D singular element [81]–[84] .....	23
Figure 18 Three regions of a crack growth rate as a function of $\Delta K$ .....	25
Figure 19 Description of the loading cycle .....	25
Figure 20 Residual stress distribution over several grains of a two-phase material showing the three kinds of residual stresses [1], [101], [107] .....	27
Figure 21 Comparison of different residual stress measurement techniques [107], [111], [125] .....	28
Figure 22 Schematic view of ultrasonic measurement configurations: a) through-thickness with one transducer, b) through-thickness with two transducers, and c) surface with two transducers [134]..	29
Figure 23 Function of penetration depth on ultrasonic frequency [135] .....	29
Figure 24 schematic illustration of DHD technique a) attachment of reference bushes and gun-drilling reference hole, b) measurement of the diameter of reference hole through the depth of hole c) trepanning of material around the hole (core) often by electro-discharge machining, d) final diameter measurement of residual stress-free reference hole [140] .....	30
Figure 25 FEM simulation of the DHD method a) original specimen b) specimen with gun-drilled hole c) specimen with a trepanned cylinder around hole [144] .....	30
Figure 26 Illustration of slitting measurement .....	31
Figure 27 Superposition principle is used to determine the original residual stress from the measurement of surface contour after cutting a part in two [164] .....	32
Figure 28 Layer removal method for cylinder and flat plate .....	33

Figure 29 Welded joint of thick plate sectioned to specimens T and L <sub>i</sub> [203].....	33
Figure 30 Diffraction ratio within the crystal structure .....	34
Figure 31 Principle of diffraction measurement .....	34
Figure 32 Map of neutron scattering facilities in Europe [213] .....	35
Figure 33 Considered railway axles .....	37
Figure 34 Typical bainitic microstructure of the EA4T steel of conventionally treated axle [216] .....	38
Figure 35 Histogram of used spectrum, sorted into 36 loading levels, which represents 1000 km of service operation.....	39
Figure 36 Boundary conditions of the used model for the critical position determination .....	39
Figure 37 Axial stress behaviour near the critical position at the axle .....	40
Figure 38 Scheme of the developed optimization process of residual stresses determination in sizeable components.....	41
Figure 39 Scheme of considered railway axle with highlighted segments for residual stress measurements.....	41
Figure 40 Measured residual stress versus the etched depth for different circumferential positions determined on the original outer surface.....	42
Figure 41 The measuring points' position for the LRBM.....	43
Figure 42 Illustration of LRBM (a) segment models; (b) defined initial stress state; (c) redistributed equilibrium stress state.....	44
Figure 43 Schematic evolution of first two iterations of initial state input data for measured axial residual stress.....	45
Figure 44 Optimized solution for simulated segments .....	45
Figure 45 Results of residual stresses determined by LRBM .....	46
Figure 46 Final residual stress distribution in the whole axle.....	46
Figure 47 Scheme of the iterative evaluation method for the correction of residual stress values measured by X-ray diffraction.....	47
Figure 48 Schematic illustration of the analytical residual stress determination process.....	49
Figure 49 Corresponding area functions behaviour.....	50
Figure 50 Comparison of axial residual stress evaluated by numerical simulations and developed solution in MATLAB from the same measured data with (a) fine depth sampling and (b) coarse depth sampling .....	50
Figure 51 Measuring paths positions for segment A and segment R for SBM.....	51
Figure 52 Example of the experimental segment A like specimen manufactured from a different axle .....	51
Figure 53 Illustration of SBM (a), (b), (c) segment A - axial cut; (d), (e), (f) segment R - radial cut; (a), (d) models for measurement; (b), (e) distribution of input stress; (c), (f) redistributed stress after numerical calculation .....	52
Figure 54 Optimized stress components for segment A (axial cut) .....	53
Figure 55 Optimized stress components for segment R (radial cut).....	53
Figure 56 Results of residual stress measurement by SBM .....	53
Figure 57 Comparison of axial residual stress measured by different methods.....	54
Figure 58 Comparison of axial residual stress evaluated by different methodologies from the same measured data with (a) fine depth sampling and (b) coarse depth sampling .....	55
Figure 59 (a) Comparison of tangential residual stresses measured by different methods on (b) ring specimens.....	57

Figure 60 Axial surface residual stress at the investigated railway axle .....	57
Figure 61 Induction hardened axle hardness.....	58
Figure 62 Microstructure of the induction hardening axle. Samples were extracted from different axle depths.....	59
Figure 63 The situation of the bearing cylinder with an internal defect, compressed between two steel plates and rolling. ....	61
Figure 64 The mesh of the whole symmetrical FEM model of the bearing cylinder. The refined area in the vicinity of the crack tip is pictured in the detailed view (note the special crack tip elements in the middle). ....	62
Figure 65 Schematic illustration of the changing orientation of the crack during rolling and the angle $\rho$ that describes the rolling position.....	63
Figure 66 Comparison of $K_I$ values for different crack lengths from Berer et al. [226] and the newer model described here.....	64
Figure 67 Difference between determined $K_I$ values for different methods and from Berer et al. [226] for crack length 1.25 mm .....	64
Figure 68 3D plot of $K_I$ as a function of both, the circumferential position on the crack front $\gamma$ and the rolling orientation of the crack $\rho$ , crack length $a = 1.25$ mm. The upper surface reflects contact between crack faces (highlighted by the solid red line). The lower surface is negative theoretical values of $K_I$ acquired from a model where no contact was defined between crack faces (highlighted by the dashed red line).....	65
Figure 69 3D plot of $K_{II}$ as a function of both, the circumferential position on the crack front $\gamma$ and the rolling orientation of the crack $\rho$ , crack length $a = 1.25$ mm. ....	65
Figure 70 3D plot of $K_{III}$ as a function of both, the circumferential position on the crack front $\gamma$ and the rolling orientation of the crack $\rho$ , crack length $a = 1.25$ mm. ....	65
Figure 71 Course of stress intensity factors during rotation in the cylinder $D \times L = 6 \times 6$ mm, load $F = 350$ N, $a = 0.25$ mm, position on the crack front; (a) $\gamma = 0^\circ$ ; (b) $\gamma = -90^\circ$ .....	66
Figure 72 Course of stress intensity factors during rotation in the cylinder $D \times L = 6 \times 6$ mm, load $F = 350$ N, $a = 0.75$ mm, position on the crack front; (a) $\gamma = 0^\circ$ ; (b) $\gamma = -90^\circ$ .....	66
Figure 73 Course of stress intensity factors during rotation in the cylinder $D \times L = 6 \times 6$ mm, load $F = 350$ N, $a = 0.85$ mm, position on the crack front; (a) $\gamma = 0^\circ$ ; (b) $\gamma = -90^\circ$ .....	66
Figure 74 Course of stress intensity factors during rotation in the cylinder $D \times L = 6 \times 6$ mm, load $F = 350$ N, $a = 1.00$ mm, position on the crack front; (a) $\gamma = 0^\circ$ ; (b) $\gamma = -90^\circ$ .....	67
Figure 75 Course of stress intensity factors during rotation in the cylinder $D \times L = 6 \times 6$ mm, load $F = 350$ N, $a = 1.25$ mm, position on the crack front; (a) $\gamma = 0^\circ$ ; (b) $\gamma = -90^\circ$ .....	67
Figure 76 Course of stress intensity factors during rotation in the cylinder $D \times L = 6 \times 6$ mm, load $F = 350$ N, $a = 1.75$ mm, position on the crack front; (a) $\gamma = 0^\circ$ ; (b) $\gamma = -90^\circ$ .....	67
Figure 77 Maximum stress intensity factors in the rolling cycle for different crack tip positions $\gamma$ depending on the normalized crack length. The indices $0^\circ$ and $90^\circ$ indicate the position $\gamma$ at the crack front.....	69
Figure 78 The R-ratio for different loading modes at different positions on the crack front during crack growth (left) with a schematic illustration of loading cycles with different R-ratios (right). The indices $0^\circ$ and $90^\circ$ indicate the position $\gamma$ at the crack front .....	69
Figure 79 a) Parametric functions fitting the values of $Y_{I_{max} 90^\circ}$ ; (b) Parametric functions fitting the values of $Y_{I_{max} 0^\circ}$ .....	70

Figure 80 (a) Parametric functions fitting the values of $Y_{Imin\ 90^\circ}$ ; (b) Parametric functions fitting the values of $Y_{Imin\ 0^\circ}$ .....	71
Figure 81 (a) Parametric functions fitting the values of $Y_{IIImax\ 90^\circ}$ ; (b) Parametric functions fitting the values of $Y_{IIImax\ 0^\circ}$ .....	72
Figure 82 Schematic geometry of the surface (a) and the internal (b) cracks .....	74
Figure 83 Schematic illustration of the boundary conditions .....	74
Figure 84 Residual stress profile after induction hardening used for the SIF determination; (a) tangential stress, (b) axial stress .....	75
Figure 85 Residual stress profile after quenching used for the SIF determination; (a) tangential stress, (b) axial stress.....	75
Figure 86 Axial stress results in different models with the surface crack.....	76
Figure 87 Possible stress intensity factor range corresponding to different bending load amplitudes	77
Figure 88 Stress intensity factor results for the considered surface crack lengths for different loading types .....	78
Figure 89 Stress intensity factors for different crack depths for crack length 1 mm.....	79
Figure 90 Crack propagation estimation for the dynamic coefficient (a) $k = 1$ (b) $k = 2.88$ (c) $k = 1.8$ .	80
Figure 91 Different railway axles fractured by the internal fatigue crack growth. ....	81
Figure 92 Stress intensity factors for different crack lengths .....	82
Figure 93 CCT specimen geometry and scheme of the cut-out area from cylindrical part of railway axle (a) standard heat-treated; (b) induction hardened .....	84
Figure 94 Fatigue crack growth curves (a) $v-\Delta K$ (b) $v-K_{max}$ .....	84
Figure 95 Comparison of $v-K_{max}$ curves for the classic EA4T material and the induction hardened material .....	85
Figure 96 $K_{max, th}$ values for different load ratio $R$ .....	85
Figure 97 Scheme of full-scale experiment .....	89
Figure 98 Fracture surface after the experiment .....	90
Figure 99 Flow chart of the stochastic lifetime estimation procedure .....	93
Figure 100 $v-K$ data used for lifetime estimation, experimental points, and generated curves .....	93
Figure 101 RFL estimation distribution for all three experimentally tested axles with consideration of all uncertainties; (a) axle 1, (b) axle 2, and (c) axle 3 .....	94

# 15 List of Tables

- Table 1 Chemical composition of the EA4T steel [214]..... 37
- Table 2 Mechanical properties of the EA4T steel [215]–[218]..... 37
- Table 3 Microstructure summary after the induction hardening ..... 59
- Table 4 NASGRO fitting constants summary ..... 87
- Table 5 Estimated residual fatigue lifetime in thousands of kilometres (kkm) for the crack growth from  $a_0$  up to 25 mm (DNP - do not propagate)..... 88
- Table 6 Experimental and estimated residual fatigue lifetime [99]..... 90
- Table 7 Considered uncertainties..... 92
- Table 8 Summary of the deterministic and stochastic residual fatigue lifetime estimation with the experimentally tested mileage ..... 95

## 16 Author's publication list and other activities

### Impacted journals:

- P. Dlhý**, J. Poduška, P. Pokorný, M. Jambor, L. Náhlík, D. Kajánek, R. Fajkoš, P. Hutař: "Estimation of residual stress distribution in railway axles" *Engineering Failure Analysis*. 135 (2022) 106142 (IF: 3.634)
- P. Dlhý**, J. Poduška, M. Berer, A. Gosch, O. Slávik, L. Náhlík, P. Hutař: "Crack Propagation Analysis of Compression Loaded Rolling Elements". *Materials* 14 (2021) 2656 (IF: 3.748)
- S. Fintová, **P. Dlhý**, K. Mertová, Z. Chlup, M. Duchek, R. Procházka, P. Hutař: "Fatigue properties of UFG Ti grade 2 dental implant vs. conventionally tested smooth specimens" *Journal of the Mechanical Behavior of Biomedical Materials*. 123 (2021) 104715 (IF: 4.042)
- F. Arbeiter, L. Trávníček, S. Petersmann, **P. Dlhý**, M. Spoerk, G. Pinter, P. Hutař: "Damage tolerance-based methodology for fatigue lifetime estimation of a structural component produced by material extrusion-based additive manufacturing" *Additive Manufacturing*. 36 (2020) 101730 (IF: 11.632)
- P. Pokorný, **P. Dlhý**, J. Poduška, R. Fajkoš, T. Vojtek, L. Náhlík, M. Grasso, P. Hutař: "Influence of heat treatment-induced residual stress on residual fatigue life of railway axles" *Theoretical and Applied Fracture Mechanics*. 109 (2020) 102732 (IF: 4.374)

### Reviewed journals:

- P. Dlhý**, J. Poduška, P. Pokorný, M. Jambor, L. Náhlík, P. Hutař: "Residual stress determination by the layer removal and X-ray diffraction measurement – correction method" *MethodsX* 9 (2022) 101768
- J. Poduška, **P. Dlhý**, P. Hutař, A. Frank, J. Kučera, J. Sadílek, L. Náhlík: "Design of plastic pipes considering content of recycled material" *Procedia Struct. Integr.* 23 (2019) 293-298
- P. Dlhý**, J. Poduška, P. Pokorný, L. Náhlík, and R. Fajkoš, "Methodology for estimation of residual stresses in hardened railway axle," *Procedia Struct. Integr.*, vol. 23, no. 2019, pp. 185–190, 2020. (Presented at MSMF9 international conference, in 2019, Brno, ČR)
- P. Dlhý**, J. Poduška, L. Náhlík, M. Berer, A. Gosch, G. Pinter, P. Hutař, "Compression-Loaded Cracked Cylinder - Stress Intensity Factor Evaluation," *Key Eng. Mater.*, vol. 774, pp. 331–336, Aug. 2018. (Presented at FDM2018 international conference, in 2018, Seville, ES)

### Conference proceedings:

- D. Tichoň, **P. Dlhý**, T. Vojtek, P. Pokorný, P. Hutař, L. Náhlík "Estimation of residual fatigue life of railway axles considering stochastic input parameters". In 2022 (5th Iberian Conference on Structural Integrity, Coimbra, Portugal)
- P. Dlhý**, J. Poduška, L. Náhlík, M. Berer, A. Gosch, G. Pinter and P. Hutař „Fracture mechanics description of the defect in rolling cylinder“. In: 2019 (Computational mechanics 2019, Srní, ČR)
- P. Pokorný, **P. Dlhý**, J. Poduška, L. Náhlík, R. Fajkoš and P. Hutař „Benefit of heat treatment induced residual stresses on residual fatigue lifetime of railway axles“. In: 2019 (ICSID 2019 international conference, Dubrovnik, HR)
- P. Dlhý**, J. Poduška, P. Pokorný, L. Náhlík, R. Fajkoš and P. Hutař „Numerically designed methodology for estimation of residual stresses in hardened cylinder“. In: 2019 (Applied mechanics 2019, Ostravice, ČR)
- P. Dlhý**, L. Náhlík, F. Arbeiter, A. Gosch and P. Hutař „Analysis of crack growth in 3D printed plastic wrench“. In: 2018 Computational mechanics 2018, Srní, ČR)
- J. Poduška, P. Hutař, I. Berger, A. Frank, **P. Dlhý** and L. Náhlík. „Examining factors potentially influencing the lifetime of the electrofusion socket“. In: 2018, s. 5. (ANTEC 2018, Orlando, FL, USA)
- P. Hutař, J. Poduška, **P. Dlhý**, A. Frank, J. Kučera, J. Sadílek, G. Pinter and L. Náhlík. „Multilayer polymer pipes – possible utilization of recycled material“. In: 2018, s. 8. ISBN 9162856030. (Plastic Pipes XIX Conference, Las Vegas, NV, USA)
- P. Dlhý**, J. Poduška, L. Náhlík, M. Berer, A. Gosch and P. Hutař „Study Of Compression Loaded Central Cracked Polymer Cylinder“. In: 2018 (PhD and Postdoc retreat 2018, Telč, ČR)
- P. Dlhý**, J. Poduška, L. Náhlík, M. Berer, A. Gosch and P. Hutař „Compression-loaded cracked cylinder – stress intensity factor evaluation“. In: 2018 (Applied mechanics 2018, Myslovice, ČR)
- P. Dlhý**, P. Novák, „Analysis of contact force along spherical roller bearing element“. In: 2017 (Computational mechanics 2017, Špičák, ČR)

Projects:

- CK03000060 - "Advanced design methodology of railway axles for safe and efficient operation" of Technology Agency of the Czech Republic
- FW03010149 - "New wheel design for freight transport with higher utility properties" of Technology Agency of the Czech Republic
- FV40034 - "Development of new design of railway axles with high operational reliability" of Ministry of Industry and Trade of the Czech Republic
- FV40327 - "Automatic optical system for fatigue crack propagation measurement" of Ministry of Industry and Trade of the Czech Republic
- TN01000071 - "National Competence Centre of Mechatronics and Smart Technologies for Mechanical Engineering" of Technology Agency of the Czech Republic
- PCCL-K1 - "K1-Center in Polymer Engineering and Science" of Competence Centers of Excellent Technologies (COMET) of the Austrian Research Promotion Agency (FFG)
- CZ.01.1.02/0.0/0.0/15\_019/0002421 - "Research and development of advanced precision casting technology of strongly thermally affected parts of new turbochargers from nickel based superalloys" of Ministry of Industry and Trade of the Czech Republic
- INNOFAT - RFCS - "Innovative approach to improve fatigue performance of automotive components aiming at CO2 emissions reduction" of the Research Fund for Coal and Steel of the European Union
- GJ19-25591Y - "Effect of the microstructure on the fatigue in highly anisotropic stainless steel fabricated by selective laser melting" of Czech Science Foundation
- FV40327 - "Automatic optical system for fatigue crack propagation measurement" of Ministry of Industry and Trade of the Czech Republic
- 21-14886S - "Influence of material properties of high strength steels on durability of engineering structures and bridges" of Czech Science Foundation

## 17 Curriculum vitae

Name: Ing. Pavol Dlhý  
Birth date: 21.01.1993  
Address: Zemiansky kút, 918/13, 91621 Čachtice, Slovak Republic  
Phone number: +421908322379, +420773764875  
E-mail: dlhypavol@gmail.com, dlhy@ipm.cz



### *Education:*

#### **2017 - present**

CEITEC - Central European Institute of Technology - Brno University of Technology,  
Brno, Czech Republic  
Ph.D. program: Advanced Materials and Nanosciences

#### **2015 - 2017**

University of Žilina, Faculty of Mechanical Engineering, Žilina, Slovak Republic  
Master`s program: CAE modeling and simulation at mechanical engineering

#### **2012 - 2015**

University of Žilina, Faculty of Mechanical Engineering, Žilina, Slovak Republic  
Bachelor`s degree in Engineering Technology

#### **2008 - 2012**

High School of Mechanical Engineering, Nové Mesto nad Váhom, Slovak Republic  
Study program: Construction of Machinery

### *Working knowledge:*

#### **Institute of Physics of Materials AS CR v.v.i.**

2017 - present – Ph.D. student

- member of High Cycle Fatigue Group
- research interest: determination of residual stress and its influence on fatigue properties of metallic materials, design and support of experiments by finite element method

#### **CEIT a.s.**

2016 - 2017 - FEM specialist – part-time job

- static analysis
- modal analysis and measurement

### *Skills:*

ANSYS Mechanical APDL – advanced  
ANSYS Workbench – advanced  
MATLAB – advanced  
AutoCAD – basic  
AutoCAD Inventor – basic  
Python – basic  
Driving license: Group B (from 2012)

### *LinkedIn profile:*

<https://www.linkedin.com/in/pavol-dlhý-18177b137>